Interstitial Modification of Palladium for Partial Hydrogenation Reactions

Ieuan T. Ellis

University College

University of Oxford

A thesis submitted for the degree of

Doctor of Philosophy

2016

Interstitial Modification of Palladium for Partial Hydrogenation Reactions

by

Ieuan T. Ellis

University College

Supervisor

Professor S. C. E. Tsang

Industrial Supervisor

Dr A. P. E. York

Internal Assessor

Professor J. S. Foord

A thesis submitted for the degree of Doctor of Philosophy at the Inorganic Chemistry Laboratory, Department of Chemistry, University of Oxford

2016

Dedication

To my friends and family.

Declaration

I hearby declare that this is my own work and the use of all materials from other sources has been properly and fully acknowledged.

Ieuan T. Ellis
January 21, 2017

Acknowledgements

First and foremost, I would like to thank Professor Edman Tsang for giving me the opportunity to join his research group and his continual, invaluable guidance throughout the course of my DPhil project. Additionally, I would like to express my gratitude to Johnson Matthey for their funding and to my industrial supervisor, Dr Andrew York, for his insight and support as well as his excellent dinner conversation. Thanks must also go to the University of Oxford and the Johnson Matthey Technology Centre (JMTC), Sonning Common for access to their research equipment and facilities.

The research presented in this thesis would not have been possible without the valuable assistance and support I have received from the following individuals within my own and other research groups in Oxford and further afield: Dr Ashley Shepherd for her training and assistance with XPS, Dr Philip Wiseman for training on several XRD instruments, Dr Aaron Lau for help with TGA and to Ben Lo and Professor Chui Tang for synchrotron PDF analysis.

I am extremely grateful to Chris Brown of Johnson Matthey for all his help and patience in carrying out and analysing the liquid and vapour phase hydrogenations undertaken at Sonning Common. Thanks must also go Dr Pilar Gomez-Jimenez for her help with and analysis of the industrial acetylene hydrogenation at JMTC Sonning Common. Similarly, I must thank Dr Glenn Jones of JMTC Pretoria for his DFT computational work along with Tom Hooper and Dr John Hanna of Warwick University for solid state NMR and SQUID analysis of my materials.

A special mention must go to many members of the Tsang group for TEM work, in particular Dr Simon Jones, Dr Simon Fairclough, Dr Amy Kolpin, Dr Hanif Mahadi, Bin Yu and Lizzie Raine. Dr Lewys Jones and Professor Peter Nellist have my thanks for high-resolution TEM, STEM and EELS analysis. Finally, I thank Elisabeth Wolf for her complimentary work as a Part II student under my supervision.

I have much gratitude to the Tsang group, past and present, for general discussion, support, and entertainment throughout my project. In particular: Dr Amy Kolpin, Lizzie Raine, Dr Hanif Mahadi, Bin Yu and Hannah Kreissl. Finally, I would like to thank all of my friends and family who have supported me throughout my time in Oxford. I am sincerely grateful.

Publications

1. I. T. Ellis, E. H. Wolf, G. Jones, B. Lo, M. M. Li, A. P. E. York and S. C. E. Tsang, *Lithium and Boron as Interstitial Palladium Dopants for Catalytic Partial Hydrogenation of Acetylene*, Chemical Communications, 2017, **53**, 601-604.

Interstitial Modification of Palladium for Partial Hydrogenation Reactions

Ieuan T. Ellis

University College

A thesis submitted for the degree of Doctor of Philosophy

Trinity 2016

Abstract

Heterogeneous catalysis is a key industrial process involved in the synthesis of nearly all chemicals currently produced. The environmental impact of these processes is huge so improvements must be made to current catalysts. Should a new material provide better yields at lower energy cost the benefits to both the industry and the planet are significant. There are many ways to change the behaviour of a catalyst, the addition of dopants, the selective blocking of active sites, and changing the strength of the support interaction to name a few. One technique that has become increasingly investigated is interstitial modification, the insertion of a light element into a metal lattice to change the metal's catalytic properties.

The work presented in this thesis devises greener synthetic routes to the known Pd-$^{\text{interstitial}}$B/C catalyst and investigates potential routes to a novel interstitial material, Pd-$^{\text{interstitial}}$Li/C. Initially, successful verification of interstitial modification comes from the characteristic increase in palladium lattice parameter from 3.89 to 4.00 Å and the blocking of the β-hydride formation. Initial catalytic screening determines the synthetic route which yields the most active catalyst which subsequently undergoes thorough characterisation. The wealth of evidence generated confirms the interstitial location of lithium within the palladium lattice, as well as adding to the current understanding of the Pd-$^{\text{interstitial}}$B/C material. EELS analysis on Pd-$^{\text{interstitial}}$B is the closest to direct observation of boron within the palladium lattice to date. PDF on Pd-$^{\text{interstitial}}$Li shows 13.7 % of the palladium octahedral interstitial sites are occupied by lithium. This is the first report of interstitial lithium within palladium to date. The effect of the interstitial modification on catalytic hydrogenation by two elements that have opposite effects on the surface electronics of the host palladium gives intriguing results.

The effect on catalysis varies depending on the conditions investigated. This bank of hydrogenation data allows an informed choice as to which interstitial material would be best suited to the gas or liquid phase catalytic hydrogenation under investigation.

Keywords: Heterogeneous catalysis, Catalyst modification, Interstitial lithium, Interstitial boron, Catalytic hydrogenation, Electronic modification

Contents

List of Figures

List of Tables

Abbreviations

ABF	Annular Bright-Field
AN	Aniline
BCC	Body-Centred Cubic
BRP	1-Bromo-2-Pentyne
BYLP	Becke-Yang-Lee-Parr
CAN	*ortho*-Chloroaniline
CHA	Cyclohexylacetylene
CNB	*ortho*-Chloronitrobenzene
DAP	1-Dimethylamino-2-Pentyne
DCM	Dichloromethane
DFT	Density Functional Theory
DMP	4,4-Dimethyl-2-Pentyne
DOS	Density of States
DPA	Diphenylacetylene
DPE	Diphenylethane
EDX	Energy Dispersive X-ray
EELS	Electron Energy Loss Spectroscopy
EPE	Ethyl 2-Pentynyl Ether
EXAFS	Extended X-ray Absorption Fine Structure

FCC	Face-Centred Cubic
FID	Flame Ionisation Detector
FWHM	Full Width Half Maximum
GC	Gas Chromatography
GPAW	Grid-based Projector Augmented Wave
HAL	Hexan-1-ol
HCP	Hexagonal Close-Packed
HEL	3-Hexen-1-ol
HNN	5-Hexynenitrile
HYL	3-Hexyn-1-ol
LAADF	Low-Angle Annular Dark-Field
MAADF	Medium-Angle Annular Dark-Field
MAS	Magic-Angle Spinning
NB	Nitrobenzene
NMR	Nuclear Magnetic Resonance
PA	Phenylacetylene
PDF	X-ray Pair Distribution Function
PE	Phenylethane
PHP	1-Phenyl-1-Pentyne
PNT	2-Pentyne

RF	Radio Frequency
RHF	Restricted Hartree-Fock
RMSE	Root Mean Square Error
RPBE	Revised Perdew-Burke-Ernzerhof Functional
SQUID	Superconducting Quantum Interference Device
ssNMR	Solid State Nuclear Magnetic Resonance
STB	Stilbene
STEM	Scanning Transmission Electron Microscopy
STY	Styrene
TCD	Thermal Conductivity Detector
TEM	Transmission Electron Microscopy
TGA	Thermogravimetric Analysis
THF	Tetrahydrofuran
TOF	Turnover Frequency
TPR	Temperature Programmed Reduction
XPS	X-ray Photoelectron Spectroscopy
XRD	Powder X-ray Diffraction

1

Introduction

Contents

1.1 Thesis Overview

This thesis consists of seven chapters. Chapters four to six detail the research performed during the course of this DPhil.

Chapter One: This chapter introduces catalysis with a focus on hydrogenation reactions. Interstitial modification is an area of particular interest and the published literature in this area is reviewed.

Chapter Two: Herein the theory and background to the analytical techniques used in this work to characterise catalytic materials are given.

Chapter Three: A detailed description of the experimental methods used in the synthesis, characterisation and catalytic testing of the materials produced throughout the course of this work.

Chapter Four: In this chapter, several synthetic routes to the known material Pd-$^{\text{interstitial}}$B/C are studied along with the synthesis of the novel material, Pd-$^{\text{interstitial}}$Li/C. Preliminary catalytic screening of the materials is conducted.

Chapter Five: Detailed characterisation of both interstitial materials using a range of techniques is conducted. Results are compared to the known interstitial materials in order to have a full understanding of the materials synthesised.

Chapter Six: Here, a range of catalytic tests in several phases are conducted to study how the interstitial modification by B or Li has affected the performance and catalytic characteristics of the materials.

Chapter Seven: The conclusions and future outlook of this work are presented.

1.2 Catalytic Definitions

A catalyst is simply a material which provides an alternative reaction route with a lower activation energy than the uncatalysed reaction.[1] It is necessary for the material not to undergo any permanent change in order to be considered a catalyst. During the process the catalyst can change provided the original material is regenerated upon the conclusion of one catalytic cycle in order to repeat the reaction.[2]

There are three broad areas or types of catalysis: homogeneous, heterogeneous and enzymatic. In homogeneous catalysis it is necessary for both the reagent and the catalyst to be in the same phase (usually liquid). The catalyst itself usually consists of a metal ion supported by a ligand framework. The framework allows for fine control over the behaviour of the catalyst. Catalysts of this type are therefore normally utilised in pharmaceuticals, and in other reactions where the chirality of the products is key. Homogeneous catalytic processes tend to have a more detailed understanding of the reaction process, in terms of a catalytic cycle and the regeneration of the starting catalyst, than the other types.[3] The downsides to homogeneous catalysis are that it is difficult to separate the catalyst from the final product, and the catalyst itself lacks stability when compared to heterogeneous catalysts.

Enzymatic catalysis has its origins in biological processes, and although they are found freely dispersed within the reaction medium they are much larger in mass when compared to a typical homogeneous catalyst. The three-dimensional nature of enzymes gives exceptionally high selectivity and turnover frequency as the reaction centre is bespoke for one particular reaction.[4,5] As enzymes are inherently biological, they are extremely sensitive to pH and temperature making them largely

unsuitable for large scale industrial catalysis.[6]

The third and final grouping is heterogeneous catalysis. Here the reactant and catalyst are in different phases with gas/solid and liquid/solid systems the most common. Indeed this technology can be found in a range of applications from large industrial chemical plants to catalytic converters in underneath most road vehicles.[7] The ease of separation for reactants and products means a vast majority of industrial processes require this type of catalyst despite the actual molecular process on the catalyst's surface being much less well-defined in comparison to homogeneous catalysis. Computational studies and better surface science analysis techniques are improving this aspect of heterogeneous catalysis.[8]

1.3 Early Catalysis

Heterogeneous catalysis has its roots in the early work conducted by Joseph Priestly and Martinus van Marum for alcohol dehydrogenation over metals in the 18th century, though the significance of the metal in their reaction was unknown to them. Between 1813 and 1823 Louis Jacques Thénard, in collaboration with Pierre Dulong, successfully decomposed ammonia over various hot metals.[9] Following this work the first demonstrable reaction of two gases, oxygen and coal gas, over a metal wire leaving the metal unchanged was reported by Humphrey Davy in 1817 in his work on the miners' safety lamp.[10] In 1820, Edmund Davy used platinum to oxidise alcohols before Döbereiner and Thénard observed hydrogen combustion over various metals.[11–13] Following this in 1825, William Henry reported the first supported catalyst, platinum on porcelain, in order to verify Döbereiner's results.[14]

These discoveries led Michael Faraday to review this new area of chemistry in 1834, two years before the term "catalysis" was coined by J.J. Berzelius.[15,16] The newspaper, *Journal des Debats*, upon hearing these results, said:

"this beautiful discovery is going to open up a new field of research in

physics and chemistry".[17]

Industrial catalysis originates with Frédérick Kuhlmann, founder of early chemical giant Établissements Kuhlmann (the remnants of which, after a number of mergers and acquisitions, are part of Rio Tinto Alcan) was granted patents in 1833 for both ammonia and sulphur dioxide oxidation over fine powders of platinum, though at the time the engineering was not available to take full advantage of these discoveries.[9]

It took until 1875 for Clemens Winkler to implement the first industrial catalytic process, the production of sulphuric acid over a Pt catalyst (the "contact process"). This catalyst was used until the First World War interrupted German platinum supplies leading to the switch to vanadium pentoxide, which remains the catalyst of choice to this day.[9] It was the same war which drove the industrialisation of another major catalytic process, the fixation of nitrogen.[18] Wilhelm Ostwald took Kuhlmann's initial ideas on nitric acid synthesis and made them work on a truly industrial scale. By 1904 he had a pilot plant producing 300 kg of nitric acid a day and by 1908 had a plant producing 3 tons a day despite his processes' inefficient use of platinum with the catalyst needing regular replacement.[18]

Meanwhile Fritz Haber, spurred on by his rivalry with Walther Nernst, had by early 1909 succeeded in fixing gaseous nitrogen into ammonia over an iron catalyst before Carl Bosch constructed the first working reactor in 1913.[19,20] The successful fixation of nitrogen, in what is known as the Haber-Bosch process, was a huge boon to Germany during the First World War, allowing the production of armaments without access to Chilean saltpetre and extending the war itself. However, it is in fertilising the land that the process has had the greatest impact on humanity, without the Haber-Bosch it is estimated that there would be two billion fewer people in the world today.[20]

It was around the time of Kuhlmann's efforts that in 1874 von Wilde demon-

strated the first catalytic alkyne hydrogenation, conducting his experiment by mixing two parts acetylene with four parts hydrogen to produce ethane over platinum.[21] These initial studies were expanded upon and generalised by Sabatier in 1897, work which won the 1912 Nobel Prize in chemistry, and gave rise to the principle which bears his name.[22]

1.3.1 Sabatier Principle

The Sabatier principle governs how effective a particular metal will be at catalysing a given reaction. As at least one of the reactants needs to be bound to the catalyst surface, how strongly the reactant interacts with the surface will define how good the metal is at catalysing the reaction. Should the reactant bind too weakly to the surface it will desorb too quickly for a reaction to take place, too strongly and it will not desorb from the surface, leading to poisoning.[1]

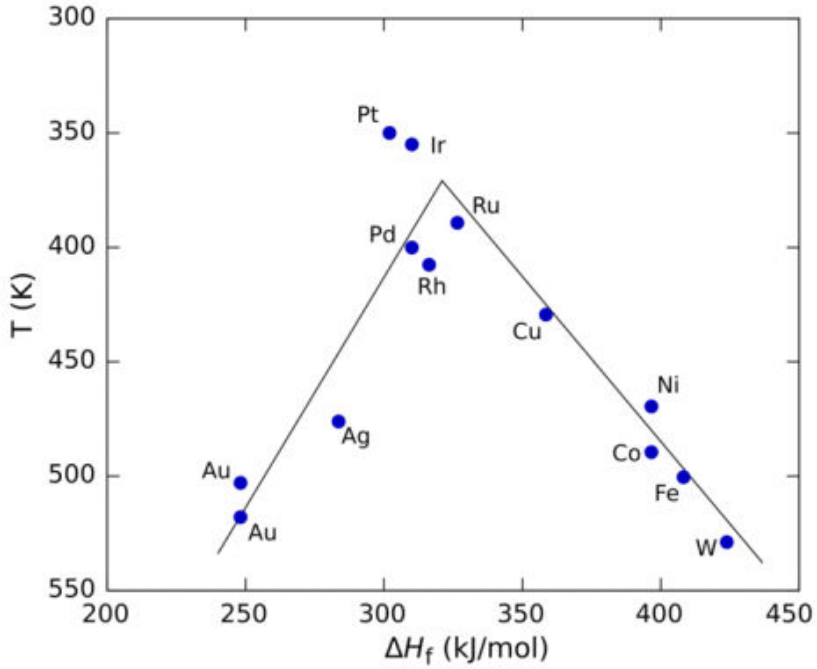

Figure 1.1: A volcano plot illustrating the relationship between formic acid chemisorption to a metal surface and the reactants' decomposition temperature. Reproduced from reference.[23]

As an example, take the decomposition of formic acid over a metal surface. In the decomposition reaction there are two pathways both requiring a dissociatively chemisorbed formate species decomposing into either H_2O and CO, or CO_2 and H_2. Here, activity can be inversely correlated with temperature. As shown in a "volcano plot" for the reaction over a series of metals (Figure 1.1), the activity of formate decomposition was slowest when the adsorption strength was either too weak (Au) or too strong (W), but when the balance between adsorption strength is in the 'sweet spot' the reaction is much faster. This principle holds true for every heterogeneous catalytic reaction and the fine balance between the rates of adsorption of a reactant and desorption of the product controls the conversion and selectivity of a reaction. Fine tuning of a reaction goes beyond simply changing the metal catalyst; changing the support material, the reaction conditions or doping the catalyst are also all well-trodden routes to a selective catalyst.[24]

1.4 Kinetics

1.4.1 Arrhenius

From a fundamental standpoint, the rate of a reaction, k, is governed by the Arrhenius equation (Equation 1.1):

$$k = Ae^{-\frac{E_a}{RT}} \tag{1.1}$$

Where A is a pre-exponential factor, E_a, the activation energy, R, the ideal gas constant and T, temperature. Essentially for any given reaction, the rate is dependent upon temperature. The function of a catalyst is to circumvent the activation energy by providing an alternative pathway for the reaction. This allows lower temperatures to be used and opens up reactions to exploitation which would otherwise be highly unfavourable, for example, ammonia synthesis.

1.4.2 Langmuir-Hinshelwood

Developed by Irving Langmuir and Cyril Hinshelwood in the 1920's, this mechanism details how two molecules, bound at neighbouring adsorption sites react, depending upon their relative concentrations or partial pressures.[25] Taking a unimolecular case, the process of adsorption of a reactant, A, onto a metal site, M, can be simplified to Equation 1.2, with the corresponding rate of adsorption, K_A, given in Equation 1.3:

$$A + M^* \leftrightarrow AM \tag{1.2}$$

$$K_A = \frac{[AM]}{[A][M^*]} \tag{1.3}$$

With $[AM]$, $[A]$ and $[M^*]$ being the corresponding equilibrium concentrations or partial pressures. Given the maximum amount of A that can adsorb to the entire surface is x_{max}, which gives a fractional surface coverage, θ, of 1, a partially covered surface can be defined by Equation 1.4.

$$\theta = \frac{x}{x_{max}} \tag{1.4}$$

Combining Equations 1.3 and 1.4 gives the Langmuir adsorption isotherm for the fractional surface coverage of A (Equation 1.5), assuming that all adsorption sites are equal (something that Langmuir acknowledged not to be the case).[26]

$$\theta_A = \frac{K_A[A]}{1 + K_A[A]} \tag{1.5}$$

Therefore, for a unimolecular reaction (Equation 1.6), the rate can be described as shown in Equation 1.7.

$$A_{(g)} \underset{k_{-1}}{\overset{k_1}{\rightleftharpoons}} A_{(ads)} \underset{k_{-2}}{\overset{k_2}{\rightleftharpoons}} P_{(g)} \tag{1.6}$$

$$k_2\theta_2 = \frac{k_2 K_A[A]}{1 + K_A[A]} \tag{1.7}$$

P is the product of the reaction and k_2 the rate determining step ($k_2 \gg k_1, k_{-2}$ and $K_A = \frac{k_1}{k_{-1}}$). Expanding this understanding to include a second reactant, B, this bimolecular reaction can be described as in Equation 1.8.

$$A_{(g)} \underset{k_{-1}}{\overset{k_1}{\rightleftharpoons}} A_{(ads)} + B_{(g)} \underset{k_{-2}}{\overset{k_2}{\rightleftharpoons}} B_{(ads)} \xrightarrow{k} P_{(ads)} \rightleftharpoons P_{(g)} \tag{1.8}$$

Assuming that the rates of adsorption and desorption of A and B (k_1, k_{-1}, k_2, k_{-2}) are much faster than the rate of reaction between the two adsorbed species (k) then the rate of reaction is directly related to the relative fractional surface coverages of each species (Equation 1.9).

$$rate = k\theta_A\theta_B \tag{1.9}$$

And in terms of the concentrations of the individual species the rate of reaction can be rewritten as Equation 1.10. This is the Langmuir-Hinshelwood mechanism for a bimolecular reaction on a surface.

$$rate = \frac{kK_A[A]K_B[B]}{(1 + K_A[A] + K_B[B])^2} \tag{1.10}$$

1.4.3 Eley-Rideal

Another, less common description for a bimolecular reaction on a surface is the Eley-Rideal mechanism where one of the reactants is adsorbed to the surface and the second reacts directly with this species from the gas phase (Equation 1.11).

$$A_{(g)} \underset{k_{-1}}{\overset{k_1}{\rightleftharpoons}} A_{(ads)} + B_{(g)} \xrightarrow{k} P_{(ads)} \rightleftharpoons P_{(g)} \tag{1.11}$$

However, the assumption cannot be made that B does not at least partially compete

for adsorption sites on the surface, hence the rate equation for this mechanism can be described by Equation 1.12.

$$rate = \frac{kK_A[A][B]}{(1 + K_A[A] + K_B[B])} \tag{1.12}$$

It is possible to distinguish between the two mechanisms experimentally as, unlike the Langmuir-Hinshelwood mechanism, the Eley-Rideal mechanism does not reach a maximum rate when the partial pressures of A and B are changed.

1.5 Hydrocarbon Hydrogenation

The catalytic hydrogenation of alkynes and/or alkenes is a vital industrial process.[27] Everything from the removal of trace alkyne from feedstocks for polymerisation, to vitamin manufacture, to fine chemical and fragrance manufacture is dependent upon this reaction.[28–30] While most late transition metals have some activity towards catalytic hydrogenation, palladium is often the metal of choice.[31]

1.5.1 Horiuti-Polanyi Mechanism

In 1934 Horiuti and Polanyi developed the first mechanism to explain gas phase hydrogenations, proposing that the pathway would most likely involve the adsorption of the unsaturated hydrocarbon to the metal surface through a π-bond interaction. In the presence of hydrogen, H_2 dissociates and adds to the bound hydrocarbon sequentially, taking it through semi-hydrogenated states (i.e. C_2H_3).[32] This mechanism, graphically represented in Figure 1.2 is still used today for the understanding of hydrogenations over metal catalysts.[33,34]

This understanding is rooted in the Langmuir-Hinshelwood reaction mechanism as both species need to be bound to the metal surface for the reaction to proceed. It is important to note that the addition or removal of the initial hydrogen is

highly reversible as deuterium labelled experiments have shown.[34] This lability has consequences when considering the hydrogenation of more complex systems than $C_2H_4 + H_2 \longrightarrow C_2H_6$ such as longer alkene chains, alkynes or molecules with a number of functional groups.

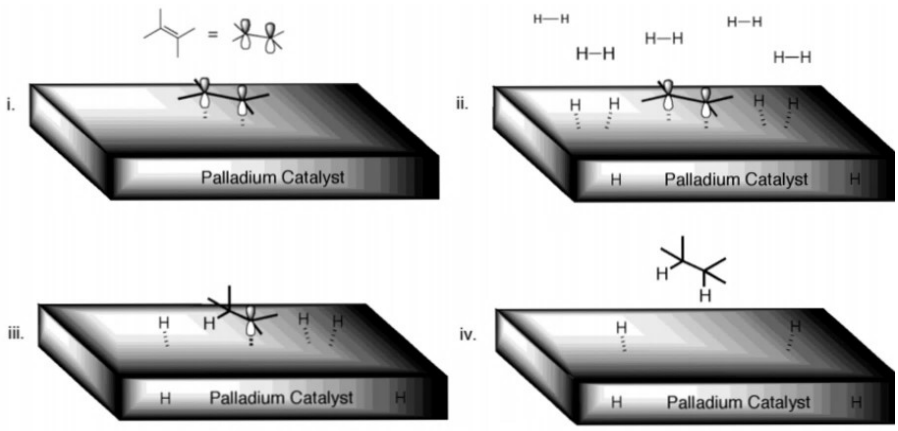

Figure 1.2: The Horiuti-Polanyi mechanism for the reduction of an alkene to alkane on a palladium catalyst. The four steps involved are i) adsorption of the alkane to the metal surface, ii) hydrogen adsorption to the surface, iii) hydrogen migration to the β-carbon causing the formation of a σ-bond between the metal and the α-carbon and finally iv) reductive elimination of the hydrogenated alkane. Figure reproduced from reference.[35]

1.5.2 Alkyne Hydrogenation

Considering an alkyne molecule, the triple bond itself has a linear conformation. The triple bond is broken with the catalytic *syn* addition of one molar equivalent of hydrogen. The orientation of the R groups away from the surface reduces steric hindrance, resulting in the formation of the *cis*-alkene product. At this stage the C=C double bond prevents the formation of the thermodynamically more stable *trans* isomer due to the configuration of the π bond preventing rotation about the C−C axis.[27]

However, should the *cis*-isomer remain resident on (or return to) the catalytic surface after this initial hydrogenation, isomerisation can occur. The initial addition of one atom of hydrogen to the double bond is a highly reversible process, allowing

a [M]-C_xH_{3x-1} intermediate to form. This intermediate has free rotation about the C−C bond which allows the *trans*-isomer to form after the elimination of the added hydrogen. It is also possible that another atom of hydrogen is added to the intermediate giving the fully hydrogenated alkane species.[27,36]

Industrially, for more complex molecules than acetylene hydrogenation, the goal is usually to maintain a very high selectivity toward the *cis*-alkene. In order to achieve this aim, it is therefore necessary to promote the desorption (and prevent the readsorption) of the *cis* isomer before isomerisation or further hydrogenation processes come into play. The alkyne precursor has a much higher relative adsorption strength to the alkene on palladium catalysts so competitive effects can maintain a near 100 % *cis* selectivity until the concentration of the alkyne in the system drops too low.[36] As a natural consequence of this balance between adsorption strength and selectivity however, changing the inherent selectivity of a catalytic system will need the adsorption thermodynamics of either the alkyne and/or alkene to change.[27]

1.6 Particle Effects

Platinum group metals (PGM's) are expensive. The average price for Pt and Pd between June and July 2016 was $1069.82 and $627.41 per ounce respectively.[37] The easiest way to reduce the cost of common catalysts is to reduce the amount of precious metal required. Indeed, reducing the metal size from the bulk to nanoscale regime can both lower the amount of metal in a system and dramatically increase the catalytically active surface area.[38]

For a fuller understanding of the catalytic processes which occur on a nanoparticle it is important to understand the fundamentals of how the properties of metals change in this size regime.

1.6.1 Size Effects

As the size of the metal is reduced to the nanoscale, the catalytic properties of the metal can change dramatically.

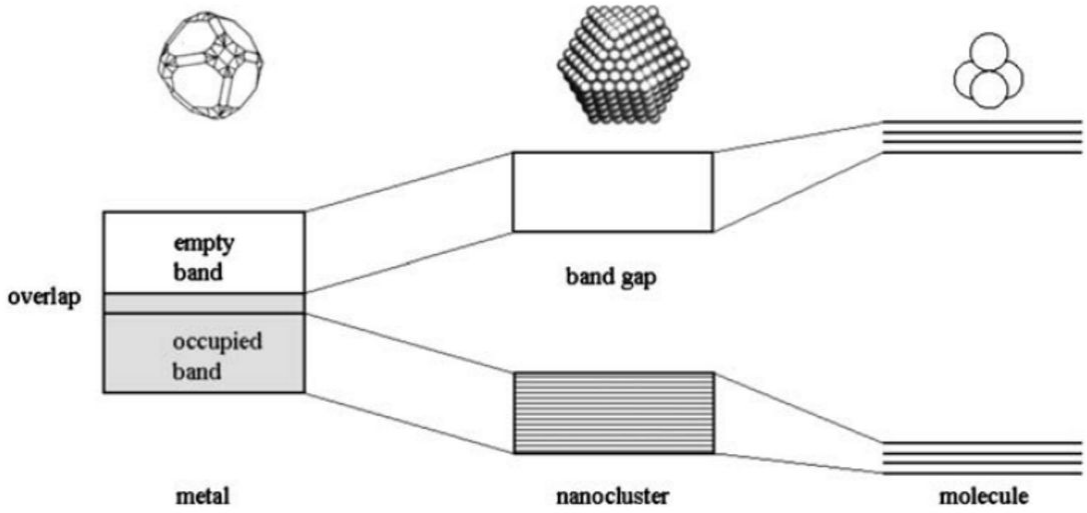

Figure 1.3: A representation of how the band structure of a metal changes with decreasing size, from bulk to nanoparticle to an isolated molecule. Reproduced from reference.[39]

Figure 1.3 shows how the band structure of the metal changes with changing particle size. As the number of atoms tends to infinity (i.e. the bulk form), the gap between overlapping d-orbitals tends to zero, giving rise to a continuous band structure. As the number of atoms in a metal crystal decreases, the spacing between the d-bands increase, eventually giving rise to a discrete band gap. With a further reduction in the number of metal atoms, the band structure becomes essentially molecular in nature.[40]

The nanoparticle regime can be considered intermediate to the extremes of the bulk and molecular forms, though technically a size range of 1 to 100 nm is considered a nanoscale system. A particular example of this is gold. Gold is inert in the bulk form but upon reducing the particle size to approximately 5 nm (Figure 1.4), gold becomes a highly active catalyst for CO oxidation, propene epoxidation and peroxide synthesis.[41–43]

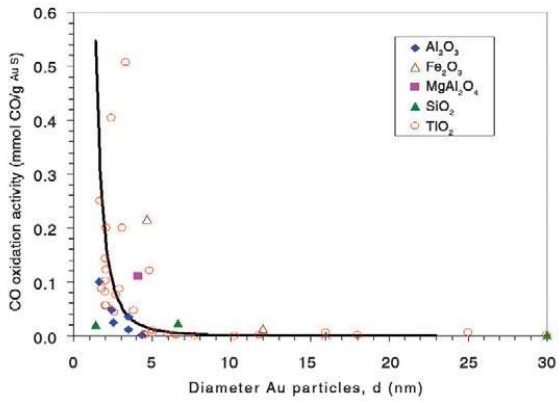

Figure 1.4: A summary of the reported catalytic activity of differently sized Au nanoparticles for CO oxidation at 273 K. Reproduced from reference.[44]

Below 1 nm there is a complete loss of metallic character as the band gap increases to a point where the material acts as an insulator.[39,45,46] Above 100 nm in size the metal is considered to be in its bulk form, though the d-band structure doesn't change significantly for particles greater than 10 nm in size.[43,47] Size, however, does not limit its effects to the d-band structure of the metal.

1.6.2 Geometric Effects

Within a nanoparticle not every atom behaves equally. Taking the gold catalysed CO oxidation example from earlier, some of the increase in activity can be attributed to the increase in low co-ordinate corner sites on the particle.[44] Differences in catalytic activity depending on the specific sites or facets of a nanoparticle are considered the geometric effects upon catalysis.

Taking the ideal cubo-octahedron in Figure 1.5, the particle's surface atoms have a range of different co-ordination numbers. The atoms located wholly within the (111) and (100) planes have co-ordination numbers of 9 and 8 respectively, the (100) and (111), have a co-ordination number of 9. The edge atoms, located at the boundary between two planes and the corner atoms, at the boundary between three planes have lower co-ordination numbers of 7 and 6 respectively.[49] As particles get

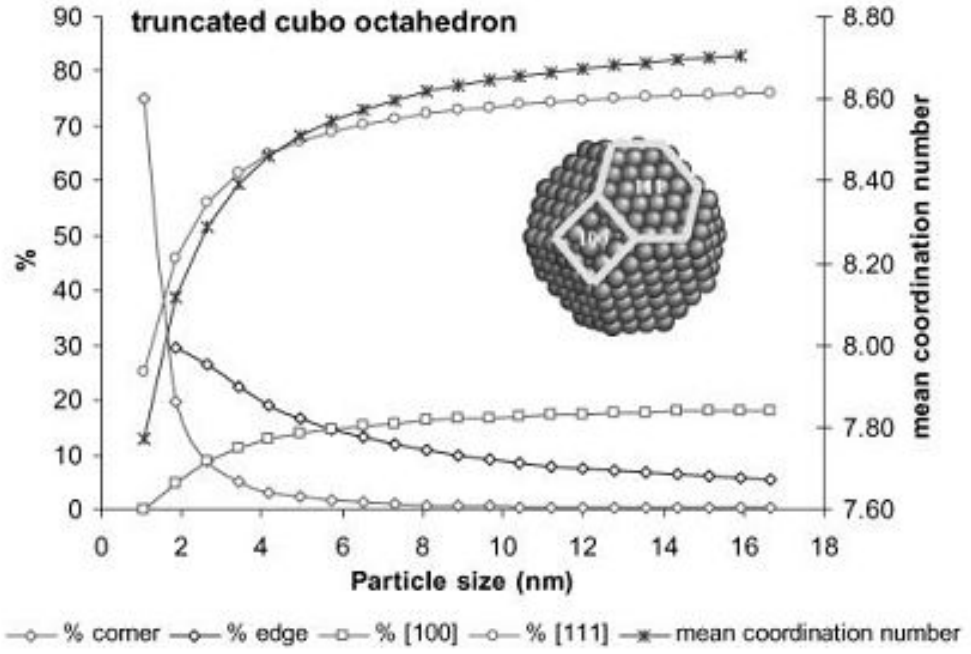

Figure 1.5: The distribution of the different types of sites and mean coordination number of surface atoms with increasing particle size for a theoretically ideal truncated cubo-octahedral particle. Reproduced from reference.[48]

smaller the average co-ordination number of a surface atom decreases. These surface atoms have slightly different catalytic properties as, depending on how saturated the atoms are, reactant molecules will bind differently.

For gold nanoparticles the edges and corners (the lowest co-ordination atoms) exhibit the best activity for CO oxidation due to the reduced binding energy on these sites.[44] Therefore controlling the availability of these sites can be used as a method of controlling a reaction on a metal surface. The easiest way to do this is by controlling particle size.[50] However, this change can also influence the underlying electronics of the nanoparticle in question, and separating out these competing effects can be challenging.[27] To avoid this, more "bulk-like" colloidal nanoparticles, with sizes above the range where electronic effects dominate, have been used to investigate these effects.[51,52] Semagina *et al.* saw an increase in the specific activity of alkyne hydrogenation with increasing particle size in the range of 6 to 14 nm.[53] This contradicts the general assumption that smaller is better when it comes to

catalysis and was attributed to the reaction's preference for terraced sites, the proportion of which increase with increasing particle size.[53,54]

Shape controlled investigations have similarly shed light upon which surface is preferred for some reactions. For example, cubic nanoparticles (i.e. comprised of just the (100) plane) were found to be slightly more active than octahedral particles (the (111) plane exclusively) for the hydrogenation of 2-methyl-3-butyn-3-ol, but selectivity was controlled by the number of low co-ordinate edge and corner sites present. This allowed for the construction of a theoretical "ideal" particle for this reaction.[55] Similarly the Fe (111) facet has been found to be the most active plane for the synthesis of ammonia in the Haber process.[56]

This surface sensitivity can be studied further by controlling the availability of surface sites through the use of ligands, polymers or adatoms which preferentially bind to a particular type of surface atom.[57] Using Bi and Te to selectively decorate Pd nanoparticles (either blocking the low co-ordinate corner/edge sites or the terrace sites respectively) has given insights into the surface sensitivity of hexyne hydrogenations and the mechanism behind formic acid decomposition.[58,59] The advantage of this approach is that the particle size remains almost unchanged, limiting the effect that this will have upon the surface electronics. It is important to remember that these cannot be discounted.

1.6.3 Electronic Effects

As mentioned earlier, changing the particle size not only affects the particle geometry, but also the inherent electronics of the system.[39] Generally, as metal particles get smaller, discrete bands, separated by a band gap, evolve (Figure 1.3). With decreasing particle size a number of concurrent electronic effects occur. Namely, the d-band narrows, causing a shift in the d-band centre to closer to that of the Fermi level. Similarly as the average co-ordination number drops, so does the

corresponding density of states (DOS) at the Fermi level.[27]

These effects have been experimentally observed for small (1 to 6 nm) nanoparticles of Pd supported on graphite where the decrease in size gave rise to a reduction in the density of states at the Fermi level.[60] Similar effects have been seen in other metal nanoparticle systems including Au, Ag, Ni and Cu.[52,61] Even though d-band width, centre position and density of states at the Fermi level are all directly related to particle size, the d-band centre position relative to the Fermi level is generally quoted as it allows the relationship between particle size and surface adsorption properties to be determined.

Nørskov explained this relationship by describing how the surface-adsorbate interaction occurs.[62] As the interaction between an adsorbate and the transition metal s-band contributes little in terms of variations in adsorption strength, the bonding interaction with the metal d-band states governs the binding strength through how close the d-band centre is to the Fermi level.[63] In larger particles, the d-band itself is broad with a centre considerably lower than the Fermi level leading to weaker adsorption due to increased filling of the antibonding adsorbate orbitals. In smaller particles where the d-band centre is closer to the Fermi level, fewer antibonding orbitals are filled resulting in a more strongly adsorbed molecule.[64]

Applying this to the Au catalysed oxidation of CO example shown previously, the reduction in average coordination number as the nanoparticles become smaller than 5 nm causes significant narrowing of the d-band, raising the centre closer to the Fermi level and giving rise to increased CO adsorption strength and enhanced oxidation activity.[64]

As before when considering the electronic effects, the individual surface atoms are not identical in terms of local density of states. The lower the co-ordination number an atom has, say an edge or corner site relative to a terrace site, the closer its localised density of states is to the Fermi level and the stronger the adsorption strength an adsorbate will have on that particular site.[65,66]

The electronic and geometric changes in relation to particle size are most important for the 1 to 5 nm particle range. Above 10 nm the correlation of these effects to just particle size contributions is effectively null.[48,60] Outside of this size dependent range a number of additional modification techniques exist to alter the electronics of the system.

1.6.4 Metal/Support Interaction

An important consideration in catalysis is how the catalyst support interacts with the metal. Metal nanoparticles have high surface energies and will naturally tend to agglomerate into larger, more stable particles.[1] This can be prevented through the use of ligands, like polyvinylpyrrolidone (PVP), attached to the surface of the particle which will prevent agglomeration through electrostatic or steric effects.[67] However, ligand supported nanoparticles are not stable at elevated temperatures, or in conditions where the ligand might leave the metal surface.[68] Metal nanoparticles are therefore very commonly embedded into a solid support. The interaction between the support and the metal immobilises it on the support surface, greatly reducing agglomeration. For industrial materials, the support needs to remain stable under the reaction conditions as well as maintaining the dispersion of the metal. Other factors such as support surface area and mechanical strength also require consideration.[1]

Outside of these physical parameters, the support can play a considerable role in catalysis through charge transfer. Indeed, changing support for otherwise identical materials can cause great differences in catalyst reactivity.[69] The strong metal-support interaction is particularly prevalent with reducible metal oxides such as ceria or titania. The support itself can be reduced from M^{4+} to M^{3+} producing an electron rich metal oxide with some of that charge donated to the metal catalyst, though this effect is reversible should the support be re-oxidised.[23] Some geometric changes in the metal surface can similarly be attributed to this electronic

donation.[23] Greater changes in the catalytic metal structure can be explained though lattice mismatch between the two materials, causing strain and distorting the metal lattice.[70,71] The strength of the support interaction can even cause discrepancies in characterisation techniques, such as CO chemisorption for surface area determination, as the underlying assumptions in this method do not allow for any electronic modification or structural changes beyond the straight-forward particle size/surface area relationship. The particle shape on the surface changes (Figure 1.6) depending how interacting the metal is with the support material.[72]

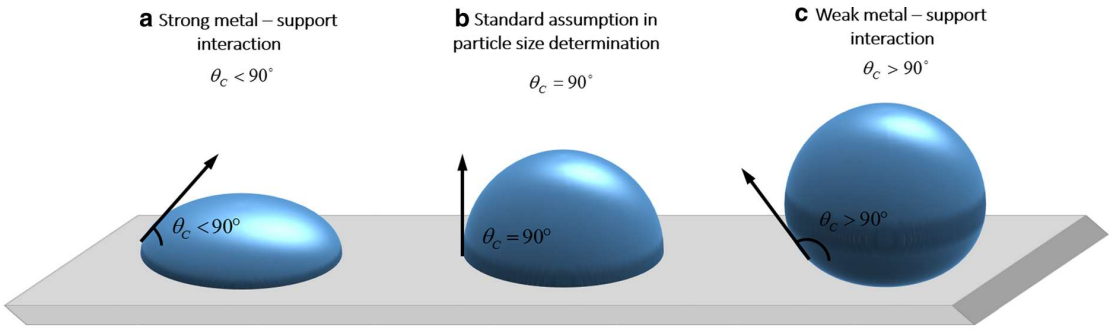

Figure 1.6: The effect of metal support on the geometry of a typical metal nanoparticle. Reproduced from reference.[72]

One example of this is shown where Pd carefully deposited onto graphite can be templated into an hexagonal close-packed arrangement instead of its usual face-centred cubic lattice arrangement.[73]

With a very strong metal/support interaction some interesting effects can be seen. For example, Tauster *et al.* observed a decrease in H_2 chemisorption for various transition metals (Pt, Pd, Rh, Ru, Ir and Os) supported on TiO_2.[74] Heating these materials in O_2 restored their chemisorption behaviour.[74] Fractional coverage of the active metal by partially reduced TiO_x species was blocking adsorption sites, having an overall negative effect. However, for redox active oxides such as ceria, catalytic activity can be enhanced despite a considerable drop in metal surface area.[75] The two proposed mechanisms in action are: the spillover of a very mobile active hydrogen species from the metal to the support,[76] and an electronic

interaction between the metal and the metal oxide.[75,77] Acerbi *et al.* investigated the competing mechanisms in action to explain this activity enhancement.[78] It was found that the electronic properties of the metal drive hydrogen chemisorption (and dissociation) on the metal surface.

It was concluded that the strong metal/support interaction is related to the electronic nature of the catalytic system, i.e. the spillover effect is a direct consequence of the electronic structure of the metal when the metal is partially exposed.[78]

1.7 Interstitial Modification of Palladium

Interstitial modification is the selective blocking of a hole, usually octahedral, within a metal lattice by a small atom.[79] The insertion of a light element can have a quite profound influence on the properties of the host lattice. For example, a small amount of carbon located in the interstitial sites of iron gives steel, and increasing the carbon content gives increasingly hard, but less ductile steel.[80]

Once inserted, these small atoms have interesting effects on the geometry and electronics of palladium which has a direct impact on its Fermi level (ϵ_f) and density of states, and thus allows the metal to be tuned as a catalyst. In 1931 Hägg proposed some geometric criteria which these small atoms have to fulfil if they are to enter the lattice, namely that the ratio between the transition metal (R_M) and the interstitial element (R_I) radii must be less than 0.59.[81,82]

Interstitial systems are not typical alloy systems in that an atom from the host lattice is not replaced by the dopant, instead an additional atom is added into the vacant holes in the lattice. Vegard's law can be used for substitutional alloy systems. This law states that the lattice parameter of a solid solution of two constituents is approximately equal to the two constituents' lattice parameters at the same temperature.[83–85] However for interstitial systems this law breaks down as a host lattice expansion is typical, regardless of the lattice parameter of the

dopant.[86] It is also possible to use the atomic radii of the elements in question, provided they are of a similar size.[85] The law would not be viable therefore for an interstitial system with a large difference in atomic radii.

1.7.1 Palladium Hydride (Pd-$^{\text{interstitial}}$H)

The most common interstitial palladium system is that of palladium hydride.[87] The first theories trying to understand the behaviour of hydrogen with palladium came in the late 1860's through the work of Thomas Graham who believed that hydrogen bonds were constantly being broken and reformed as hydrogen entered and departed the system.[88–90] The modern understanding is that the palladium hydrogen system has two phases, α and β (sometimes co-existing) depending on hydrogen pressure, temperature and concentration.[91]

Hydrogen easily diffuses throughout the lattice, and naturally forms an equilibrium with palladium at temperatures from 167 K to as low as 100 K.[92–94] Pd−H decays, depending on the partial pressure of hydrogen, between below 327 to 427 K.[95] The bonding of Pd−H is well understood and was summarised by Flanagan and Oates who say that there is a small charge transfer from the H 1s to the Pd 4d orbitals with the effective Pd−H interaction barely extending beyond the nearest Pd neighbours.[96] There is some narrowing of the Pd 4s DOS due to hybridisation with H leading to a higher Fermi energy.[96]

Physically, a dilute Pd-$^{\text{interstitial}}$H phase forms (the α phase) with initial hydrogen absorption. This leads to a slight increase in lattice parameter, from the bulk value of 3.89 to 3.90 Å.[97] With increasing hydrogen absorption, the lattice undergoes a phase change to the β phase, where the palladium lattice sharply expands to a maximum value of approximately 4.00 Å, allowing (under standard conditions) up to 70 % of the octahedral sites to be filled with interstitial hydrogen.[91] Throughout this phase change, which can be reversed with reduction in H concentration, the

palladium maintains a face-centred cubic structure.[98] The nature of the phase change from α to β is not completely clear.[99] A recent study by Ulvestad *et al.* studying the strain induced by interstitial hydrogen as it enters a palladium nanocube observed a co-existence of both phases.[100] It was seen that an excess of hydrogen in the α phase and deficiency in the β phase enhanced the magnitude of the strain field *via* stress-driven diffusion.

It is interesting to note that the hydrogen isotopes, deuterium and tritium, behave in a very similar manner with palladium. The β-phase transition is observed and a similar amount of each isotope can be located interstitially.[101–103] Due to tritium's relatively short half-life, palladium tritide can give rise to localised bubbles of helium deforming the host metal. Interstitial helium was thought unlikely to form but could not be ruled out by the authors.[104]

1.7.2 Palladium Carbide (Pd-$^{\text{interstitial}}$C)

The palladium carbide system was observed by Zaidi through studies of ethylene acetoxylation over palladium, though at the time it was misassigned to palladium hydride.[105] Ziemecki built upon these initial observations and studied the Pd-$^{\text{interstitial}}$C binary and Pd-$^{\text{interstitial}}$H,C ternary systems. It was concluded that the maximum occupancy of carbon in the lattice is 15 %, where the free octahedral sites can be filled with hydrogen at lower carbon occupancy levels.[106,107] This blocking of the octahedral sites by carbon, preventing the insertion of hydrogen, is a good initial indicator of the formation of an interstitial palladium species.

It was shown that Pd-$^{\text{interstitial}}$C generated *in-situ* (from fragments of acetylene gas decomposing on the metal surface during the reaction) can selectively hydrogenate alkynes. This required careful control over the gases as the C fragments occupying the lattice sites were hydrogenated out of the lattice as methane if the flow of H_2 was too great.[108] These catalysts are normally loaded onto a carbon support which

is assumed to have no influence on the reaction.[109] Recent work within the Tsang group by Chan demonstrated an efficient protocol for the synthesis of palladium with interstitial carbon, to the maximum loading of 15 %, prior to use as a selective catalyst for a number of reactions.[110] The palladium lattice again underwent the β-phase change, increasing the lattice parameter to 3.99 Å.[111]

Interestingly, the energy of the C 2p electrons and the Pd 4d electrons are almost degenerate resulting in a very strong interaction between the two, with most of the C electrons donated to the Pd 4d at just above the Fermi level, with the electronic potential of C quite localised to the carbon atom.[79,86,112]

1.7.3 Palladium Boride (Pd-$^{\text{interstitial}}$B)

Historically, palladium boron has been studied as an ordered substitutional Pd_xB_y alloy, with most analytical study conducted on this material.[79,113–115] By the mid 1970's Brodowsky had confirmed that B could occupy the octahedral sites of palladium, but could not provide an explanation as to why B can enter the lattice. Theoretically, following Hägg's rule ($\frac{R_M}{R_I} = 0.67$ for Pd-$^{\text{interstitial}}$B) boron is too large to fit. Brodowsky therefore proposed that there should be an electronic interaction between the valence electrons of B and the 4d and 5s bands of palladium.[115–117] The maximum loading of B into the lattice was found experimentally to be 20 %, comparable to the Pd-$^{\text{interstitial}}$C system.[114,118] This material had no catalytic use as the original syntheses of Pd-$^{\text{interstitial}}$B required high temperatures, bulk palladium and used toxic B sources.[119–121]

Further work by Chan *et al.* uncovered a low temperature synthesis for a carbon supported Pd-$^{\text{interstitial}}$B catalyst, as well as conducting DFT calculations on the bonding within the system. These calculations showed that there is a considerable overlap between the B 2p and Pd 4d with an electronic transfer to the B from the Pd.[122] This is in agreement with Bakker *et al.* who stated that, similar to C, the B

2p band is almost degenerate with the Pd 4d band resulting in a strong interaction. Unlike carbon the boron potential has a longer range, i.e. it is less localised on the interstitial atom.[79] The interstitial doping by boron (and indeed carbon), has the effect of broadening the palladium d band, and decreasing the electron density at the Fermi level of the metal.[111,122] Catalytically, Pd-$^{\text{interstitial}}$B has been found to be particularly well suited to selective hydrogenations and formic acid decomposition, as well as having improved stability in comparison to the carbon system.[120,123]

1.7.4 Other Interstitial Palladium Systems

For interstitial oxygen, a recent detailed study by Gegner *et al.* went through the contradictory historical literature and, with their own experimental work, concluded that oxygen does dissolve atomically into the palladium lattice. This in turn leads to quick internal oxidation of the metal.[124] Catalytically interstitial oxygen in palladium can be applied to high temperature CO oxidation where it has been observed to act as a crucial intermediate in the formation of CO_2. In contrast to typical palladium oxide, Pd-$^{\text{interstitial}}$O is heavily dependent on the pressure of oxygen and temperatures used.[125,126] The transient nature of the Pd-$^{\text{interstitial}}$O species means that attempts to synthesise it at room temperature, similar to the methods applied to Pd-$^{\text{interstitial}}$B and Pd-$^{\text{interstitial}}$C would ultimately be unsuccessful and have not been attempted.

There is very little evidence toward the formation of a stable Pd-$^{\text{interstitial}}$N species. Veith *et al.* studied the synthesis of palladium nitrides through physical vapour deposition and found that, while substitutional Pd_xN_y alloys were made, interstitial nitrogen was not seen.[127] Interstitial nitrogen has been seen transiently in vanadium materials but not as a stable compound.[128]

A number of binary Pd−F species exist but none as an interstitial system, a computational study by Gelatt Jr. *et al.* on a Pd−F system found no overlap between the fluorine p orbital and palladium 4d orbital, which is present in the other

known Pd interstitials (excluding palladium hydride).[86,129] Pd-$^{\text{interstitial}}$Li is another system that has not been examined before, though the ordered alloy system is again well understood.[130,131] This material has been mentioned in passing as a potential species in some electrochemical work and in the dubious field of cold fusion.[132,133] Outside of this the same study by Gelatt Jr. saw a minimal overlap between the Li s orbital and the Pd 4d suggesting that it will have a greater likelihood of being a stable system than a Pd-$^{\text{interstitial}}$F system.[86]

1.8 Computational Methods

Recently, with the advances in computational power and speed, new avenues in material investigation have become available.[66] The effects of alloying, lattice expansion, and interstitial modification on metal electronic and geometric properties have all been investigated.[8,70,122,134,135] This work is typically used in conjunction with other empirical results to explain phenomena seen experimentally, though it can also be used to independently predict catalytic results.[66]

Density functional theory (DFT) is commonly used for this work as it allows for larger systems to be modelled without an extreme computational cost. This is done by using a set of one-electron Schrödinger equations (Kohn-Sham equations) to describe the system.[66] Catalytic surfaces are often reduced to a small cluster, where only the atoms around the active site are modelled; the contributions of atoms further away are considered negligible. The alternative representation of a catalyst is that of a slab. Here, a repeating unit several atomic layers deep (i.e. the super cell) with an area large enough to minimise adsorbate-adsorbate interactions is utilised (Figure 1.7).[66]

Other parameters under consideration in a DFT calculation are the basis set and the exchange-correlation function.[66] The basis set provides an approximation to simplify the Kohn-Sham equations for the electron orbitals within a system. As

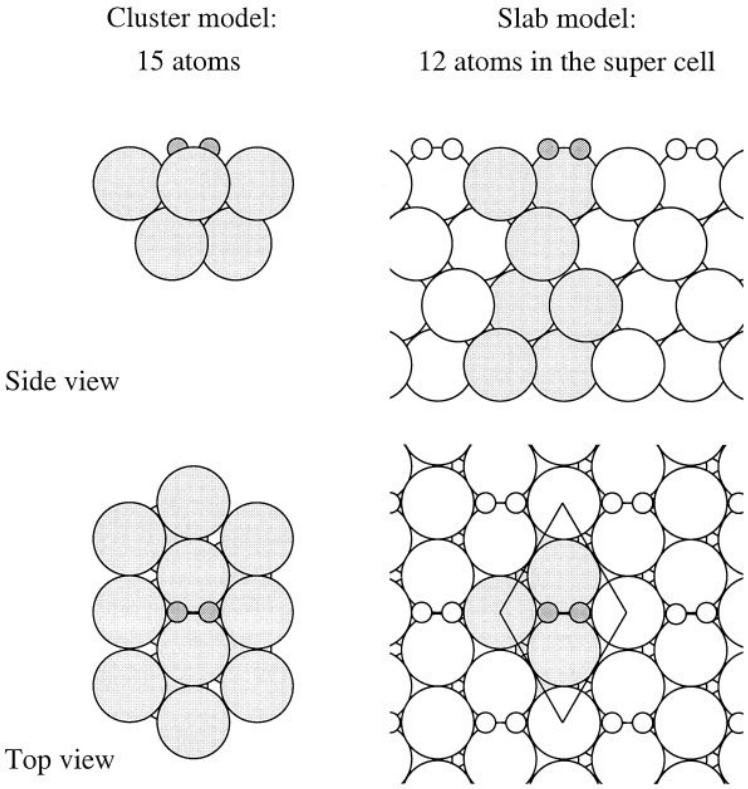

Figure 1.7: Cluster and slab representations of hydrogen on a semi-infinite surface. Shaded atoms represent atoms within the super cell, whereas unshaded are repeat units of the super cell. Reproduced from reference.[66]

valence electrons dominate bonding interactions they are modelled as a free electron gas in an infinite solid (a plane wave) and the exchange-correlation function is used to reduce the errors seen in approximating the interaction between the one electron wavefunctions.[66] DFT calculations describe the electronics of the system in terms of the d-band centre and the Fermi level. Changes to this value through alloying, doping or interstitial modification, relative to that of various adsorbates can be used to determine the strength of an adsorbate-surface bond using the Sabatier principle (Section 1.3.1).[66,70,134,136]

1.9 Aims and Objectives

1.9.1 Why Interstitially Modify Palladium?

There are a number of advantages to focussing on interstitial chemistry as a palladium modification technique. From a purely structural point of view, the blocking of β-hydride formation, a known cause of over-hydrogenation, will improve catalytic selectivity.[137] Beyond this, as the modification is sub-surface, the active area of palladium is not reduced unlike other techniques which require site blocking.[59]

Interstitial boron has the effect of lowering electron density at the Fermi level of the palladium host and we postulate that the insertion of lithium into the palladium lattice will have the opposite effect. Lithium doping will result in electron donation to palladium, causing an increase in the electron density at the Fermi level. These two opposite effects will influence not only the rate of hydrogenation, but the final product composition too (i.e. the ratio of the *cis*/*trans* products and the rate of over-hydrogenation).

1.9.2 Aims

The overarching aim of this thesis is the investigation of interstitial palladium materials and their use in a range of catalytic reactions. How the interstitial dopant affects both the physical structure and electronic structure of the palladium host lattice will be studied. To this aim, the known Pd-$^{\text{interstitial}}$B system will be synthesised, and as a comparison, the novel Pd-$^{\text{interstitial}}$Li system will be synthesised for the first time. These two interstitial systems will undergo testing in a range of catalytic hydrogenations in comparison to unmodified Pd to study the effect of this modification.

1.9.3 Objectives

In summary, the objectives are:

- Explore other synthetic routes to the known Pd-$^{\text{interstitial}}$B catalyst and explore synthetic routes to the novel Pd-$^{\text{interstitial}}$Li catalyst. Initial catalytic screening will be undertaken to elucidate the route to the most active materials.
- Comprehensively characterise both systems through a range of simple to more advanced techniques.
- Study how catalytic performance of the materials has changed following doping with either boron or lithium.

1.10 References

(1) J. M. Thomas and W. J. Thomas, *Principles and Practice of Heterogeneous Catalysis*, Wiley-VCH Verlag GmbH & Co. KGaA, Weinheim, Germany, 1997.

(2) J. Hagen, *Industrial Catalysis: A Practical Approach*, Wiley-VCH Verlag GmbH & Co. KGaA, Weinheim, Germany, 2nd edn., 2006.

(3) G. F. Swiegers, *Mechanical Catalysis: Methods of Enzymatic, Homogeneous, and Heterogeneous Catalysis*, John Wiley & Sons, Hoboken, New Jersey, 2008.

(4) I. B. Wilson and M. A. Harrison, *The Journal of Biological Chemistry*, 1961, **236**, 2292–2295.

(5) *Enzyme Biocatalysis: Principles and Applications*, ed. A. Illanes, Springer, 2008.

(6) *Sustainable Industrial Chemistry: Principles, Tools and Industrial Examples*, ed. F. Cavani, G. Centi, S. Perathoner and F. Trifirò, Wiley-VCH Verlag GmbH & Co. KGaA, Weinheim, Germany, 2009.

(7) R. A. Sheldon, I. W. C. E. Arends and U. Hanefeld, *Green Chemistry and Catalysis*, Wiley-VCH Verlag GmbH & Co. KGaA, Weinheim, Germany, Feb. 2007.

(8) C. Hu, S. W. Ting, K. Y. Chan and W. Huang, *International Journal of Hydrogen Energy*, 2012, **37**, 15956–15965.

(9) A. J. B. Robertson, *Platinum Metals Review*, 1975, **19**, 64–69.

(10) H. Davy, *Philosophical Transactions of the Royal Society of London*, 1817, **107**, 77–85.

(11) E. Davy, *Philosophical Transactions of the Royal Society of London*, 1820, **110**, 108.

(12) P. L. Dulong and L. J. Thenard, *Annales de Chimie et de Physique*, 1823, **11**, 440.

(13) J. W. Döbereiner, *Annales de Chimie et de Physique*, 1823, **24**, 91–96.

(14) W. Henry, *Philosophical Magazine Series 1*, 1825, **65**, 269–283.

(15) M. Faraday, *Philosophical Transactions of the Royal Society of London*, 1834, **124**, 55–76.

(16) J. J. Berzelius, *Edinburgh New Philosophical Journal*, 1836, **21**, 223–228.

(17) D. McDonald and L. B. Hunt, *A History of Platinum and its Allied Metals*, Europa Publications Limited, London, 1982.

(18) L. B. Hunt, *Platinum Metals Review*, 1958, **2**, 129–134.

(19) T. Hager, *Alchemy of the Air: A Jewish Genius, a Doomed Tycoon, and the Scientific Discovery That Fed the World but Fueled the Rise of Hitler*, Three Rivers Press, New York, 2008.

(20) V. Smil, *Nature*, 1999, **400**, 1999.

(21) M. P. von Wilde, *Berichte der deutschen chemischen Gesellschaft*, 1874, **7**, 352–357.

(22) P. Sabatier and J.-B. Senderens, *Comptes rendus hebdomadaires des séances de l'Académie des sciences*, 1897, **124**, 1392–1395.

(23) *Ullmann's Encyclopedia of Industrial Chemistry*, ed. H. Knözinger and H. Kochloefl, Wiley-VCH Verlag GmbH & Co. KGaA, Weinheim, Germany, 2000.

(24) *Handbook of Heterogeneous Catalysis*, ed. G. Ertl, H. Knözinger, F. Schüth and J. Weitkamp, John Wiley & Sons, 1999.

(25) I. Langmuir, *Journal of the American Chemical Society*, 1918, **40**, 1361.

(26) I. Langmuir, *Transactions of the Faraday Society*, 1922, **17**, 607.

(27) G. C. Bond, *Metal-Catalysed Reactions of Hydrocarbons*, Springer, New York, 2005.

(28) B. Chen, U. Dingerdissen, J. G. E. Krauter, H. G. J. Lansink Rotgerink, K. Möbus, D. J. Ostgard, P. Panster, T. H. Riermeier, S. Seebald, T. Tacke and H. Trauthwein, *Applied Catalysis A: General*, 2005, **280**, 17–46.

(29) *Nanoparticles and Catalysis*, ed. D. Astruc, Wiley-VCH Verlag GmbH & Co. KGaA, Weinheim, Germany, 2007.

(30) R. A. Sheldon and H. van Bekkum, *Fine Chemicals through Heterogeneous Catalysis*, Wiley-VCH Verlag GmbH & Co. KGaA, Weinheim, Germany, 2000.

(31) Y. Chen, B. He and H. Liu, *Journal of Materials Science & Technology*, 2005, **21**, 187–190.

(32) I. Horiuti and M. Polanyi, *Transactions of the Faraday Society*, 1934, **30**, 1164–1172.

(33) J. Osswald, K. Kovnir, M. Armbruster, R. Giedigkeit, R. Jentoft, U. Wild, Y. Grin and R. Schögl, *Journal of Catalysis*, Aug. 2008, **258**, 219–227.

(34) B. Mattson, W. Foster, J. Greimann, T. Hoette, N. Le, A. Mirich, S. Wankum, A. Cabri, C. Reichenbacher and E. Schwanke, *Journal of Chemical Education*, May 2013, **90**, 613–619.

(35) K. L. Amezcua, T. J. Mull, A. L. Mayhugh and D. B. Cordes, *International Journal of Undergraduate Research and Creative Activities*, 2015, **7**, Article 5.

(36) J. G. Ulan and W. F. Maier, *Journal of Molecular Catalysis*, 1989, **54**, 243–261.

(37) *Johnson Matthey PMM Prices*, http://www.platinum.matthey.com/prices, Accessed: 27-06-2016.

(38) P. Stoltze, *Introduction to heterogeneous catalysis*, Michael J. Fink, Aalborg, 2012.

(39) *Metal Nanoclusters in Catalysis and Materials Science: The Issue of Size Control*, ed. B. Corain, G. Schmid and N. Toshima, Elsevier, Amsterdam, 2008.

(40) K. W. Kolasinski, *Surface Science: Foundations of Catalysis and Nanoscience*, John Wiley and Sons, Ltd, Chichester, 3rd edn., 2012.

(41) P. J. Miedziak, S. A. Kondrat, N. Sajjad, G. M. King, M. Douthwaite, G. Shaw, G. L. Brett, J. K. Edwards, D. J. Morgan, G. Hussain and G. J. Hutchings, *Catalysis Science & Technology*, 2013, 2910–2917.

(42) M. Haruta, T. Kobayashi, H. Sano and N. Yamada, *Chemistry Letters*, 1987, **16**, 405–408.

(43) *Nanocatalysis*, ed. U. Heiz and U. Landman, Springer, Berlin, 2007.

(44) B. Hvolbæk, T. Janssens, B. Clausen, H. Falsig, C. Christensen and J. Nørskov, *Nano Today*, 2007, **2**, 14–18.

(45) F. Aguilera-Granja, S. Bouarab, A. Vega, J. A. Alonso and J. M. Montejano-Carrizales, *Solid State Communications*, 1997, **104**, 635–639.

(46) J. Zhao, X. Chen and G. Wang, *Physical Review B*, 1994, **50**, 15424–15426.

(47) *Handbook of Nanostructured Materials and Nanotechnology*, ed. H. S. Nalwa, Elsevier, Amsterdam, 2000.

(48) D. Uzio and G. Berhault, *Catalysis Reviews*, 2010, **52**, 106–131.

(49) H. G. Fritsche and R. E. Benfield, *Zeitschrift für Physik D: Atoms, Molecules and Clusters*, 1993, **26**, 15–17.

(50) M. Boudart, A. Aldag, J. E. Benson, N. A. Dougharty and C. Girvin Harkins, *Journal of Catalysis*, 1966, **6**, 92–99.

(51) T. Teranishi and M. Miyake, *Chemistry of Materials*, 1998, **10**, 594–600.

(52) C. N. R. Rao, G. U. Kulkarni, P. J. Thomas and P. P. Edwards, *Chemistry - A European Journal*, 2002, **8**, 28–35.

(53) N. Semagina, A. Renken, D. Laub and L. Kiwiminsker, *Journal of Catalysis*, Mar. 2007, **246**, 308–314.

(54) N. Semagina, A. Renken and L. Kiwi-Minsker, *The Journal of Physical Chemistry C*, 2007, **111**, 13933–13937.

(55) M. Crespo-Quesada, J.-M. Andanson, A. Yarulin, B. Lim, Y. Xia and L. Kiwi-Minsker, *Langmuir*, June 2011, **27**, 7909–16.

(56) N. Spencer, R. Schoonmaker and G. Somorjai, *Journal of Catalysis*, 1982, **74**, 129–135.

(57) Y. J. Tong, *Chemical Society reviews*, 2012, **41**, 8195–209.

(58) J. A. Anderson, J. Mellor and R. P. K. Wells, *Journal of Catalysis*, 2009, **261**, 208–216.

(59) S. Jones, S. M. Fairclough, M. Gordon-Brown, W. Zheng, A. Kolpin, B. Pang, W. C. H. Kuo, J. M. Smith and S. C. E. Tsang, *Chem. Commun.*, 2015, **51**, 46–49.

(60) H. N. Aiyer, V. Vijayakrishnan, G. N. Subbanna and C. N. R. Rao, *Surface Science*, 1994, **313**, 392–398.

(61) V. Vijayakrishnan, A. Cbainani, D. D. Sarma and C. N. R. Rao, *The Journal of Physical Chemistry*, 1992, **96**, 8679–8682.

(62) B. Hammer and J. K. Nørskov, *Why gold is the noblest of all the metals*, 1995.

(63) A. Nilsson, L. G. M. Pettersson, B. Hammer, T. Bligaard, C. H. Christensen and J. K. Nørskov, *Catalysis Letters*, 2005, **100**, 111–114.

(64) A. Visikovskiy, H. Matsumoto, K. Mitsuhara, T. Nakada, T. Akita and Y. Kido, *Physical Review B - Condensed Matter and Materials Physics*, 2011, **83**, 1–9.

(65) C. Mottet, G. Tréglia and B. Legrand, *Surface Science*, 1996, **352-354**, 675–679.

(66) B. Hammer and J. Nørskov, *Advances in Catalysis*, 2000, **45**, 71–129.

(67) K. Tedsree, C. W. A. Chan, S. Jones, Q. Cuan, W.-K. Li, X.-Q. Gong and S. C. E. Tsang, *Science*, 2011, **332**, 224–228.

(68) K. Tedsree, T. Li, S. Jones, C. W. A. Chan, K. M. K. Yu, P. A. J. Bagot, E. A. Marquis, G. D. W. Smith and S. C. E. Tsang, *Nature Nanotechnology*, 2011, **6**, 302–307.

(69) W.-J. Shen, M. Okumura, Y. Matsumura and M. Haruta, *Applied Catalysis A: General*, 2001, **213**, 225–232.

(70) M. Mavrikakis, B. Hammer and J. Nørskov, *Physical Review Letters*, 1998, **81**, 2819–2822.

(71) C. R. Henry, *Surface Science Reports*, 1998, **31**, 231–325.

(72) L. Torrente-Murciano, *Journal of Nanoparticle Research*, 2016, **18**, 87.

(73) J. Walter, J. Heiermann, G. Dyker, S. Hara and H. Shioyama, *Journal of Catalysis*, Jan. 2000, **189**, 449–455.

(74) S. J. Tauster, S. C. Fung and R. L. Garten, *Journal of the American Chemical Society*, 1978, **100**, 170–175.

(75) S. E. Golunski, H. A. Hatcher, R. R. Rajaram and T. J. Truex, *Applied Catalysis B: Environmental*, 1995, **5**, 367–376.

(76) L. S. F. Feio, C. E. Hori, S. Damyanova, F. B. Noronha and W. H. Cassinelli, *Applied Catalysis A: General*, 2007, **316**, 107–116.

(77) L. F. Liotta, A. Longo, A. Macaluso, A. Martorana, G. Pantaleo, A. M. Venezia and G. Deganello, *Applied Catalysis B: Environmental*, 2004, **48**, 133–149.

(78) N. Acerbi, S. C. E. Tsang, G. Jones, S. Golunski and P. Collier, *Angewandte Chemie - International Edition*, 2013, **52**, 7737–7741.

(79) H. L. M. Bakker, M. J. C. de Jong, P. M. Oppeneer, R. Griessen, A. Lodder, R. Vis and H. Brodowsky, *Journal of Physics F: Metal Physics*, 1986, **16**, 707–720.

(80) P. R. Knowles, *Design of Structural Steelwork*, Taylor & Francis, Glasgow, 2nd edn., 2005.

(81) G. Hägg, *Zeitschrift für Physikalische Chemie B*, 1929, **12**, 221.

(82) G. Hägg, *Zeitschrift für Physikalische Chemie B*, 1931, **12**, 33.

(83) Y. Sakamoto, F. L. Chen, J. Muto and T. B. Flanagan, *Zeitschrift für Physikalische Chemie*, Jan. 1991, **173**, 235–250.

(84) L. Vegard, *Zeitschrift für Physik*, 1921, **5**, 17–26.

(85) A. R. Denton and N. W. Ashcroft, *Physical Review A*, 1991, **43**, 3161–3164.

(86) C. D. Gelatt, Jr., A. R. Williams and V. L. Moruzzi, *Physical Review B*, 1983, **27**, 2005–2013.

(87) F. D. Manchester, A. San-Martin and J. M. Pitre, *Journal of Phase Equilibria*, 1994, **15**, 62–83.

(88) T. Graham, *Philosophical Transactions of the Royal Society of London*, 1866, **156**, 399–439.

(89) T. Graham, *Proceedings of the Royal Society of London*, 1868, **17**, 500–506.

(90) T. Graham, *Proceedings of the Royal Society of London*, 1868, **17**, 422.

(91) F. A. Lewis, *Platinum Metals Review*, 1982, **26**, 20–27.

(92) T. Curran, T. B. Flanagan and W. A. Oats, *Journal of the Chemical Society, Faraday Transactions 1: Physical Chemistry in Condensed Phases*, 1973, **69**, 449–458.

(93) H. Hemmes, A. Driessen, R. Griessen and M. Gupta, *Physical Review B*, 1989, **39**, 4110–4118.

(94) V. F. Rybalko, A. N. Morozov, I. M. Neklyudov and V. G. Kulish, *Physics Letters A*, 2001, **287**, 175–182.

(95) S. B. Ziemecki and G. A. Jones, *Journal of Catalysis*, Oct. 1985, **95**, 621–622.

(96) T. B. Flanagan and W. A. Oates, *Annual Review of Materials Science*, 1991, **21**, 269–304.

(97) J. A. Eastman, L. J. Thompson and B. J. Kestel, *Physical Review B*, 1993, **48**, 84.

(98) W. Auer and H. J. Grabke, *Berichte der Bunsengesellschaft für physikalische Chemie*, 1974, **78**, 58–67.

(99) R. Griessen, N. Strohfeldt and H. Giessen, *Nature Materials*, 2015, **15**, 1–7.

(100) A. Ulvestad, M. J. Welland, S. S. E. Collins, R. Harder, E. Maxey, J. Wingert, A. Singer, S. Hy, P. Mulvaney, P. Zapol and O. G. Shpyrko, *Nature Communications*, 2015, **6**, 10092.

(101) R. Lässer and K. .-.-H. Klatt, *Physical Review B*, 1983, **28**, 748–758.

(102) B. J. Heuser and J. S. King, *Journal of Alloys and Compounds*, 1997, **261**, 225–230.

(103) B. J. Heuser and J. S. King, *Metallurgical and Materials Transactions A*, 1998, **29A**, 1593.

(104) G. J. Thomas and J. M. Mintz, *Journal of Nuclear Materials*, 1983, **116**, 336–338.

(105) S. A. H. Zaidi, *Journal of Catalysis*, 1981, **263**, 255–263.

(106) S. B. Ziemecki, *Reactivity of Solids*, 1986, **1**, 195–198.

(107) S. B. Ziemecki, G. A. Jones and D. G. Swartzfager, *Journal of Less-Common Metals*, 1987, **131**, 157–162.

(108) D. Teschner, J. Borsodi, A. Wootsch, Z. Révay, M. Hävecker, A. Knop-Gericke, S. D. Jackson and R. Schlögl, *Science*, May 2008, **320**, 86.

(109) M. Gurrath, T. Kuretzky, H. P. Boehm, L. B. Okhlopkova and A. S. Lisitsyn, *Carbon*, 2000, **38**, 1241–1255.

(110) C. W. A. Chan, Y. Xie, N. Cailuo, K. M. K. Yu, J. Cookson, P. Bishop and S. C. Tsang, *Chemical Communications*, July 2011, **47**, 7971–3.

(111) C. W. A. Chan, K. Y. Tam, J. Cookson, P. Bishop and S. C. Tsang, *Catalysis Science & Technology*, 2011, **1**, 1584–1592.

(112) J. Häglund, A. F. Guillermet, G. Grimvall and M. Körling, *Physical Review B*, 1993, **48**, 11685–11691.

(113) M. Beck, M. Ellner and E. Mittemeijer, *Acta Materialia*, Apr. 2001, **49**, 985–993.

(114) M. Beck, M. Ellner and E. Mittemeijer, *Zeitschrift für Kristallographie*, 2001, **216**, 591–594.

(115) H. Husemann and H. Brodowsky, *Zeitschrift für Naturforschung A*, 1968, **23A**, 1693.

(116) R. Mehlmann, H. Husemann and H. Brodowsky, *Berichte der Bunsen-Gesellschaft für physikalische Chemie*, 1973, **77**, 36–41.

(117) H. Brodowsky and H.-J. Schaller, *Berichte der Bunsen-Gesellschaft für physikalische Chemie*, 1976, **80**, 656–661.

(118) R. Burch and F. A. Lewis, *Transactions of the Faraday Society*, 1970, **66**, 727–735.

(119) M. Krawczyk, *Applied Surface Science*, 1998, **135**, 209–217.

(120) J.-Y. Wang, Y.-Y. Kang, H. Yang and W.-B. Cai, *The Journal of Physical Chemistry C*, May 2009, **113**, 8366–8372.

(121) M. Beck, Dr. rer. nat. Dissertation, Institut für Metallkunde der Universität Stuttgart, Max-Planck-Institut für Metallforschung Stuttgart, 2001.

(122) C. W. A. Chan, A. H. Mahadi, M. M.-J. Li, E. C. Corbos, C. Tang, G. Jones, W. C. H. Kuo, J. Cookson, C. M. Brown, P. T. Bishop and S. C. E. Tsang, *Nature Communications*, Jan. 2014, **5**, 5787.

(123) B. Yang, R. Burch, C. Hardacre, G. Headdock and P. Hu, *Journal of Catalysis*, Sept. 2013, **305**, 264–276.

(124) J. Gegner, G. Hörz and R. Kirchheim, *Journal of Materials Science*, Sept. 2008, **44**, 2198–2205.

(125) C. S. Gopinath, K. Thirunavukkarasu and S. Nagarajan, *Chemistry, An Asian Journal*, Jan. 2009, **4**, 74–80.

(126) S. Nagarajan, K. Thirunavukkarasu and C. S. Gopinath, *The Journal of Physical Chemistry C*, Apr. 2009, **113**, 7385–7397.

(127) G. M. Veith, A. R. Lupini, L. Baggetto, J. F. Browning, J. K. Keum, A. Villa, L. Prati, A. B. Papandrew, G. A. Goenaga, D. R. Mullins, S. E. Bullock and N. J. Dudney, *Chemistry of Materials*, 2013, **25**, 4936–4945.

(128) P. Rochana, K. Lee and J. Wilcox, *Journal of Physical Chemistry C*, 2014, **118**, 4238–4249.

(129) N. N. Greenwood and A. Earnshaw, *Chemistry of the Elements*, Butterworth-Heinemann, Oxford, Second Edi, 1997.

(130) J. Sangster and A. Pelton, *Journal of Phase Equilibria*, 1992, **13**, 63–66.

(131) O. Loebich, Jr. and C. J. Raub, *Journal of the Less-Common Metals*, 1976, **55**, 67–76.

(132) R. A. Howald, *Calphad*, 1990, **14**, 1–9.

(133) T. Nohira, K. Amezawa and Y. Ito, *Journal of Applied Electrochemistry*, 1995, **25**, 48–53.

(134) J. R. Kitchin, J. K. Nørskov, M. A. Barteau and J. G. Chen, *Physical Review Letters*, 2004, **93**, 4–7.

(135) A. Ruban, H. Skriver and J. Nørskov, *Physical Review B*, 1999, **59**, 15990–16000.

(136) A. Ruban, B. Hammer, P. Stoltze, H. L. Skriver and J. K. Nørskov, *Journal of Molecular Catalysis A: Chemical*, 1997, **115**, 421–429.

(137) M. Armbrüster, M. Behrens, F. Cinquini, K. Föttinger, Y. Grin, A. Haghofer, B. Klötzer, A. Knop-Gericke, H. Lorenz, A. Ota, S. Penner, J. Prinz, C. Rameshan, Z. Révay, D. Rosenthal, G. Rupprechter, P. Sautet, R. Schlögl, L. Shao, L. Szentmiklósi, D. Teschner, D. Torres, R. Wagner, R. Widmer and G. Wowsnick, *ChemCatChem*, Aug. 2012, **4**, 1048–1063.

2

Analytical Techniques

Contents

2.1 Introduction

It is vitally important to have reliable information as to the nature of a particular catalyst in order to understand its role in a chemical reaction. With this in mind, a large range of analytical techniques have been developed to aid our understanding of the catalyst's surface (i.e. the top 0.5 to 3 nm, equivalent to approximately 2 - 10 atomic layers) and bulk properties. For materials on the nanoscale the distinction between bulk and surface technique blurs.[1]

Advances in nanoscale characterisation mean that it is no longer the "black art" which it once was, but an ideal scenario would give perfect information about the catalyst under reaction conditions.[2] This, however, is very rarely possible due to

general inaccessibility of working catalysts and the reactants themselves interfering with the analysis. A variety of techniques are therefore required in order have a good understanding of the catalyst's properties prior to use in a reaction. These include thermal analysis, spectroscopy, microscopy, a range of radiation techniques and probe molecules. This information can then be used to improve existing catalysts, or rationally design new catalysts.[3]

2.2 Powder X-ray Diffraction

Powder X-ray diffraction (XRD) is a very common technique in nanoparticle characterisation. As a non-destructive (at least for standard laboratory instruments) bulk technique, the interactions between the X-rays and the material's atoms provides structural information for crystalline materials.

Commonly, for a laboratory instrument, incident X-rays are generated by firing high energy electrons, generated by a tungsten source, at a copper target. This high energy bombardment ejects core electrons, typically from the K shell. As a Cu electron from a higher shell transitions into the electron holes, a photon is emitted as an X-ray. The X-rays enter a collimator and a monochromator to filter the light into a semi-coherent beam of X-rays with one or two wavelengths. For a lab-based copper-source instrument the two common wavelengths are Cu $K_{\alpha 1}$ ($\lambda = 1.540\,56\,\text{Å}$) and Cu $K_{\alpha 2}$ ($\lambda = 1.544\,39\,\text{Å}$) which are caused by the $2p_{\frac{3}{2}}$ and the $2p_{\frac{1}{2}}$ to 1s transitions respectively.

Synchrotron X-rays are created by the curved movement of charged particles through a magnetic field. They were initially noticed by Elder *et al.* in 1947 who recognised the radiation generated as something characterised by Iwanenko and Pomeranchuk three years earlier.[4,5] The advantages of a synchrotron X-ray source are that the incident X-rays are much brighter than their Cu-source counterparts, allowing for better characterisation of very thin (nm scale) films and for use in

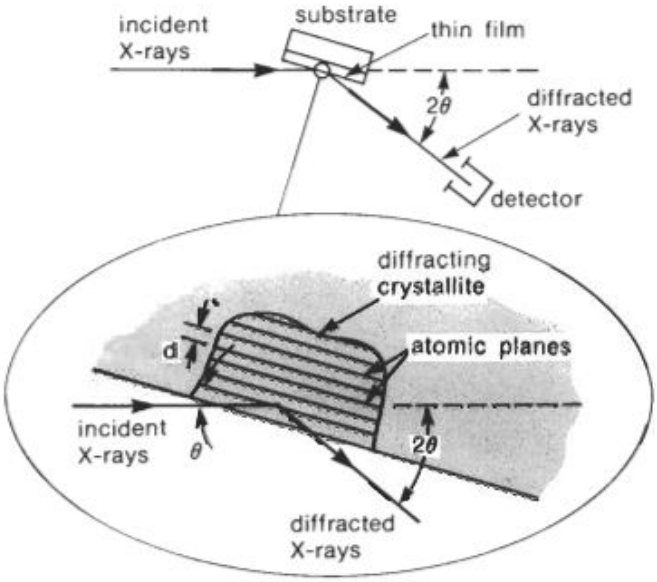

Figure 2.1: Schematic of a typical XRD experiment demonstrating the diffraction of X-rays by a crystalline material. Reproduced from reference.[6]

more exotic X-ray techniques discussed later in this chapter.[6]

A big advantage to XRD is that it is a non-destructive technique that lends itself very well to *in-situ* work as it is not dependent on a particular environment to function. Samples can be heated (or cooled) under a flow of a number of different gases (air, nitrogen, helium, hydrogen to name a few) in order to observe how a material changes under these conditions.

Figure 2.1 details how, should the material subjected to the X-ray beam consist of ordered crystalline phases, the X-rays diffract by the elastic scattering caused by atoms in the material. Constructive interference occurs at angles characteristic to the material and the interlayer spacings, d, can be calculated through Bragg's Law (Equation 2.1).

$$n\lambda = 2d_{hkl} \sin\theta \tag{2.1}$$

Where n is an integer representing the order of diffraction, λ is the wavelength of incident X-ray radiation (i.e. 1.540 56 Å for a typical lab source), d is the interplanar

spacing and θ is the diffraction (Bragg) angle. The characteristic diffraction pattern can be used to identify a material. Studying subtle changes in the diffraction pattern of heterogeneous catalysts, for example small shifts in peak positions due to expansion or contraction of the lattice, is a particularly good tool for tracking interstitial doping or alloy formation.

The interplanar spacing, d_{hkl}, can be used to calculate the lattice parameter, a, of a crystalline material by relating the spacing to the Miller indices, h, k and l of a particular Bragg plane. For cubic materials, such as palladium, Equation 2.2 can be used.

$$\frac{1}{d_{hkl}^2} = \frac{h^2 + k^2 + l^2}{a^2} \tag{2.2}$$

The particle size of samples with a long range order can be estimated through the Scherrer equation (Equation 2.3), however for nanoparticles with much less long range order, the diffraction peaks become increasingly broad, limiting the accuracy of the equation. It is important to correct for instrument broadening otherwise the value for the particle size will be inaccurate. Another consideration is that the Scherrer equation tends to underestimate particle sizes, due to different crystallographic domains appearing as separate particles. Often a direct observation method, such as transmission electron microscopy, is more useful.

$$L = \frac{K\lambda}{\beta \cos\theta} \tag{2.3}$$

L being the average crystallite size, K is a shape factor, normally set to unity, λ is the X-ray wavelength, β is the full width half maximum (FWHM) of a peak and θ is the Bragg angle.

2.3 Pair Distribution Function

A more exotic use for synchrotron X-rays than XRD is Pair Distribution Function (PDF). Other high-energy radiations such as hot neutrons can be used for this technique. PDF is a powerful tool in characterising amorphous phases in nanoscale materials, as well as other systems such as liquid-liquid and liquid-solid phase boundaries. Although the theory behind PDF has been known since the 1920's, it took until fairly recently that the facilities capable of providing the quality high-energy electrons or neutrons necessary came into being.[7,8]

As mentioned in Section 2.2, Bragg's Law (Equation 2.1) can be used to analyse how atoms are arranged in crystalline materials. These crystals are randomly oriented within the powder which leads to diffraction rings with a specific lattice vector, Q (Equation 2.4).

$$Q = \frac{4\pi \sin\theta}{\lambda} \tag{2.4}$$

If a crystal is not perfectly periodic, it can give rise to diffuse scattering of X-rays. Diffuse scattering is present in XRD but is normally considered part of the background. The diffuse scattering in non-crystalline samples possessing no long-range order. Using an X-ray source is undesirable for large values of Q because the X-ray form factor greatly reduces the scattering intensity. A neutron source is preferable where the study of large values of Q is required as the form factor is not an issue.[8]

The rationale behind PDF can be described by the Debye equation for diffraction (Equation 2.5), which states that an isotropic approximation can be made for a randomly oriented system. The observed scattering intesity (I_N) is linked to the sum of all pairs of atoms r_{ij} within the material.[9,10]

$$I_N(Q) \propto S(Q) = 1 + \frac{1}{N} \sum_{i,i \neq j}^{N} f_i f_j \frac{\sin(Qr_{ij})}{Qr_{ij}} \tag{2.5}$$

Where f_i is the atomic form factor and $S(Q)$ the structure factor. θ is the diffraction angle, and λ the incident radiation wavelength.

As PDF is considered a total scattering technique where both Bragg and diffuse scattering are considered, the function $g(r)$ (Equation 2.6) is the probability of finding two atoms a distance r apart. This allows PDF to contain information about the average, longer range structure and the local structural disorder of a material.

$$g(r) - 1 = \frac{1}{2\pi^2 r\rho} \int_0^\infty Q[S(Q) - 1] \sin(Qr) dr \tag{2.6}$$

Unlike other techniques, such as extended X-ray adsorption fine structure (EXAFS), which can be considered a partial PDF, PDF does not need to be centred on any particular atom, therefore giving a description of the local ordering around any given atom.[11] PDF gives the probability of finding two atoms at a distance x apart. This is a particular advantage for systems where there is no long range order and conventional X-ray techniques would struggle.

2.4 X-ray Photoelectron Spectroscopy

X-ray photoelectron spectroscopy (XPS) is a surface sensitive technique capable of probing the top 2 to 5 nm of a material's surface. XPS is able to identify the surface composition of a material, including the electronic states of the elements present. It is often used in tandem with XRD which provides information about the bulk characteristics of a system. The origins of XPS lie in the photoelectric effect discovered by Einstein in 1905.[12] However, it took until the 1960's and the work of Kai Siegbahn for the analytical properties of this effect to be known.[13]

The X-rays used for XPS are generated in a similar way as those used in XRD,

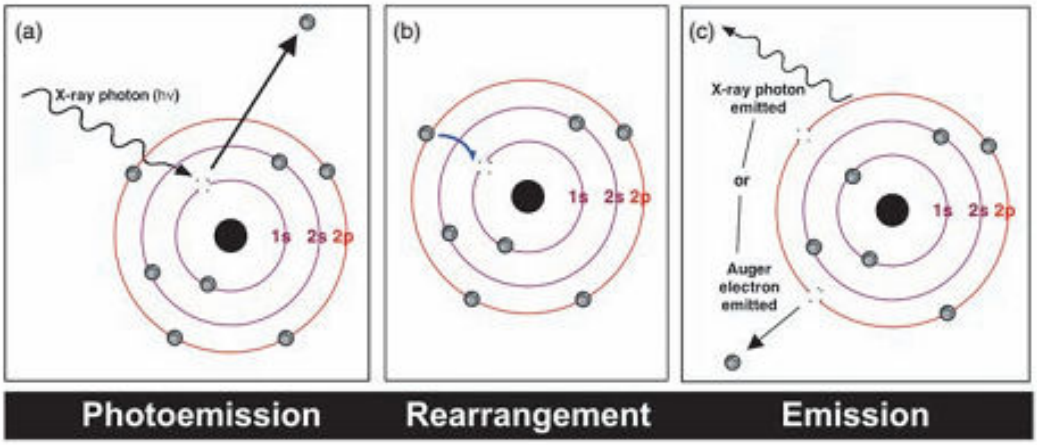

Figure 2.2: : Schematic of how an atom behaves under bombardment with X-ray photons. a) the incident X-ray is absorbed prompting the ejection of a core electron. This leads to b) where the electrons within the atom rearrange, with a higher energy electron dropping down to fill the vacancy and c) the emission of a photon (or an Auger electron) resulting from this transition. Reproduced from reference.[1]

however an Al or Mg target is used resulting in much lower energy (soft) X-rays (1486.3 eV for an aluminium source compared to 8027.8 eV for copper). Figure 2.2 shows the basis behind XPS. The emitted X-ray photon, caused by the dropping of a higher shell electron into the core, has a characteristic energy, as defined by Equation 2.7. Incidentally, XPS is only a surface sensitive technique as the emitted electron from deeper inside the particle lacks the energy to escape the material due to inelastic collisions with other atoms within the material.

$$E_k = h\nu - E_b - \phi \tag{2.7}$$

Where E_k is the energy of the photoemitted electron, h Planck's constant, ν the frequency of the incident radiation, E_b the binding energy of the emitted electron and ϕ the work function of the spectrometer.

As E_b is unique for each element it can be used to quantify the elemental surface composition of a material. High resolution scans give information about the shifts in E_b, which indicate the oxidation state of the element in question. For example the change between Ce^{3+} and Ce^{4+}, and Pd and Pd^{2+} are readily detectable.[14,15]

When a non-conducting sample (which lacks a method of being earthed within the spectrometer) undergoes XPS investigation, large shifts in binding energy can be seen due to the build-up of positive charge in the sample. In these cases it is common to reference a peak, often the C 1s peak if available, to the known position of that peak in the absence of the charging effects.[6]

It is thought that interstitial modification of palladium by a light atom will have an influence on the metal's electron density at the Fermi level. This change, if sufficiently large, will be noticeable through XPS due to a change in palladium peak positions. The light element will be much harder to detect due to very poor response factors in XPS, boron being several orders of magnitude less responsive than palladium as an example.[1]

2.5 Thermogravimetric Analysis

Thermogravimetric analysis (TGA) is a technique designed to track the weight change of a sample as it is heated or cooled in a controlled manner. Changes in sample mass can be attributed to redox processes, material decomposition or solvent evaporation. With more advanced instruments, differential scanning calorimetry (DSC) can be used in conjunction with TGA to see how the heat-flow in the system changes at a particular moment in time. A negative heat-flow (i.e. more energy is required to continue the heating ramp or maintain the current temperature than would be expected) is typical of solvent evaporation while a positive heat-flow can be ascribed to a chemical reaction happening within the sample. Samples can be analysed in inert or reactive atmospheres and it is important to maintain a standard heating rate and initial sample mass when analysing a range of samples. Variations in these can cause changes in peak position or resolution and the observed decomposition temperatures. Typical experiments use very little sample (1 to 50 mg) but the major downside to TGA is the destructive nature of the analysis.[3]

2.6 Solid State Nuclear Magnetic Resonance

Nuclear magnetic resonance (NMR) was first described by I. I. Rabi in 1938 where it was seen that magnetic nuclei (e.g. ^{1}H, ^{13}C, ^{31}P), when placed in a magnetic field, resonate when radio frequency (RF) of the correct energy was applied to the nucleus.[16]

This field was rapidly expanded from the molecular beams initially studied to include solid systems. One of the major problems of materials in the solid state is line broadening due to the various interactions between the dipole and quadrupole moments of the nuclei, the electric field gradient at the nucleus and the anisotropy of differing levels of electronic shielding at different sites in the structure. This is not seen in fluids as the atomic motion of a sample is quicker than the interaction frequency.[17,18]

Magic angle spinning (MAS) is the most common method for enhancing resolution for solid state experiments. The sample is spun at the magic angle of ~54.74° ($\cos\theta_m{}^2 = \frac{1}{3}$) which removes the anisotropic effects, leaving only the isotropic effects that would be seen in solution. This is because the second order Legendre polynomial equals zero at this angle. Figure 2.3 shows this schematically.

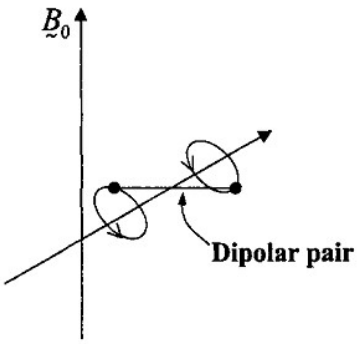

Figure 2.3: Schematic re-orientation of a dipole at the magic angle whilst spinning in a magnetic field. Reproduced from reference.[17]

The disadvantage of this is that spinning side bands can form at integer values

of the spinning frequency, ν. Spinning the sample at different frequencies can confirm that the features observed are indeed side bands and give some information about the anisotropy of the system.[17]

Another consideration when dealing with metal systems is Knight shift.[19] This is due to electrons delocalising in conductors giving rise to shifts that are much greater than typical chemical shifts. A common method to avoid this effect but still give surface information is to use a spacer molecule such as formate, where the nuclei of interest interact indirectly with the conductor.[20] The effects of the Knight shift on interstitially inserted atoms into Pd is much less well studied, though for palladium hydride a concentration dependence was observed in the degree of Knight shift present.[21]

Information can be gathered about the magnetic environment of a spin system through how such a system relaxes following a perturbing radio frequency pulse. In a simple system macroscopic z magnetisation recovers according to Equation 2.8.

$$M_\tau - M_\infty = (M_\infty - M_0)e^{-\frac{\tau}{T_1}} \tag{2.8}$$

Where M_τ is the macroscopic z magnetisation at a time τ after a perturbing radio-frequency (RF) pulse. T_1 is the nuclear spin-lattice relaxation time and it is calculated using a three-parameter fit of the experimental information (Equation 2.9).

$$M_\tau = a - be^{-\frac{\tau}{T_1}} \tag{2.9}$$

However, spin-lattice relaxation in solids often deviates from the usual exponential relaxation seen due to, for example, paramagnetic impurities in a sample. Another possibility is the nucleus existing in two or more environments which cause identical nuclei to relax at substantially different rates.[22]

A simpler, but less accurate way to calculate the relaxation time is to use a stretched exponential to fit the data (Equation 2.10).

$$I = I_0(1 - e^{-\frac{\tau}{T_1}^x}) \qquad 0.6 \leqslant x \leqslant 1 \tag{2.10}$$

The stretched exponential can be used if there is a distribution of different relaxation rates, as determined by the fitting factor x. This factor needs a value between 0.6 and 1 to be deemed valid. Outside of this range it is unlikely that the non-exponential relaxation is due to paramagnetic impurities within the sample.[22]

A multi-exponential fit (Equation 2.11) is more complex and fits each relaxation component individually, though with increasing numbers of relaxation environments the fitting process becomes exponentially more difficult.[23]

$$I = I_0(1 - e^{-\frac{\tau}{T_1}}) + I_0'(1 - e^{-\frac{\tau}{T_1'}}) \tag{2.11}$$

Should a single exponential fit not work (i.e. there is more than one component), both the stretched exponential and multi exponential equations can be used to fit the non-exponential T_1 relaxation. However, for some systems, the stretched exponential is insufficient to properly describe the system and if this should this be the case, then the more complex multi-exponential fit is required to accurately represent the system.

Saturation-relaxation experiments can be used to determine different environments for the nucleus under investigation. Therefore it is possible to differentiate atoms on the surface of a catalyst, and those within the metal lattice. Interstitial atoms are likely to relax in conjunction with the host metal. This will lead to a very fast relaxation of the interstitial atom allowing it to be differentiated from surface species.[24]

2.7 Electron Microscopy

As optical microscopes are limited to a resolution of 1 µm by virtue of the wavelength of visible light, electron microscopy uses a beam of electrons to allow Ångström

level resolution. This magnification, up to 1 000 000 times, is sufficient to directly observe a heterogeneous catalyst's particle dispersion, particle morphology, and even detailed structural information with atomic resolution of a particle surface.[6]

The electron microscope itself (Figure 2.4) consists of an illumination source and an electromagnetic lens system with an electron gun and a series of magnetic lenses to focus and make the electrons coherent. The beam strikes perpendicular to the sample holder and the electrons, after passing through the sample, are refocussed onto an imaging plate.[6]

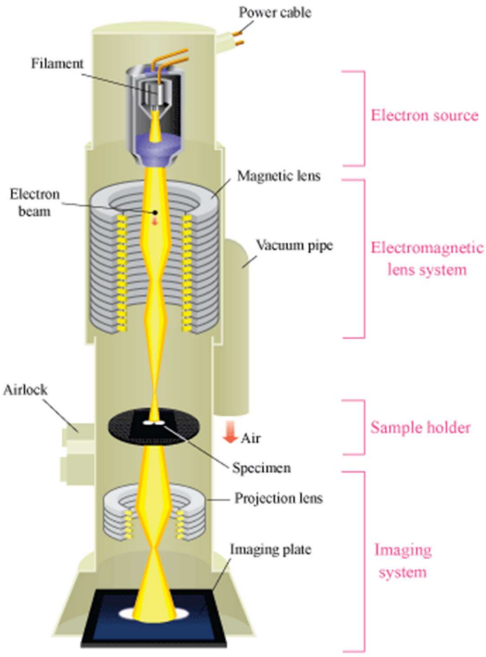

Figure 2.4: A schematic of a typical electron microscope. Reproduced from reference[25].

When the electron beam interacts with the sample, a wide variety of processes occur revealing a wealth of information about a sample, summarised in Figure 2.5. The techniques used in this work are electron energy loss spectroscopy (EELS), transmission electron microscopy (TEM) and scanning transmission electron microscopy (STEM).

In a typical TEM experiment the transmitted electrons are those which have passed through the sample allowing a two-dimensional projection of the sample

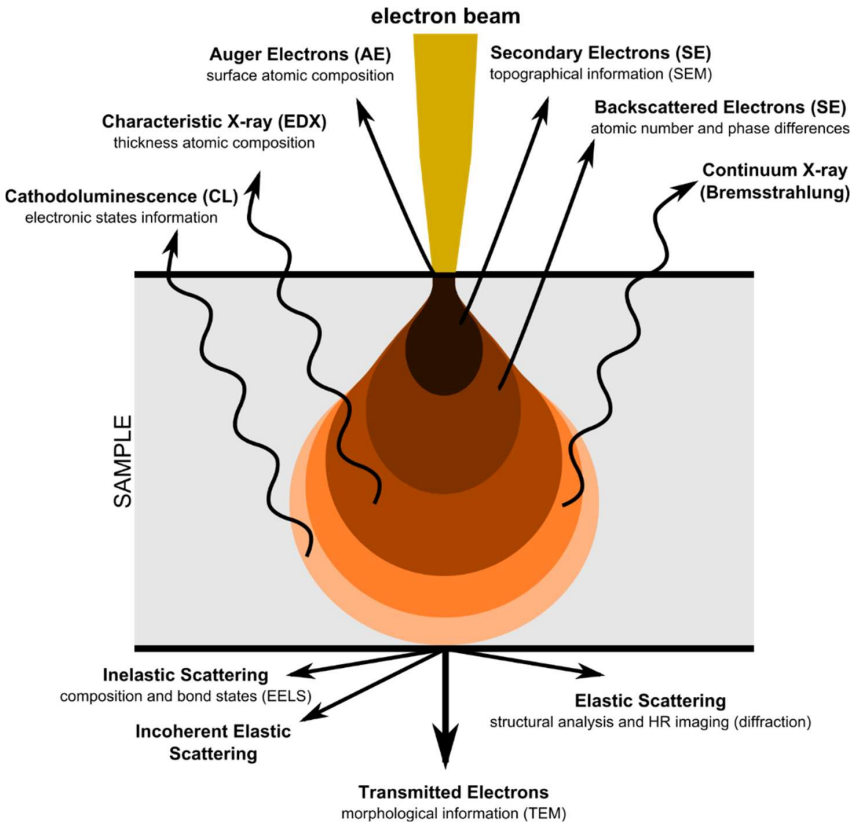

Figure 2.5: A summary of what techniques can be used and what information can be gained from an electron microscope. Reproduced from reference.[26]

to be imaged. Standard TEM looks at the annular bright-field (ABF) where only transmitted electrons are used to form the final image. In ABF, the heavier the nuclei examined (or the thicker the sample), the darker the image against at a bright background. Annular dark-field (ADF) imaging uses diffracted electrons to construct the image. Here the background is dark with light areas appearing due to coherent scattering from the nuclei. Depending on the detector distance from the centre of the transmitted electrons (i.e. the ABF region), different information can be gleaned about the structural features of a sample. Low-angle ADF (LAADF) gives more information about strain in a particle compared to medium- and high-angle ADF (MAADF and HAADF) which gives more information about particle density.

STEM images are a combination of information from the classic TEM image and information from scanning electron microscopy (SEM). SEM detects the secondary

emission of electrons from a sample which can be used to reconstruct an image. As STEM is a combination of these two techniques, images of greater clarity and resolution can be taken.

2.8 Electron Energy Loss Spectroscopy

The final microscope technique used in this thesis is electron energy loss spectroscopy (EELS). This is a characterisation technique which can determine the positions of certain elements within a sample, and even the oxidation state of the elements. This allows a two-dimensional map of the elemental composition of the sample to be built.[27]

EELS utilises the kinetic energy of the scattered electrons (Figure 2.5) to determine the elements present in a sample through inelastic scattering of the electron beam. The amount of energy lost by the beam depends on which of the sample electrons the beam interacts with. For example, a loosely held outer N shell palladium electron will result in a lower energy loss than a tightly held inner K shell electron. It can therefore be sensitive to the oxidation state present in a material. As the energy loss is a primary interaction with the incident electrons, unlike energy dispersive X-ray spectroscopy (EDX) which relies upon secondary X-ray emission, more information is retained in EELS in comparison to EDX.

Recent advances in STEM-EELS allows for near-atomic resolution and in conjunction with other spectroscopic techniques can give huge amounts of information about a sample.[28] Work by Jones *et al.* allows the recombination of several rapidly taken STEM images at different orientations into a single image with excellent resolution.[29] This will allow an interstitially modified palladium nanoparticle to be viewed in great detail, with the potential to see a light dopant within the lattice (although this is considered unlikely due to the huge mass-difference between palladium and the dopant).

2.9 Gas Chromatography

Gas chromatography (GC) is an analytical technique that separates the various gases and volatile compounds that exist in a sample. After a sample is injected into a heated chamber to ensure total vaporisation of all components, an inert carrier gas (typically N_2 or He) transports the sample across a stationary phase. The separation then occurs as the individual components within the sample interact with the column differently as they pass through. All molecules of a certain analyte within the sample will have the same retention time, hence they will elute from the column at the same time. Columns are usually packed with a stationary phase with a high weight molecular polymer coating.

It is necessary to optimise the retention time of the various components in a sample being analysed so that each component elutes at separate, discrete points. This can be done by initially selecting a column known to have a good separation for the compounds under investigation. Changing the length of a column can also help to separate compounds with similar retention times, at the cost of slower analysis times and peak broadening. Using temperature ramps is a useful method to drive off compounds with particularly long retention times.

There are two common detectors used to analyse elutants. The first of which, a flame ionising detector (FID), will work on any sample capable of ionising in a hydrogen/air flame. FID's have excellent detection limits in the picogram scale which make them a useful candidate for quantification of the products. One major issue with FID's, especially in work that involves hydrogen, is that H_2 is undetectable. Fortunately, a thermal conductivity detector (TCD), which operates by comparing the thermal conductivity of eluted gases referenced to the carrier gas, can detect any component except the carrier gas itself. It is not uncommon to find GC instruments equipped with an FID and two TCD's with different carrier gases (He and N_2) to ensure the proper detection of all components.

2.10 Temperature Programmed Reduction

First developed by J. W. Jenkins as a variant on temperature programmed desorption (TPD), temperature programmed reduction (TPR) is used to observe how a material behaves under reducing conditions.[30,31] Prior to the TPR experiment, the sample is pre-treated under a flow of inert gas to remove moisture or any other surface contaminant. The TPR experiment itself consists of a continuous flow of H_2 over the sample as the temperature is steadily increased. The data is relative to the H_2 response at a TCD detector where (under normal polarity) any consumption of H_2 will lead to a negative peak, and any released H_2 a positive peak.

In this thesis, TPR was used to observe the β-hydride desorption peak from palladium catalysts. This peak, which is observed at around 80 °C (exact position depends on particle size, support used etc.) is characteristic of interstitial hydrogen leaving the palladium lattice.[32] If this peak is smaller than anticipated it is a useful indicator that some (or all) of the interstitial sites of the metal are blocked.[33]

2.11 Superconducting Quantum Interference Device

A superconducting quantum interference device (SQUID) is a very sensitive magnetometer able to measure magnetic fields as low as 5 aT.[34] SQUID's are based upon superconducting loops known as Josephson junctions, named after B. D. Josephson who predicted the relationship between two superconducting loops separated by a thin insulating contact.[35,36] Quantum tunnelling allows the insulating bridge to be crossed, indeed the bridge can be tunnelled even without the application of a voltage. A sample in this environment will affect the magnetic flux of the system and will alter the interaction between the superconducting loops. SQUID's are very sensitive to the presence of these magnetic fields.[37]

Common uses for SQUID's include detecting the magnetism in biological systems, for example an arrangement of SQUID's can be used to study neural activity (magnetoencephalography).[38] The use of SQUID in this work is studying the paramagnetism of palladium samples. In a paramagnetic sample, as an external magnetic field is applied the observed magnetic moment of the sample should increase as the electrons with the sample align.

It has been observed that when an element (in this case hydrogen) has entered the palladium lattice, the paramagnetic character of the sample is lost as the interstitial hydrogen opposes the induced magnetic field.[39]

2.12 Pulse Chemisorption

As typical heterogeneously catalysed chemical reactions occur on the surface of a metal catalyst, quantification of the metal surface area, and hence the number of active sites in a sample, is required to understand the efficiency of a catalyst system. For example, it is common to report turn over frequency (TOF) in terms of atoms converted per active site per unit time. It is therefore necessary to use a gas that binds to the metal catalyst but not the support, such as CO or H_2.[6] Chemisorption analysis also allows inferences to be drawn/made about other properties of the system, such as mean particle size and metal dispersion. It is important to note that a number of assumptions are required to deduce this information (e.g. the shape of the particle, the support interaction and how clean the surface is) so a direct measurement technique, such as TEM, is preferable.[40]

In a typical pulse chemisorption experiment, the sample surface is 'cleaned' and fully reduced by heating under hydrogen and subsequently in an inert gas such as He, the conditions of which will depend on the material being investigated. Subsequently a known volume of the adsorbate gas is injected into an inert gas stream. The TCD peak areas (Figure 2.6) are analysed to see how much gas has

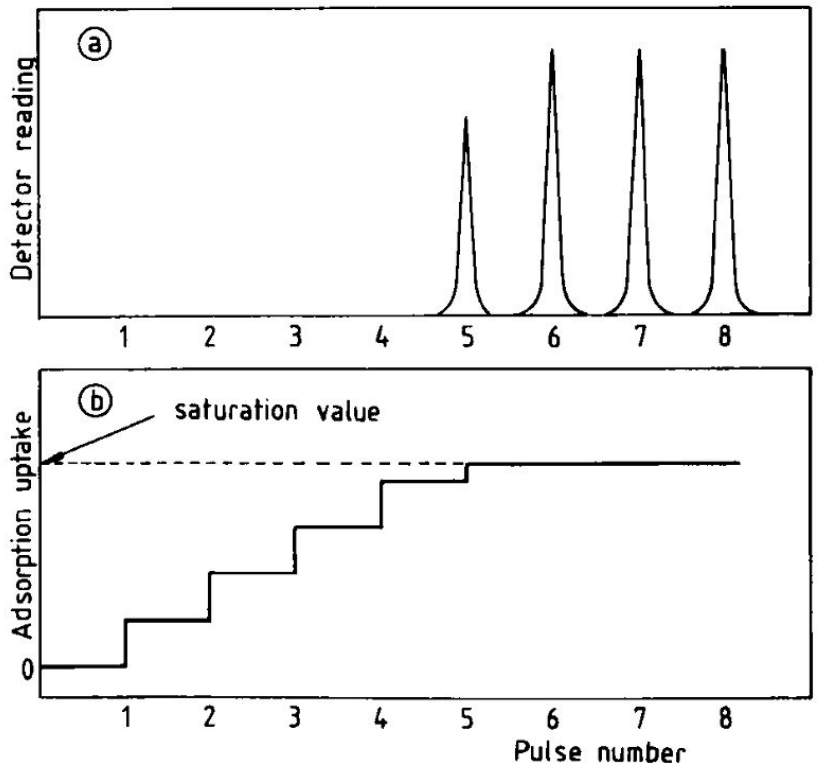

Figure 2.6: a) A typical pulse chemisorption profile, the peaks increasing as the metal surface becomes more saturated with the adsorbate gas. b) the volume of adsorbed gas in relation to the saturation level. Reproduced from reference.[41]

adsorbed and when the surface is saturated. This is quantified by assuming that the fully saturated peak corresponds to the known amount of injected gas.

These peak areas are used to determine metal surface area with respect to sample and metal mass, metal dispersion and metal particle size using Equations 2.12-2.15 respectively.

$$A_s = N_A n_{ads} F_s a_m 10^{-23} \tag{2.12}$$

$$A_m = A_s \frac{100}{X_m} \tag{2.13}$$

$$D = \frac{10 n_{ads} F_s M_m}{X_m} \tag{2.14}$$

$$d = \frac{S_f 10^3}{A_m \rho_m} \tag{2.15}$$

Where A_s and A_m are metal surface area per gram of sample or metal respectively, N_A is Avogadro's number, n_{ads} the moles of adsorbed gas, a_m the cross-sectional metal area, F_s is a stoichiometric factor relating moles of adsorbed gas to moles of metal, X_m the percentage metal loading, D metal dispersion, M_m the metal atomic mass, S_f a dimensionless shape factor, ρ_m the metal density and d, the average particle size.[41]

For the CO chemisorption on Pd samples as conducted in this work, the F_s is 1, a_m is $0.0787\,\mathrm{nm}^2$ and ρ_m is $12.023\,\mathrm{g\,cm}^{-3}$.

2.13 References

(1) *Surface Analysis – The Principal Techniques*, ed. J. C. Vickerman and I. S. Gilmore, John Wiley and Sons, Ltd, Chichester, 2nd edn., 2009.

(2) R. Jin, *Nanotechnology Reviews*, 2012, **1**, 31–56.

(3) *Handbook of Analytical Techniques*, ed. H. Günzler and A. Williams, Wiley-VCH Verlag GmbH & Co. KGaA, Weinheim, Germany, 2nd edn., 2002.

(4) F. R. Elder, A. M. Gurewitsch, R. V. Langmuir and H. C. Pollock, *Physical Review*, 1947, **71**, 829–830.

(5) D. Iwanenko and I. Pomeranchuk, *Physical Review*, 1944, **65**, 343.

(6) *Encyclopedia of Materials Characterization*, ed. C. R. Brundle, C. A. Evans, Jr. and S. Wilson, Butterworth-Heinemann, Greenwich, Connecticut, 1992.

(7) F. Zernike and J. A. Prins, *Zeitschrift für Physik*, 1927, **41**, 184.

(8) S. J. L. Billinge, *Zeitschrift für Kristallographie*, 2004, **219**, 117–121.

(9) P. Debye, *Annalen der Physik*, 1915, **351**, 809–823.

(10) H. E. Fischer, A. C. Barnes and P. S. Salmon, *Reports on Progress in Physics*, 2006, **69**, 233.

(11) A. Fernandez-Martinez, G. J. Cuello, J. E. Daniels and L. Charlet, *Macla*, 2008, **9**, 99–100.

(12) A. Einstein, *Annalen der Physik*, 1905, **322**, 132–148.

(13) K. Siegbahn and K. Edvarson, *Nuclear Physics*, 1956, **1**, 137–159.

(14) S. C. DeCaluwe, M. E. Grass, C. Zhang, F. El Gabaly, H. Bluhm, Z. Liu, G. S. Jackson, A. H. Mcdaniel, K. F. Mccarty, R. L. Farrow, M. A. Linne, Z. Hussain and B. W. Eichhorn, *Journal of Physical Chemistry C*, 2010, **114**, 19853–19861.

(15) K. Jiang, J. Chang, H. Wang, S. Brimaud, W. Xing, R. J. Behm and W.-b. Cai, *Applied Materials and Interfaces*, 2016, **8**, 7133–7138.

(16) I. Rabi, J. Zacharias, S. Millman and P. Kusch, *Physical Review*, 1938, **53**, 318.

(17) K. J. D. MacKenzie and M. E. Smith, *Multinuclear Solid-State NMR of Inorganic Materials*, ed. R. W. Cahn, Pergamon, Kidlington, 1st edn., 2002.

(18) D. D. Laws, H.-M. L. Bitter and A. Jerschow, *Angewandte Chemie International Edition*, 2002, **41**, 3096.

(19) W. D. Knight, *Physical Review*, 1949, **76**, 1259–1260.

(20) K. Tedsree, C. W. A. Chan, S. Jones, Q. Cuan, W.-K. Li, X.-Q. Gong and S. C. E. Tsang, *Science*, 2011, **332**, 224–228.

(21) P. Brill and J. Voitländer, *Berichte der Bunsengesellschaft für physikalische Chemie*, 1973, **77**, 1097–1103.

(22) A. Narayanan, S. J. Hartman and A. D. Bain, *Journal of Magnetic Resonance, Series A*, 1995, **112**, 58–65.

(23) E. Yeramian and P. Claverie, *Nature*, 1987, **326**, 169–174.

(24) J. van der Klink and H. Brom, *Progress in Nuclear Magnetic Resonance Spectroscopy*, 2000, **36**, 89–201.

(25) C. Eley, D.Phil. Thesis, University of Oxford, 2014.

(26) Claudionico˜commonswiki, *Electron Interaction with Matter*, 2016.

(27) *Transmission Electron Energy Loss Spectrometry in Materials Science and the EELS Atlas*, ed. C. C. Ahn, Wiley-VCH Verlag GmbH & Co. KGaA, Weinheim, 2nd edn., 2004.

(28) J. M. Thomas, R. K. Leary, A. S. Eggeman and P. A. Midgley, *Chemical Physics Letters*, 2015, **631-632**, 103–113.

(29) L. Jones, H. Yang, T. J. Pennycook, M. S. J. Marshall, S. Van Aert, N. D. Browning, M. R. Castell and P. D. Nellist, *Advanced Structural and Chemical Imaging*, 2015, **1**, 8.

(30) S. D. Robertson, B. D. McNicol, J. H. De Baas, S. C. Kloet and J. W. Jenkins, *Journal of Catalysis*, 1975, **37**, 424–431.

(31) S. E. Golunski, *Platinum Metals Review*, 2008, **52**, 249–250.

(32) V. H. Sandoval and C. E. Gigola, *Applied Catalysis A: General*, 1996, **148**, 81–96.

(33) C. W. A. Chan, Y. Xie, N. Cailuo, K. M. K. Yu, J. Cookson, P. Bishop and S. C. Tsang, *Chemical Communications*, July 2011, **47**, 7971–3.

(34) D. Drung, C. Aßmann, J. Beyer, A. Kirste, M. Peters, F. Ruede and T. Schurig, *IEEE Transactions on Applied Superconductivity*, 2007, **17**, 699–704.

(35) B. D. Josephson, *Physics Letters*, 1962, **1**, 251–253.

(36) B. D. Josephson, *Reviews of Modern Physics*, 1974, **46**, 251–254.

(37) A. I. Golovashkin, A. L. Karuzskii, V. M. Mishachev, A. A. Orlikovsky, V. V. Privezentsev and A. M. Tshovrebov, *Russian Microelectronics*, 2006, **35**, 354–358.

(38) R. Kleiner, D. Koelle, F. Ludwig and J. Clarke, *Proceedings of the IEEE*, 2004, **92**, 1534–1548.

(39) A. G. Lipson, B. J. Heuser, C. H. Castano and A. Celik-Aktas, *Physics Letters, Section A: General, Atomic and Solid State Physics*, 2005, **339**, 414–423.

(40) L. Torrente-Murciano, *Journal of Nanoparticle Research*, 2016, **18**, 87.

(41) *Spectroscopic Characterization of Heterogeneous Catalysts Part B: Chemisorption of Probe Molecules*, ed. J. L. G. Fierro, Elsevier, Amsterdam, 1990.

3

Experimental Methods

Contents

3.1 Palladium on Carbon

All catalysts used within this work are based upon Pd/C synthesised *via* the following methods.

3.1.1 Solvent Based Approach

5 % weight palladium supported on carbon was synthesised using Chan *et al.*'s method.[1] In a typical synthesis, Vulcan ® XC72R carbon (1.9 g) was stirred with butan-1-ol (100 mL) before the dropwise addition of $Pd(NO_3)_2$ solution (15.11 % Pd assay, 0.66 mL, 2.283 mmol). After stirring at room temperature overnight the solution was filtered and washed thoroughly with deionised water and ethanol. A clear, yellow tinged filtrate indicates that the palladium has anchored to the support. The catalyst was dried overnight at 80 °C before it was reduced in a Carbolite tubular furnace in a 1:1 hydrogen:nitrogen atmosphere, with a flow rate of 60 mL min^{-1}. The furnace was ramped to 500 °C at a rate of 5 °C min^{-1} and held for 1 hour, before cooling to room temperature. Once at room temperature the atmosphere was switched to 100 % nitrogen for 15 minutes to flush the system of hydrogen, before the furnace was opened to air.

3.1.2 Grinding Approach

Loading palladium onto carbon *via* physically mixing the palladium acetate with the support followed by heating above the $Pd(OAc)_2$ thermal decomposition temperature

(205 °C) under an inert atmosphere was inspired by Lin *et al.*'s work with metal salts and carbon nanotubes.[2,3]

A 5 % weight loading of palladium on Vulcan ® XC72R carbon was achieved by grinding the carbon (190 mg) with $Pd(OAc)_2$ (21.28 mg) until the powder appeared homogeneous (approximately 5 minutes) in an agate pestle and mortar. The resultant black powder was transferred to an inert nitrogen atmosphere and heated to 250 °C for 1 hour before cooling to room temperature.

A 50 % weight loading of palladium on Vulcan ® XC72R carbon was achieved by grinding the carbon (100 mg) with $Pd(OAc)_2$ (212 mg) until the powder appeared homogeneous, which was approximately 5 minutes constant grinding, in an agate pestle and mortar. The resultant black powder was similarly transferred to an inert nitrogen atmosphere and heated to 250 °C for 1 hour before cooling to room temperature.

3.2 Palladium Interstitial Boron

Palladium interstitially doped with boron was the subject of Markus Beck's thesis.[4] His method required the use of arc melting to dope boron into palladium foils. Unfortunately, this approach means that the interesting materials Beck investigated have no industrial application. This method was improved upon by Chan *et al.* with a much simpler process that allowed the doping of palladium nanoparticles, and began the investigation of these interstitially doped materials for catalytic application.[1]

3.2.1 *via* Borane

Chan's method is a solvent based approach.[1] Initially, 5 % by weight Pd/C catalyst (typically 100 mg), under an inert atmosphere of nitrogen is suspended in tetrahydrofuran (THF) (3 mL) before a 1.0 M borane tetrahydrofuran complex (BH_3-THF) in THF (2 mL) was added dropwise. There is a large excess of boron used given

the tendency of the activated carbon support to take up the boron and prevent its incorporation into the palladium lattice. The suspension was heated to 40 °C and the solvent is slowly evaporated under nitrogen. Once all the solvent was evaporated the powder was heated to 200 °C under N_2 for one hour to drive the boron into the palladium lattice. After cooling to room temperature the resultant black powder was washed with water (250 mL) and ethanol (250 mL) and left to dry overnight.

3.2.2 *via* Sodium Borohydride

A solvent free approach was devised whereby 5 % by weight Pd/C catalyst (typically 100 mg) was ground with an agate pestle and mortar with sodium borohydride ($NaBH_4$) (20 mg, 0.63 mmol) – a 5:1 B:Pd molar ratio – in a glovebox with a nitrogen atmosphere. The inert atmosphere was necessary when using Pd samples of size <10 nm as the hydrogen released from the decomposition of $NaBH_4$ is catalytically recombined with atmospheric oxygen over the Pd catalyst. This is an exothermic reaction and can ignite the carbon support. The grinding usually took approximately 5 minutes at which point the mixture appeared homogeneous. The resultant black powder was then heated to 200 °C under nitrogen for one hour to decompose the sodium borohydride and drive the boron into the lattice. The resulting black powder was cooled to room temperature, washed with water (250 mL) and ethanol (250 mL) and left to dry overnight.

One Pot Approach

Similar to the above solvent free approach, this involved the grinding together of the carbon support (0.95 g) with palladium acetate (0.212 g) and sodium borohydride (0.200 g) using an agate pestle and mortar. An advantage here was that this approach doesn't require the use of a glove box. The grinding usually took approximately 5 minutes at which point the mixture appeared homogeneous. This black powder

was then heated to 200 °C under nitrogen for one hour to decompose the palladium acetate and sodium borohydride, and drive the boron into the newly formed Pd lattice. After the resultant black powder was cooled to room temperature, washed with water (250 mL) and ethanol (250 mL) and left to dry overnight.

3.2.3 *via* Sodium Triacetoxyborohydride

Another solvent free approach was investigated whereby 5 % by weight Pd/C catalyst (typically 100 mg) was ground with an agate pestle and mortar with sodium triacetoxyborohydride ($NaBH(OAc)_3$) (414 mg, 2.0 mmol), until the mixture appeared homogeneous. This usually took approximately 5 minutes. Again there is a risk of fire if done in air, so this procedure was done in a nitrogen glovebox. This black powder was then heated to 200 °C for one hour under nitrogen to decompose the $NaBH(OAc)_3$ and drive the boron into the lattice. The resultant black powder was cooled to room temperature, washed with water (250 mL) and ethanol (250 mL) and left to dry overnight.

3.3 Palladium Interstitial Lithium

3.3.1 *via* *n*-Butyllithium

5 % by weight Pd/C catalyst (typically 100 mg), under an inert atmosphere of nitrogen was suspended in tetrahydrofuran (THF) (3 mL) before 2.5 M *n*-butyllithium solution in hexanes (2 mL) was added dropwise. Similar to the solvent based boron synthesis, a large excess of lithium is used because the activated carbon support can take up some of the lithium and prevent its incorporation into the Pd lattice. The suspension was heated to 50 °C to slowly evaporate the solvent under nitrogen. Once all the solvent had evaporated the powder was heated to 250 °C for two hours to drive the lithium into the palladium lattice. After cooling

to room temperature the resultant black powder was washed with water (250 mL) and ethanol (250 mL) and left to dry overnight.

3.3.2 *via* Lithium Acetate

A solvent free approach was devised whereby 5 % by weight Pd/C catalyst (typically 100 mg) was ground with an agate pestle and mortar with lithium acetate (CH_3COOLi) (73 mg). In contrast to the boron grinding approaches, there is no fire risk, so the physical mixing can be done in air. The grinding usually took approximately 5 minutes after which the mixture appeared homogeneous. This black powder was then heated to 250 °C under nitrogen for two hours to decompose the lithium acetate and drive the lithium into the lattice. The resultant black powder was cooled to room temperature, washed with water (250 mL) and ethanol (250 mL) and left to dry overnight.

3.4 Analysis

3.4.1 X-ray Diffraction

Powder XRD

Powder XRD was performed on a PANalytical X'Pert Pro Diffractometer, equipped with a generator set to 40 kW and 40 mA and a copper source emitting Cu_{K_α} radiation of wavelength $\lambda = 1.5406$ Å. Samples were prepared by placing the powder onto either a glass or aluminium slide and pressing it flat with a spatula. Profiles were measured from $2\theta = 5$ - 90°.

In-situ XRD

In-situ powder XRD was performed using a Siemens D5000 X-ray Diffractometer, equipped with a Bruker D5005 X-ray generator set to 40 kW and 40 mA and a Cu

source. The instrument is fitted with a parallel beam Göbel mirror with an Aton Paar HTK 1200 high temperature attachment. Samples were heated from room temperature to 500 °C either in air or under a helium atmosphere. Profiles were taken at regular intervals, scanning from 2θ = 10 - 90°.

3.4.2 X-ray Photoelectron Spectroscopy

XPS analysis was conducted on a VG Escalab XPS Spectrometer with an aluminium source of energy = 1486.3 eV under ultra-high vacuum. Samples were prepared by pressing a sticky carbon tab, attached to a sample holder, into the fine powder. Initially four wide scans from 0 to 1200 eV (dwell time = 0.1 s, step interval = 1 eV, pass energy = 50 eV) were done to identify regions of interest. These regions of interest were then sequentially scanned 15 times (dwell time = 0.4 s, step interval = 0.1 eV, pass energy = 20 eV). The C 1s peak was referenced to 284.5 eV for charge correction.[5]

3.4.3 Thermogravimetric Analysis

Thermogravimetric analysis (TGA) was conducted using a TA Instrument TGA Q50. Approximately 5 to 10 mg of sample was placed on a tared platinum pan before the sample was accurately weighed. The samples were held isothermally under a flow of gas (either air or N_2). The sample was then ramped to 800 °C with ramp rate of 10 °C min^{-1}.

3.4.4 Transmission Electron Microscopy

Transmission electron microscopy (TEM) images were taken with a JEOL 2010 microscope at the Begbroke Science Park. TEM samples were prepared by sonicating the sample (1 mg) in ethanol (10 mL) for 30 minutes to fully disperse the particles. The suspension was then dropped onto a holey carbon coated Cu grid and dried

under a stream of nitrogen. The instrument was operated at various times by Dr Hanif Mahadi, Dr Amy Kolpin, Dr Simon Jones, Dr Simon Fairclough, Bin Yu and Elizabeth Raine (all University of Oxford).

3.4.5 Scanning TEM - Electron Energy Loss Spectroscopy

Scanning TEM (STEM) and Electron Energy Loss Spectroscopy (EELS) were conducted by Lewys Jones of the Department of Materials, University of Oxford on a JEOL ARM200CF instrument. For all measurements the camera length was 12 cm with a probe angle of 22 mrad.

STEM images were taken simultaneously in three modes, annular bright-field (ABF) (detector inner/outer angles: 12.25 mrad/19.94 mrad), low-angle annular dark-field (LAADF) (detector inner/outer angles: 22.85 mrad/36.00 mrad), and medium-angle annular dark-field (MAADF) (detector inner/outer angles: 50.39 mrad/242.03 mrad). For each mode a number of images were taken in rapid succession then combined using the Smart Align algorithm by Lewys Jones *et al.* to give the final image.[6]

EELS was done taken by scanning a 200 keV electron beam over the sample with the data acquisition time taking between 1 and 10 minutes depending on particle size and desired detail in the resultant compositional information.

3.4.6 Chemisorption

CO pulse chemisorption measurements were carried out using Quantachrome Instruments ChemBET Pulsar TPR/TPD Automated Chemisorption Analyser. Approximately 20 mg of sample was packed between two quartz wool plugs in a quartz glass reactor tube. Helium was used as a carrier gas with a flow rate of 20 mL min^{-1} and 100 % CO was used as a titrant gas. Samples were pre-treated under H_2 for 1 hour at various temperatures and then cooled under inert gas before

the CO pulse chemisorption measurements were taken. The CO was pulsed 7 times with a pulse volume of 72 µL. The detector current was set to 150 mA with an attenuation of 1.

3.4.7 Temperature Programmed Reduction

Temperature programmed reduction (TPR) measurements were performed using a Quantachrome ChemBET Pulsar TPR/TPD Automated Chemisorption Analyser. Typically, 20 mg of sample was held between two quartz wool plugs inside the reactor tube. Each sample was pre-treated by heating in He (150 °C for a Pd/C system) for one hour to remove moisture and other adsorbed gasses. 5 % H_2 in Ar with a flow rate of 100 mL min^{-1} was used as the reducing gas. Samples were ramped from 40 to 500 °C at a rate of 5 °C min^{-1}. The detector was set to 150 mA with an attenuation of 1.

3.4.8 Solid State Nuclear Magnetic Resonance

Solid state nuclear magnetic resonance (NMR) was done at Warwick University in collaboration with Tom Hooper and Dr John Hanna. All samples were diluted with three parts NaCl as the catalysts are a conductive material.

One Pulse Experiments

^{7}Li NMR experiments were, for the 5 % loaded Pd-$^{\text{interstitial}}$Li/C, conducted by loading a 1.3 mm Bruker probe with the material. The NMR was conducted in a 100 MHz (2.35 T) Bruker Avance III HD spectrometer with magic angle spinning of 60 kHz and a 1.29 ms pulse time. For 50 % Pd/C, the sample was packed into a 2.5 mm Bruker probe. The NMR was conducted using a 600 MHz (14.1 T) Bruker Avance II+ instrument, with magic angle spinning at 30 kHz, 1.50 ms pulse time and a flip angle of 45°.

^{11}B NMR experiments were, for both 5 % and 50 % Pd-$^{\text{interstitial}}$B/C, conducted by loading a 4 mm Varian probe with the material. The NMR was conducted using a 600 MHz (14.1 T) Varian instrument with magic angle spinning at 12 kHz.

Saturation-Relaxation Experiments

For this study, the 50 % weight loaded Pd/C, Pd-$^{\text{interstitial}}$B/C and Pd-$^{\text{interstitial}}$Li/C samples were used. For ^{7}Li NMR, a 2.5 mm Bruker probe was loaded with the material. The spectrometer used was a 500 MHz (11.7 T) Bruker Avance III, with magic angle spinning at 30 kHz, a 2.25 ms pulse time and a flip angle of 90°.

For ^{11}B NMR, a 4 mm Varian probe was loaded with the catalyst. The experiment was conducted using a 600 MHz (14.1 T MHz Bruker Avance II+ instrument, with magic angle spinning at 12 kHz, 2.95 ms pulse time and a flip angle of 90°.

3.4.9 X-ray Pair Distribution Function

X-ray pair distribution function (PDF) experiments were conducted at the I15 Beamline at the Diamond Light Source, in collaboration with Professor Chui Tang and Tsz Lo. A small amount of sample was loaded into a kapton capillary sample holder. The sample to detector distance was ~240.72 mm, the X-ray energy was 76.0 keV (i.e. a wavelength of $\lambda = 0.163\,14$ Å), and the total scattering X-ray data were collected using the Rapid Acquisition Pair Distribution Function method.[7] Data were collected over the range $0.5 < Q < 50\,\text{Å}^{-1}$ and corrected for background, Compton and multiple scattering, and beam attenuation by the sample holder interference by using the GudrunX package, which itself was used to normalise the one-dimensional data to the normalised structure factor ($S(Q)$), and hence $d(r)$, rather than modelling the data itself.[8] $S(Q)$ was converted to the PDF in the form of the $d(r)$ function as laid out by Keen.[9] In addition, the DAWN software was used to convert the two-dimensional diffraction image into the integrated one-dimensional

pattern.[10] The refinements of $d(r)$ were performed using PDFgui, in which scale factor, lattice parameters, dampening and broadening factors were set to be refined, with the fit range set to be from 1.5 to 10 Å.[11]

3.5 Catalytic Testing

The catalytic tests undertaken on the catalysts synthesised above are as follows:

3.5.1 High Pressure Liquid Phase Hydrogenations

High pressure hydrogenations were undertaken in a High Pressure HEL Chemscan reactor at the Johnson Matthey Technology Centre, Sonning Common. The apparatus is equipped with 8 parallel stainless steel Hastelloy reactors, with independent pressure, temperature and stirring control. Each reactor is equipped with a Teflon stirrer and glass vial insert. Prior to the reaction each vessel was leak tested by pressurising the vessels to 6.6 bar using nitrogen and tracking the reactor pressure over time.

Before beginning the reaction, the reactor cells were purged three times with N_2, twice with the reactive gas, and heated to the desired reaction temperature. The reaction progress was monitored through hydrogen uptake curves (i.e. the amount of H_2 required to maintain the pressure within the reaction vessel). Each substrate (Table 3.1, Figure 3.1) was hydrogenated with 3 bar hydrogen, at a temperature of 30 °C and a stirring rate of 1200 rpm. Each reaction consisted of a 5 mL of a 0.5 M solution (2.5 mmol) of the substrate in either DCM or ethanol and was hydrogenated using 2.50 µmol palladium (except *ortho*-chloronitrobenzene in ethanol where 3.80 µmol of Pd was used). For the samples analysed by GC (3-hexyn-1-ol, diphenylacetylene, phenylacetylene and *ortho*-chloronitrobenzene, all in ethanol), 1,4-dioxane (0.5 M, 2.5 mmol) was used as an internal standard. After the reaction the H_2 atmosphere was vented and then the systems purged once with N_2.

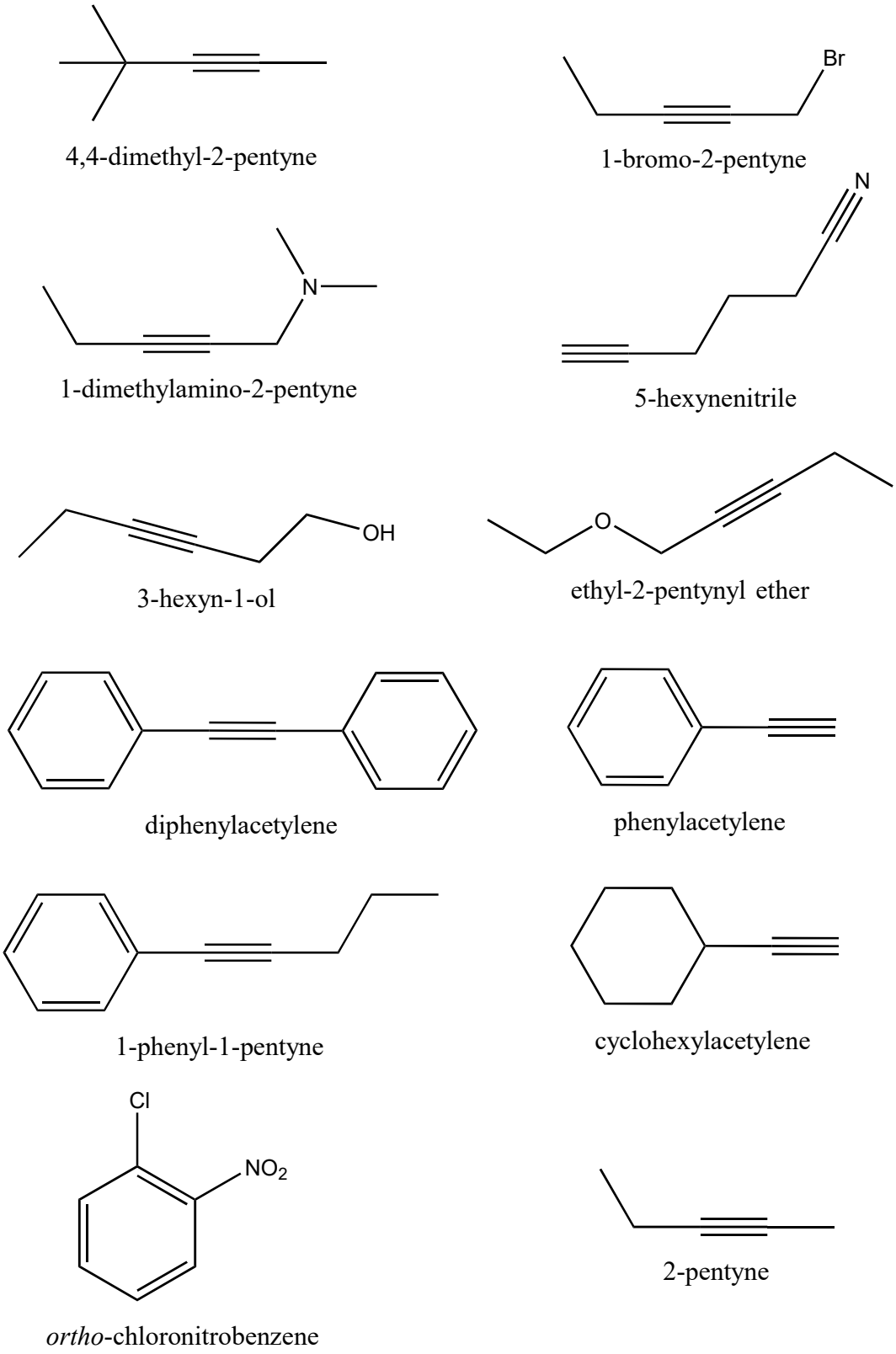

Figure 3.1: Graphical summary of the substrates tested at the Johnson Matthey Technology Centre, Sonning Common.

Table 3.1: A summary of the substrates hydrogenated at the Johnson Matthey Technology Centre in Sonning Common.

Substrate	Abbrev.	Mass (g)	Vol. (mL)	Conc. (M)
1-Phenyl-1-pentyne	PHP	0.3606	5	0.5
2-Pentyne	PNT	0.1703	5	0.5
5-Hexynenitrile	HNN	0.2453	5	0.5
1-Dimethylamino-2-pentyne	DAP	0.2780	5	0.5
4,4-Dimethyl-2-pentyne	DMP	0.2404	5	0.5
Cyclohexylacetylene	CHA	0.2705	5	0.5
1-Bromo-2-pentyne	BRP	0.3675	5	0.5
Ethyl-2-pentynyl ether	EPE	0.2804	5	0.5
3-Hexyn-1-ol	HYL	0.2454	5	0.5
ortho-Chloronitrobenzene	CNB	0.3939	5	0.5
Phenylacetylene	PA	0.2554	5	0.5
Diphenylacetylene	DPA	0.4456	5	0.5

3.5.2 Ambient Pressure 3-Hexyn-1-ol Hydrogenation

Ambient pressure 3-hexyn-1-ol hydrogenations were undertaken in a 250 mL three-neck round-bottom flask equipped with a Teflon coated stirrer, paraffin oil bubbler and two rubber septa. One septum had a stainless steel needle for bubbling hydrogen through and the other was used for withdrawing samples. The reaction was stirred at 750 rpm, hydrogen bubbled at 30 mL min^{-1} and the temperature was set to 30 °C.

3.5.3 Acetylene Hydrogenation

In-House Testing

Initial acetylene hydrogenation experiments were carried out in a custom fixed-bed continuous flow reactor. The catalyst was accurately weighed out and placed between two plugs of quartz wool into a Pyrex glass tube of 4 mm internal diameter. The total flow rate of the carrier and reaction gases (N_2, H_2, and 10 % C_2H_2 in N_2) was fixed at 50 mL min^{-1} with acetylene comprising 5 % of the resulting gas mix.

For temperature varied reactions the reagent gas ratios were fixed to either

1:1 or 1:2 C_2H_2:H_2 (i.e. a 5 %:5 % or 5 %:10 % ratio of total gas flow) and 75 mg catalyst was used. Five measurements were obtained for each temperature point (room temperature, 50 °C, 100 °C, 150 °C, and another at 50 °C after cooling the system down). Longer term catalytic studies at a fixed temperature of 100 °C were also undertaken using 5 mg catalyst for incomplete conversion, the sample was loaded identically as above, and a 1:1 reaction gas ratio was used. Measurements were taken every 10 minutes for 500 minutes.

Product gas analysis was conducted on a Perkin Elmer Arnel AutoSystem XL gas chromatograph equipped with a HayeSep T type column. Helium and nitrogen were used as carrier gases. The TCD was used to analyse the resultant gases, with the Turbochrom Navigator software used to integrate the chromatograms. Peak areas were corrected against the response factor for each product.[12]

Industrial Testing

Samples of 5 % Pd/C, Pd-$^{\text{interstitial}}$B/C and Pd-$^{\text{interstitial}}$Li/C were sent to the Johnson Matthey Technology Centre, Sonning Common and tested under industrial conditions by Dr Pilar Gomez-Jimenez of Johnson Matthey. Samples were tested both as the original powder (10 mg per test) and as pellets of size 250 to 300 µm (30 mg). The gas mixture was 97.9 % C_2H_4, 1.0 % C_2H_2, 1.1 % H_2 and the flow rate was fixed at either 150 or 200 mL min^{-1} depending upon the experiment performed. The reaction temperature was slowly increased as the experiment progressed. The resultant gasses were analysed by GC. Both the final acetylene and ethane concentrations were studied as these markers are the most commercially important. Direct comparisons between the catalysts were taken at the same acetylene conversion point, not at the same temperature as this leads to a clearer understanding of the reaction in progress.

3.5.4 1-Pentyne Vapour Phase Hydrogenation

The reagent solution comprised 1-pentyne (6.81 g, 1 M) reagent, plus 2-methylpentane (8.62 g, 1 M) as an internal standard, dissolved in *n*-hexane (100 mL). The catalyst sample was weighed into a quartz tube (360 mm long by 6 mm outer diameter by 4 mm inner diameter) and held in the central position by means of quartz wool plugs either side. Typically, 5 to 20 mg of catalyst was used depending on the loading.

The 1-pentyne reagent solution was added through a heated vaporiser at a flow rate of 0.06 mL min^{-1}. All of the gas transport tubing from the point of injection of the reagent solution to the GC sampling valve was heated to 120 °C to ensure no condensation of reagent or hydrogenation product compounds. The transport gas was pure He for the non-reaction conditions and 40 % H_2/He for the hydrogenation conditions. The flow rate was set at 200 mL min^{-1} on an air calibrated mass flow controller which equates to an actual flow of 279 mL min^{-1} of pure He and 247 mL min^{-1} of 40 % H_2/He. Due to the downstream restrictions of the narrow tubing and GC sampling valve, the backpressure on the system causes it to operate at around 6.0 psi gauge pressure with the furnace at room temperature and this rises to around 6.5 psi at 250 °C. The variations are due to the individual catalyst sample packing, particle sizes and weight used. This measurement came from a single check and the system back pressure is not routinely monitored.

The test proceeds by allowing the pure He and 1-pentyne reagent to come to equilibrium over the catalyst in the furnace at room temperature and then sampling by GC which operates on a 15 minute cycle time per sample. Once several reproducible non-hydrogenation samples had been acquired the transport gas was switched to the 40 % H_2/He hydrogenation gas. After flushing for 5 minutes the furnace was started on its ramp cycle of room temperature to 250 °C at 2 °C min^{-1}. The furnace was cooled under He at the end of the test with He flowing over the catalyst sample.

3.6 Computational Details

3.6.1 DFT Calculations

Density functional theory (DFT) calculations were carried out using the grid based projector augmented wave (GPAW) code.[13,14] Bulk lattice parameters for fcc-Pd ($a_0 = 3.99\,\text{Å}$) were obtained using the planewave cut-off of 1100 eV, and Monkhorst-Pack k-point mesh of $8 \times 8 \times 8$ for palladium.[15] PAW potentials were used to describe the core electrons and the electron-electron interaction was described using the revised Perdew-Burke-Ernzerhof (RPBE) functional.[16] Surface slabs were subsequently prepared for Pd(111) consisting of 4 atomic layers with a vacuum gap of 12 Å, with bottom two layers frozen in the bulk positions and the two top most layers allowed to relax. The calculations for the surfaces were run using finite difference mode with GPAW, using a grid spacing of 0.18 Å (which is equivalent to a planewave cutoff of 1100 eV). All calculations used a Fermi-Dirac smearing of 0.1 eV. Structural relaxations were converged to $0.05\,\text{eV}\,\text{Å}^2$. Two subsets of structural models were examined for the two dopant elements (B, Li), the initial structure having the dopant on the surface, and the initial structure having the dopant subsurface at a notional coverage of 0.25 monolayers. Electronic structure analysis was carried out using the Atomic Simulation Environment in conjunction with topological analysis using the Bader charge analysis code.[17,18]

Molecule calculations were conducted through the MoCalc2012 graphical user interface.[19] Initial geometry optimisations were conducted in Stewart's MOPAC 2016 software set to use the restricted Hartree-Fock (RHF) wavefunction and the PM7 Hamiltonian.[20–23] Molecular energy calculations utilised Granovsky's Firefly QC package, which is partially based upon the GAMESS(US) source code.[24,25] The optimised molecules had their dipoles estimated *ab initio* using the RHF wavefunction, the 6-31G* basis set, and the BYLP DFT type.[22,26–28]

3.6.2 Kinetic Modelling

Ambient pressure 3-hexyn-1-ol hydrogenation reaction profiles were fit using a Langmuir-Hinshelwood kinetic model. A least squares method was used to determine unknown rate constants with the overall rate constant k treated as a constant for the purpose of the optimisation calculation *via* the SIMPLEX method.[29]

The root mean square error (RMSE) cost function, f, (Equation 3.1) was defined as the difference between the experimental and fitted reaction data profiles.

$$f = \sqrt{\frac{1}{n - nk} \sum_{i=1}^{ns} \frac{([P_i]_{exp} - [P_i]_{cal})^2}{[P_i]_{exp}}} \tag{3.1}$$

Where n is the number of experimental data points, nk the number of rate constants to be fit and ns the number of species. All calculations were performed in Matlab (R2015b) with initial rate constants based upon the unmodified palladium catalyst and compared to other systems tested under these conditions.[1]

3.7 References

(1) C. W. A. Chan, A. H. Mahadi, M. M.-J. Li, E. C. Corbos, C. Tang, G. Jones, W. C. H. Kuo, J. Cookson, C. M. Brown, P. T. Bishop and S. C. E. Tsang, *Nature Communications*, Jan. 2014, **5**, 5787.

(2) P. K. Gallagher and M. E. Gross, *Journal of Thermal Analysis*, 1986, **31**, 1231–1241.

(3) Y. Lin, K. A. Watson, M. J. Fallbach, S. Ghose, J. G. Smith, D. M. Delozier, W. Cao, R. E. Crooks and J. W. Connell, *ACS Nano*, Apr. 2009, **3**, 871–884.

(4) M. Beck, Dr. rer. nat. Dissertation, Institut für Metallkunde der Universität Stuttgart, Max-Planck-Institut für Metallforschung Stuttgart, 2001.

(5) R. J. J. Jansen and H. van Bekkum, *Carbon*, 1995, **33**, 1021–1027.

(6) L. Jones, H. Yang, T. J. Pennycook, M. S. J. Marshall, S. Van Aert, N. D. Browning, M. R. Castell and P. D. Nellist, *Advanced Structural and Chemical Imaging*, 2015, **1**, 8.

(7) P. J. Chupas, X. Qiu, J. C. Hanson, P. L. Lee, C. P. Grey and S. J. L. Billinge, *Journal of Applied Crystallography*, 2003, **36**, 1342–1347.

(8) A. K. Soper and E. R. Barney, *Journal of Applied Crystallography*, 2011, **44**, 714–726.

(9) D. A. Keen, *Journal of Applied Crystallography*, 2001, **34**, 172–177.

(10) M. Basham, J. Filik, M. T. Wharmby, P. C. Y. Chang, B. El Kassaby, M. Gerring, J. Aishima, K. Levik, B. C. A. Pulford, I. Sikharulidze, D. Sneddon, M. Webber, S. S. Dhesi, F. Maccherozzi, O. Svensson, S. Brockhauser, G. Náray and A. W. Ashton, *Journal of Synchrotron Radiation*, 2015, **22**, 853–858.

(11) C. L. Farrow, P. Juhas, J. W. Liu, D. Bryndin, E. S. Božin, J. Bloch, T. Proffen and S. J. L. Billinge, *Journal of physics. Condensed matter : an Institute of Physics journal*, 2007, **19**, 335219.

(12) Y. Guan, L. Zhou, D. Zhu and W. Jiang, *Journal of Chromatography A*, July 1992, **604**, 233–241.

(13) J. J. Mortensen, L. B. Hansen and K. W. Jacobsen, *Physical Review B - Condensed Matter and Materials Physics*, 2005, **71**, 1–11.

(14) J. Enkovaara, C. Rostgaard, J. J. Mortensen, J. Chen, M. Dułak, L. Ferrighi, J. Gavnholt, C. Glinsvad, V. Haikola, H. A. Hansen, H. H. Kristoffersen, M. Kuisma, A. H. Larsen, L. Lehtovaara, M. Ljungberg, O. Lopez-Acevedo, P. G. Moses, J. Ojanen, T. Olsen, V. Petzold, N. A. Romero, J. Stausholm-Møller, M. Strange, G. A. Tritsaris, M. Vanin, M. Walter, B. Hammer, H. Häkkinen, G. K. H. Madsen, R. M. Nieminen, J. K. Nørskov, M. Puska, T. T. Rantala, J. Schiøtz, K. S. Thygesen and K. W. Jacobsen, *Journal of Physics: Condensed Matter*, 2010, **22**, 253202.

(15) J. D. Pack and H. J. Monkhorst, *Physical Review B*, 1977, **16**, 1748–1749.

(16) B. Hammer, L. Hansen and J. Nørskov, *Physical Review B*, 1999, **59**, 7413–7421.

(17) S. R. Bahn and K. W. Jacobsen, *Computing in Science and Engineering*, 2002, **4**, 56–66.

(18) G. Henkelman, A. Arnaldsson and H. Jónsson, *Computational Materials Science*, 2006, **36**, 354–360.

(19) D. B. Depizzol, M. H. M. Paiva, T. O. D. Santos and A. C. Gaudio, *Journal of Computational Chemistry*, 2005, **26**, 142–144.

(20) J. J. P. Stewart, *Journal of Computer-Aided Molecular Design*, 1990, **4**, 1–103.

(21) J. J. P. Stewart, *Journal of Molecular Modeling*, 2013, **19**, 1–32.

(22) S. Hammes-Schiffer and H. C. Andersen, *Journal of Chemical Physics*, 1993, **99**, 1901.

(23) J. J. P. Stewart, *MOPAC 2016, version 16.076W*, http://OpenMOPAC.net, 2016.

(24) A. A. Granovsky, *Firefly, version 8.1.1*, http://classic.chem.msu.su/gran/firefly/index.html, 2016.

(25) M. W. Schmidt, K. K. Baldridge, J. A. Boatz, S. T. Elbert, M. S. Gordon, J. H. Jensen, S. Koseki, N. Matsunaga, K. A. Nguyen, S. Su, T. L. Windus, M. Dupuis and J. A. Montgomery, *Journal of Computational Chemistry*, 1993, **14**, 1347–1363.

(26) V. A. Rassolov, J. A. Pople, M. A. Ratner and T. L. Windus, *Journal of Chemical Physics*, 1998, **109**, 1223–1229.

(27) A. D. Becke, *Physical Review A*, 1988, **38**, 3098–3100.

(28) C. Lee, W. Yang and R. G. Parr, *Physical Review B*, 1988, **37**, 785–789.

(29) J. A. Nelder and R. Mead, *The Computer Journal*, 1965, **7**, 308–313.

4

Design of Interstitially Doped Palladium Nanocatalysts

Contents

4.1 Background

The synthesis of catalysts is an expensive business and catalyst companies must try to reduce this cost. This can be achieved through reducing the precious metal content of the catalyst through using non-precious metals to replace, or partially

replace, current precious metal catalysts. For example, this can be achieved by using copper with palladium in hydrogenation reactions, or by directly reducing the amount of precious metal used in a particular catalyst ("thrifting").[1,2] Similarly, costs can be reduced by making the production process more energy efficient which requires the elimination or simplification of steps in the manufacture of catalysts. From an industrial perspective there is little point in making a catalyst that is 3 % more selective if the cost of manufacture and operation is 10 % greater than the current leading catalyst.

The insertion of small light elements into the palladium lattice as a technique for catalyst modification is an area that has been explored in greater detail in recent years. Extensive research has focussed on palladium as a potential hydrogen storage material as Pd can absorb huge amounts (up to 900 times its own volume) of H_2. Hence, Pd is often referred to as a "sponge" for H_2 absorption.[3] Palladium is able to absorb this volume by dissociating hydrogen on the metal surface which then penetrates the lattice and resides in the octahedral sites of the palladium (Pd-$^{\text{interstitial}}$H). Indeed it is this ability of Pd metal to readily dissociate hydrogen and form the interstitial phase that makes it such a potent hydrogenation catalyst, with atomic hydrogen readily able to migrate out of the lattice or dissociate on the surface to hydrogenate a bond. Preventing Pd from forming the interstitial Pd−H phase can thus decrease hydrogenation activity and will increase selectivity to the partial hydrogenation products.[4]

Initial observations by Teschner *et al.* of the formation of a sub-surface palladium carbide phase during acetylene hydrogenation prompted Chan *et al.* to devise a route to form a catalytically useful version of this *in-situ* material.[5–10] With carbon blocking the interstitial site, hydride formation was supressed, but under certain reaction conditions the interstitial carbon was readily removed from the lattice as methane leading to regeneration of Pd−H, so subsequent work within the Tsang group has focussed on a more stable dopant, boron.[11]

Most work involving palladium and boron has previously focussed on ordered Pd_xB_y alloys.[12–14] though Beck had succeeded in the insertion of boron into the octahedral sites of palladium foils by arc welding.[15,16] Boron is a viable candidate for doping palladium nanoparticles interstitially despite the fact boron would violate Hägg's rule.[17,18]

Hägg's rule treats atoms as hard spheres, and if the radius of the dopant (R_I) over the radius of the host metal (R_M) is less than 0.59, the interstitial atom can enter the lattice. From this calculation, boron should not fit within the palladium lattice as $\frac{R_I}{R_M} = 0.63$. However, Hägg's rule does not consider electronic interactions between the particles which stabilise the dopant within the lattice. Chan *et al.* built on these prior efforts leading to a particularly efficient Pd-$^{\text{interstitial}}$B nanoparticle catalyst. However, the heavy use of solvents, particularly tetrahydrofuran (THF) which is a suspected carcinogen and highly flammable, limited Pd-$^{\text{interstitial}}$B's practical use for large-scale commercial operations.[11,19]

Other boron sources have been utilised for Pd-$^{\text{interstitial}}$B synthesis. Krawczyk used diborane (B_2H_6) to build a boron overlayer on the surface of a palladium nanoparticle, which upon heating migrated into the lattice, and more recently Wang *et al.* used dimethylamine borane ($(CH_3)_2NHBH_3$) for the same purpose.[20,21] Major issues including expense and toxicity of boron source, as well as low doping levels mean an alternative avenue to the synthesis of boron doped palladium needs to be explored and developed before commercialisation of the Pd-$^{\text{interstitial}}$B catalyst can occur.

In order to gain a deeper understanding of interstitial palladium modification, palladium doped with lithium, an interstitial material that has yet to be studied, was investigated. Indeed, the palladium-lithium alloy system is quite well understood and has been for some time (Figure 4.1).

In the late 1980's and early 1990's several electrochemical experiments by Dalard *et al.* and Ulmann *et al.* brought up the possibility of at least a small

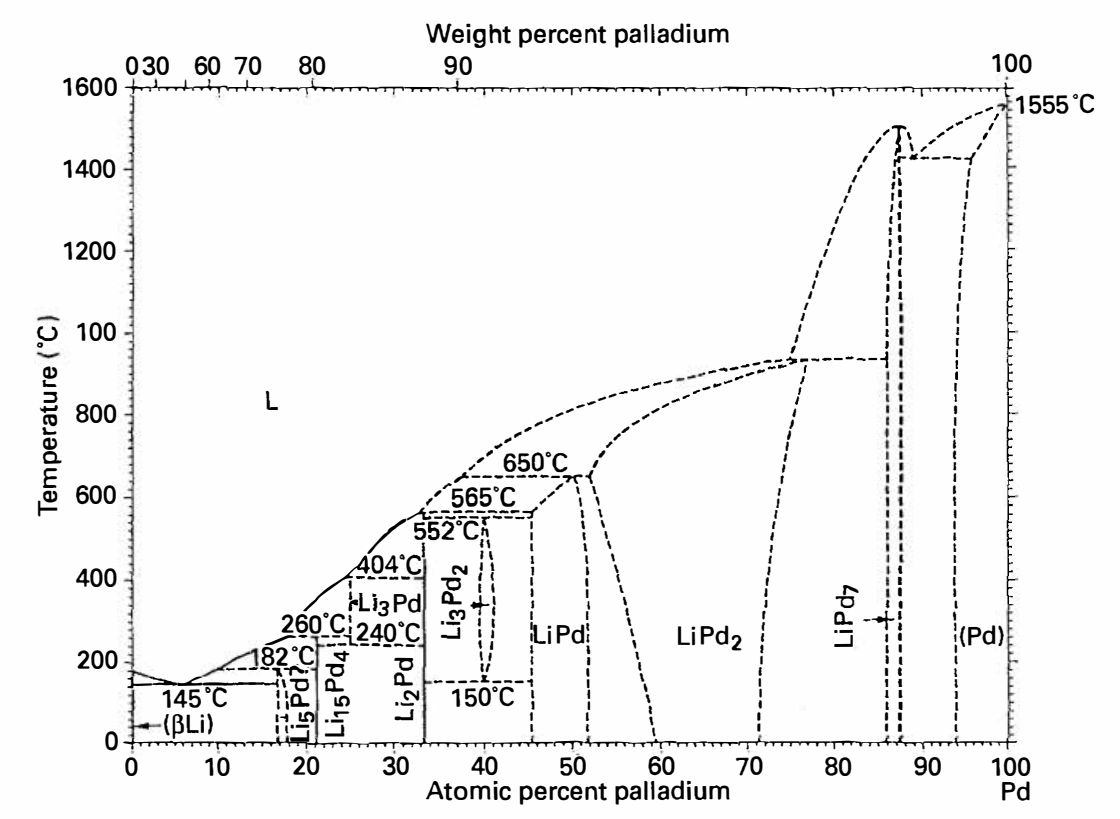

Figure 4.1: A modified version of Loebich's PdLi alloy phase diagram. Reproduced from reference.[22]

amount of lithium entering the interstitial site of palladium. They had observed interesting charging and discharging effects involving the Pd electrode.([23,24]) In 1995 Nohira and Amezawa used eutectic LiCl-KCl melts to electrochemically form Pd-Li alloys, mostly Pd_7Li, on the edges of their palladium electrode, however this was done at 450 °C (above the maximum temperature at which all other palladium interstitial systems are stable) and does not fully explain the observed earlier electrochemical works.[9,11,16,22,25]

In 2000 Yu *et al.* explicitly stated the high likelihood of lithium ions passing through the interstitial sites of the palladium lattice to explain their electrochemical observations.[26] This was explained by comparison to similar charge/discharge phenomena seen in stannic oxides with the formation of SnLi alloys.[27,28] When comparing the radius of Li^+ (76 pm) to the other known interstitial species such as

carbon (70 pm) and boron (84 pm), it would seem likely that Li^+ is able to form an interstitial material with palladium from purely a Hägg's rule based argument, though as we have seen with the boron case, this rule becomes more of a guideline once the electronics of the two species are considered.[11,17,18,29] A study by Sakamoto focussing on the hydrogen absorption characteristics of palladium-rich PdLi alloys noted a linear decrease in palladium lattice parameter between 4 to 10.3 % Li, as would be expected by Vegard's law, which states that the lattice parameter of a solid solution of two constituents is approximately equal to the two constituents' lattice parameters at the same temperature.[30–32] These results are largely consistent with Loebich's phase diagram table (Figure 4.1). Sakamoto *et al.* did see an interesting phase transition in PdLi alloys in the presence of hydrogen, similar to that seen in ternary H−Pd−B alloys.[14,33] Here, hydrogen can still induce a phase change from α to β despite the contraction of the lattice caused by the incorporation of up to 10.6 % lithium into the alloy.

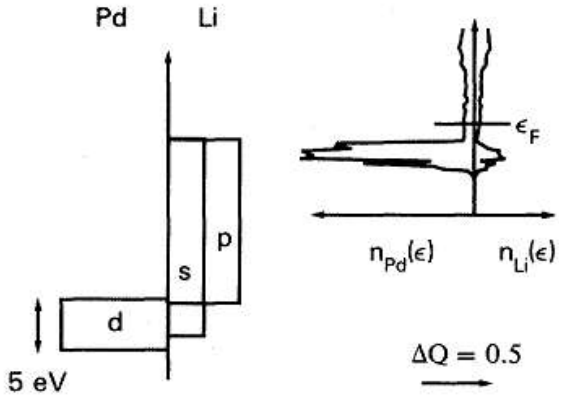

Figure 4.2: The DFT analysis of Gelatt's study on the Pd-$^{\text{interstitial}}$Li system. Reproduced from reference.[34]

Theoretically, work by Gelatt Jr. *et al.* indicated that the palladium-lithium interstitial system should be stable with some overlap between the palladium d-band and the s-band of lithium (Figure 4.2).[34] Herein it is discussed that the palladium d-band is significantly narrowed due to this interaction, reflecting the lattice expansion to accommodate Li, whilst maintaining the face centred cubic structure of palladium.

In 1986, Zaidi conducted a short catalytic experiment involving palladium and lithium acetate in glacial acetic acid for the oxidation of propylene to allyl acetate, and saw an increase in selectivity in the 175 to 200 °C range with up to 25 % LiOAc, however an in-depth explanation given for the observed results proposed the selectivity change was most likely due to LiOAc altering the $Pd(OAc)_2$ equilibrium and not due to any potential interstitial effect.[35]

Physical grinding, or physical mixing, of metal acetates and a support followed by heating has been shown to give excellent dispersions of either single metal, or bimetallic nanoparticles.[36–38] This physical grinding approach to nanoparticle synthesis could provide a route to eliminate the use of expensive and toxic precursors and solvents from the most current synthesis of Pd-^{interstitial}B, and potentially provide a route to the synthesis of a novel Pd-^{interstitial}Li system.[11] In order for physical grinding to be a viable alternative pathway, the solid source (boron or lithium) used needs to decompose at a temperature below 300 °C (above this all known palladium interstitial phases become unstable). The decomposition pathway of the source should leave little to no side products, and those that it does leave should be easily removed. It is important to maintain the interstitial palladium phase and ensure that its catalytic performance is not compromised.

4.2 Objectives

The focus of this chapter is to test alternative synthetic approaches to the Pd-^{interstitial}B catalyst based on the principle of physically grinding the relevant precursors together. These new ground catalysts are compared to the current leading Pd-^{interstitial}B/C synthetic approach *via* BH_3–THF. A number of different combinations of precursors and salts were used in order to determine the best alternative to the current solvent-heavy approach. Similarly, for the novel interstitial catalytic material Pd-^{interstitial}Li/C, two potential synthetic routes were investigated. One

route was solvent based *vis-à-vis* on the borane method of Pd-$^{\text{interstitial}}$B/C synthesis, and one was a grinding approach. Successful catalyst synthesis was initially verified with XRD and TPR. Initial catalytic screening of the prepared catalysts with well-understood liquid phase hydrogenation reactions allowed for determination of the route which gives the most active material.

4.3 Catalyst Preparation

Full details of the synthesis of all catalysts mentioned herein can be found in Chapter 3. In brief, a standard 5 % weight palladium on activated carbon was synthesised as the base catalyst for further modification with boron. The base catalyst was typically a 5 % Pd/C produced by dispersing an activated carbon (normally Vulcan ® XC72R) in butan-1-ol. To this suspension, the required amount of $Pd(NO_3)_2$ in nitric acid was dissolved in butan-1-ol before being added dropwise. This was stirred overnight before filtering and washing with water and ethanol. A clear yellow tinged filtrate indicates the successful anchoring of Pd to the carbon support (some yellow remains due to nitric acid). The catalyst was then dried overnight before reduction in a tubular furnace under a 1:1 mix of $N_2 : H_2$ ramping at $5\,^{\circ}\text{C}\,\text{min}^{-1}$ to 500 °C where it was held for 1 hour before cooling to room temperature. This approach yields nanoparticles of 13 ± 5 nm in size. Larger nanoparticles reportedly are better for interstitial doping because the lattice parameter of Pd nanoparticles contracts as the particles get smaller, thus there is a higher chemical potential to overcome for interstitial insertion.[39]

4.3.1 Palladium Boron Synthesis

The original boron insertion technique by Chan *et al.* involved the suspending of the base Pd/C catalyst in THF under an inert N_2 atmosphere before the dropwise addition of an excess of BH_3 – THF complex solution. The solvent was evaporated off

slowly at 40 °C until a black powder remained. This powder was heated, still under the N_2 atmosphere to 200 °C for 1 hour to drive the boron into the palladium lattice. The resultant black powder was washed with water and ethanol and dried overnight.

The first and second physical grinding approaches involved grinding the base Pd/C with either $NaBH_4$ or $NaBH(OAc)_3$ in a nitrogen glovebox for five minutes, or until a homogeneous powder was formed. The resultant black powder was subsequently heated to 200 °C, to ensure full decomposition of the sodium borohydride and to drive the boron into the Pd lattice. The catalyst was then washed with water and ethanol and dried overnight.

The final physical grinding approach involved grinding $NaBH_4$ with $Pd(OAc)_2$ and activated carbon, in effect a one pot approach to synthesising the Pd-$^{\text{interstitial}}$B/C catalyst, minimising the use of solvents in the chemical process.

4.3.2 Palladium Lithium Synthesis

In order to successfully insert the lithium into the palladium lattice, lithium needs to be deposited onto the metal particles themselves. For the solvent based approach this was achieved by initially suspending the Pd/C in THF under an inert nitrogen atmosphere, before bubbling hydrogen through the suspension to create palladium hydride. It was hoped that through the dropwise addition of *n*-butyllithium the hydrogen on the palladium would exchange with the lithium forming Pd–Li/C and butane. After the evaporation of the solvent at 50 °C under nitrogen, the sample was then heated to 250 °C in order to drive the lithium into the lattice. The resultant powder was subsequently washed with water and ethanol in a procedure analogous to the purification of Pd-$^{\text{interstitial}}$B/C.

A grinding approach was attempted using lithium acetate as the precursor to Pd-$^{\text{interstitial}}$Li/C in a similar way to how $NaBH_4$ and $NaBH(OAc)_3$ were used in the synthesis of Pd-$^{\text{interstitial}}$B/C. The decomposition of metal acetates is known

to be a complex procedure with the effect of temperature playing a key role, especially in the case of mixed metal acetate systems.[36,37,40–42] It is probable, as was the case with the boron sources, that lithium acetate will decompose at a much lower temperature than its melting point of 286 °C in the presence of palladium nanoparticles.[29] After grinding LiOAc and Pd/C together until a homogeneous powder was formed, the black powder was placed under a nitrogen atmosphere and heated to 250 °C for two hours. After cooling to room temperature the Pd-^{interstitial}Li/C was washed with water and ethanol.

4.4 Verification of Grinding Approaches to Pd-$^{\mathbf{interstitial}}$B/C

4.4.1 $NaBH_4$ as a Precursor

$NaBH_4$ is an interesting choice as a boron source as it has had many applications as a reducing agent for both catalyst preparation and as a hydrogen source for use in catalytic hydrogenations.[43–45] Its effectiveness comes from the *in-situ* decomposition of the borohydride releasing strongly nucleophilic hydride moieties.[46,47] This decomposition, which readily happens at room temperature, will deposit boron species onto the surface of the palladium nanoparticles. However, the grinding approach necessitated the use of an inert atmosphere for two reasons. Firstly, to prevent the catalysed hydrogen-oxygen recombination reaction igniting the carbon support and secondly, to prevent oxidation of the boron species deposited onto the metal surface.

Through the work of Chan *et al.* it is known that optimal doping is achieved around 25 equivalents of boron to palladium, with the limitation being contact with palladium nanoparticles as the carbon support can take up a large quantity of the deposited boron. To ensure that all the nanoparticles are in contact with boron, the whole support needs to be covered with $NaBH_4$.[11] In this system this corresponds to

40 mg of sodium borohydride for 100 mg of 5 % palladium on carbon based catalyst.

Initial verification of the successful insertion of boron into the palladium lattice came *via* XRD. Figure 4.3 shows an expansion of the palladium lattice from the bulk value of 3.89 Å to approximately 4.00 Å, the lattice parameter of the β-phase of palladium (the peaks denoted with ∗). This lattice expansion is evident in all palladium interstitials and can be seen in XRD through a downshift of the 2θ values for the typical palladium reflections. The satellite peaks (marked with ⧫) observed at $2\theta = 35$ and 41° are attributable to non-interstitial boron oxide species.[11] It was observed that washing the catalysts with water and ethanol removed the majority of the boron oxide species with no appreciable loss in boron content within the palladium lattice. Subsequently, all catalysts were washed in this manner.

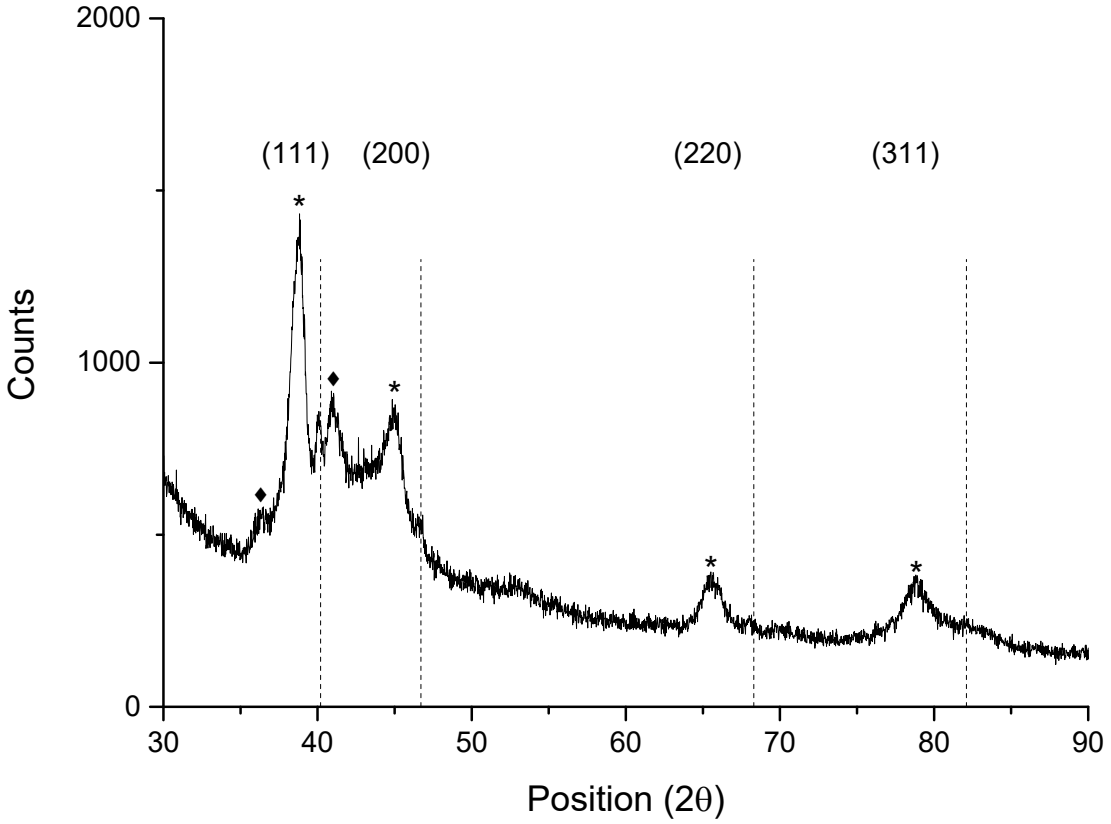

Figure 4.3: XRD of unwashed Pd-$^{\text{interstitial}}$B/C synthesised *via* $NaBH_4$. The dashed lines indicate the positions of the (111), (200), (220) and (311) reflections of unmodified palladium. ∗ indicates the expanded lattice parameters of the Pd-$^{\text{interstitial}}$B phase. The peaks denoted by ⧫'s are attributed to boron oxide species.

An empirical formula (Equation 4.1), derived by Beck and Mittemeijer, demonstrates the linear relationship between boron content within the palladium lattice (x_B^r) and the observed lattice parameter ($a(x_B^r)$).[15,16,48]

$$a(x_B^r) = 0.38920 + 0.06882(44)x_B^r \quad \text{(nm)} \tag{4.1}$$

Through the use of this equation it is possible to determine the boron content within this sample, with its expanded lattice parameter of 4.02 Å equivalent to 20.0 % of the octahedral sites occupied with boron. Within error, this is at the maximum occupancy of boron within the lattice, as seen by Beck *et al.*, of 20 %.[15,16] The total occupancy of the octahedral sites in the Pd-$^{\text{interstitial}}$B/C produced *via* this two-step method was also shown through TPR (Figure 4.4) with the elimination of the β-hydride peak. This peak arises from interstitial hydrogen (palladium hydride), located within the palladium nanoparticles, desorbing. Its absence give a strong indication that the nanoparticle is saturated with a new interstitial dopant, in this case boron.[49]

4.4.2 $NaBH_4$ One-Pot Synthetic Approach

With a successful demonstration that this approach can dope premade palladium nanoparticles, a one-pot grinding approach was devised. The carbon support, palladium acetate and sodium borohydride were ground together until a homogeneous powder formed, an advantage here being that, without the presence of Pd nanoparticles, the borohydride doesn't spontaneously decompose to release flammable hydrogen. A range of different heating temperatures and durations were attempted to try to optimise the synthesis of Pd-$^{\text{interstitial}}$B/C, summarised in Table 4.1. Palladium acetate decomposes at about 200 °C when heated in an inert atmosphere, the same temperature that boron begins to incorporate into the palladium lattice.[36,50] PG in Table 4.1 is a label referring to the physical

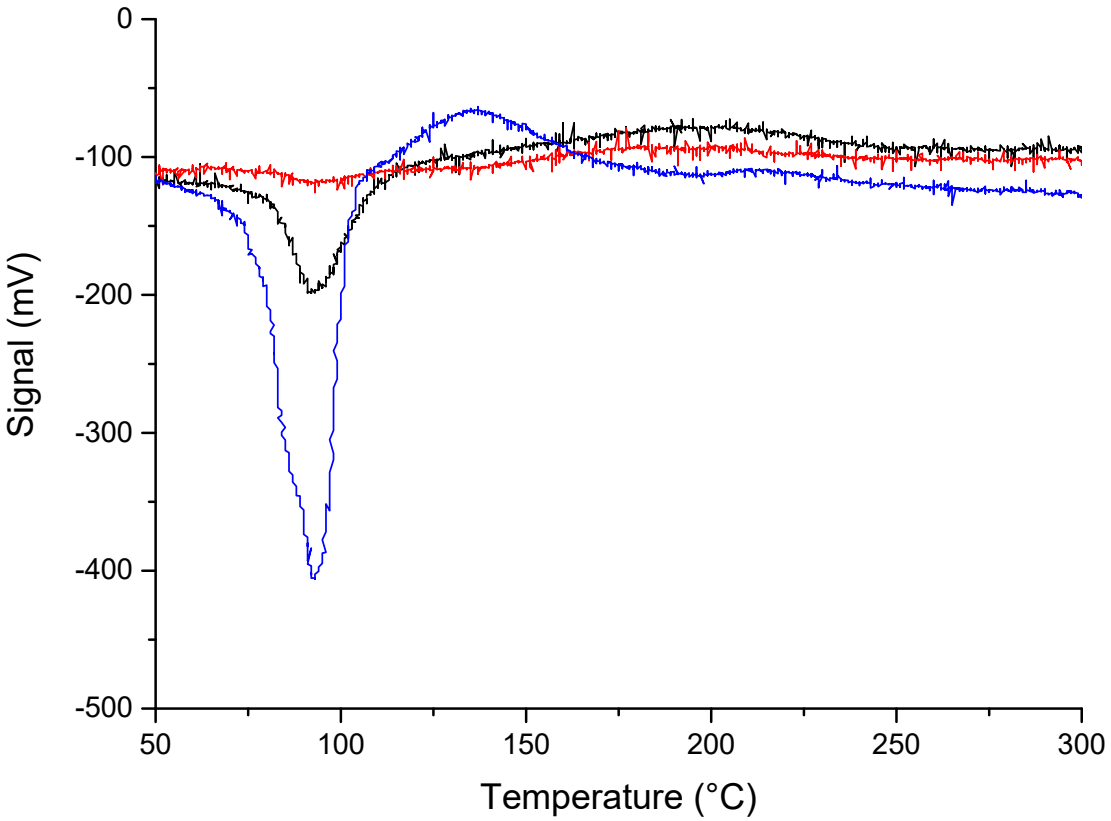

Figure 4.4: TPR of unmodified Pd/C (blue), one-pot synthesised Pd-$^{\text{interstitial}}$B/C (black) and two-pot synthesised Pd-$^{\text{interstitial}}$B/C (red). The feature at approximately 80 °C is the β-hydride desorption peak.

grinding experiment number.

Sample PG3, the powder XRD for which showed incomplete expansion of the lattice (3.99 Å), was evaluated by TPR and compared to unmodified and two-pot synthesised Pd-$^{\text{interstitial}}$B/C. (Figure 4.4). The partial elimination of the β-hydride peak in the case of the one-pot synthesis is consistent with an incomplete occupation of the octahedral sites.[12] It is unfortunately difficult to estimate what percentage of the remaining sites are occupied by hydrogen as the relationship between the solubility of hydrogen in Pd-$^{\text{interstitial}}$B based alloys is non-linear with respect to boron content.[14]

It was found that the optimal heating temperature is 200 °C, slightly above the palladium acetate decomposition temperature. Increasing the temperature beyond this was detrimental to boron insertion, similar to Chan *et al.*'s observations for

Table 4.1: A summary of the attempted syntheses of Pd-$^{\text{interstitial}}$B/C *via* a one pot strategy with varied temperature and heating lengths. Site occupancy calculated using Equation 4.1. The XRD profiles can be found in Figure 4.6

Sample	Temp. (°C)	Heating Length (hours)	Lattice Parameter (Å)	Interstitial Site Occupancy (%)
PG1	200	2	3.99	14.7
PG2	200	4	4.01	18.0
PG3	260	2	3.99	14.7
PG4	290	2	3.99	14.7
PG5	290	4	3.99	14.7
PG6	350	4	3.98	13.1

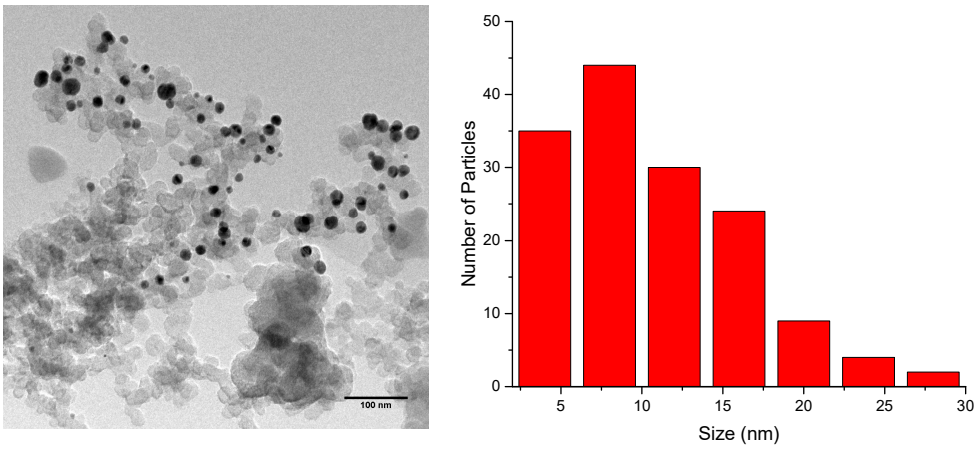

Figure 4.5: TEM image of PG2 and a histogram showing the wide range of particle sizes present in a sample of Pd-$^{\text{interstitial}}$B prepared *via* a one-pot process.

boron doping *via* BH_3–THF (see Figure 4.6).[11] It was interesting to note that doubling the heating time increased boron incorporation, suggesting that kinetics tied to the particle size may be the limiting factor. The very small nanoparticles which initially form have a lattice parameter too low to accept the phase transition to β-palladium boride due to surface stress. Once the particles have increased sufficiently in size, boron can be incorporated.[51,52]

Heating the samples for longer allows for more palladium aggregation, giving particles large enough to accept boron into the lattice. However, this has the disadvantage of losing some control over particle size distribution, as was seen through TEM (Figure 4.5). PG2 (200 °C, 4 h) has a mean size of 9.17 nm with

a standard deviation of $\sigma = 6.32\,\text{nm}$.

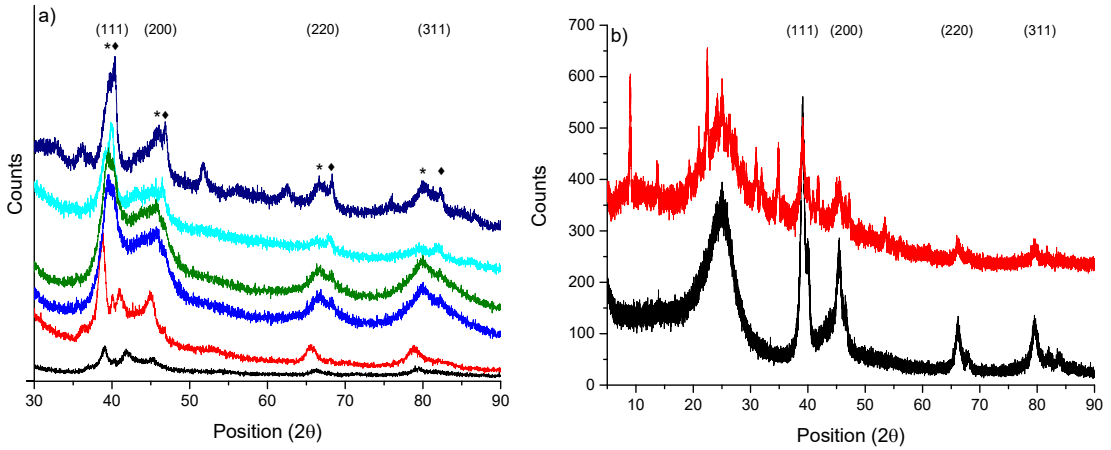

Figure 4.6: a) The XRD profiles for PG1 to PG6. ∗ and ♦ refer to the (111), (200), (220) and (311) reflections for the expanded Pd-$^{\text{interstitial}}$B phase and Pd respectively. b) An illustration of the difference in the XRD profiles of washed (black) and unwashed (red) Pd-$^{\text{interstitial}}$B show the remarkable effects of washing the catalysts with water and ethanol. It appears the vast majority of unwanted boron species were removed, leaving behind the expanded lattice system, with no loss of incorporation.

4.4.3 $NaBH(OAc)_3$ as a Precursor

Another boron source, sodium triacetoxyborohydride, was also attempted for Pd-$^{\text{interstitial}}$B/C synthesis from ready-made Pd/C nanoparticles. A one-pot approach wasn't attempted as $NaBH(OAc)_3$ melts and subsequently decomposes at 116 to 120 °C, below the temperature of palladium acetate decomposition.

As $NaBH(OAc)_3$ has such a low boron content by mass compared to both BH_3–THF and $NaBH_4$ the initial synthesis attempted used a ratio of 10:1 boron to palladium where other approaches use a ratio close to 25:1. This ratio gave a boron occupancy level of 14.7 %. Despite increasing sodium triacetoxyborohydride content in the synthesis four-fold (a final ratio of 85:1), the system was unable to reach total boron incorporation, peaking at 16.1 % (summarised in Table 4.2). Such a large amount of $NaBH(OAc)_3$ is required because it melts and decomposes before the temperature of boron incorporation into the lattice meaning a significant amount of boron lost to the atmosphere prior to incorporation.

Table 4.2: A summary of the attempted syntheses of Pd-$^{\text{interstitial}}$B/C using different Pd/C to $NaBH(OAc)_3$ ratios. All catalysts were heated to 200 °C for 2 hours. Site occupancy calculated using Equation 4.1.

Sample	Pd/C (mg)	$NaBH(OAc)_3$ (mg)	Lattice Parameter (Å)	Interstitial Site Occupancy (%)
PG7	100	212	3.99	14.7
PG8	100	424	4.00	16.1
PG9	200	1696	4.00	16.1

4.5 Initial Verification of Pd-$^{\text{interstitial}}$Li Synthesis

4.5.1 *n*-Butyllithium as a Precursor

A 1.6 M solution of *n*-butyllithium in hexanes was added dropwise to a suspension of Pd/C in THF under nitrogen before the solvents were evaporated, giving a palladium surface covered in Li species. This was heated to 250 °C under N_2 to drive the Li into the Pd lattice. As with the Pd-$^{\text{interstitial}}$B/C synthesis approaches, initial verification of successful lithium insertion came from XRD and TPR (Figure 4.7).

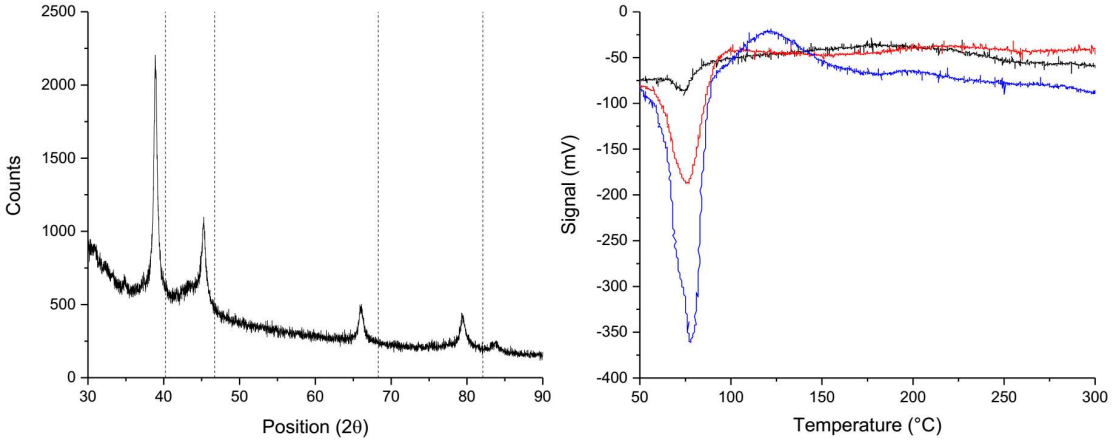

Figure 4.7: XRD of Pd-$^{\text{interstitial}}$Li/C synthesised *via* *n*-butyllithium. The dashed lines indicate the positions of the (111), (200), (220) and (311) reflections of unmodified palladium, respectively. The TPR features unmodified Pd/C (blue), an initial TPR of Pd-$^{\text{interstitial}}$Li/C (black) and a subsequent run (red). The feature at approximately 80 °C is the β-hydride desorption peak.

XRD shows a clear lattice expansion of 3 % compared to unmodified palladium.

As this is a novel material, there is no existing equation similar to Equation 4.1 to estimate total Li insertion. From TPR we observe the majority elimination of the β-hydride peak, suggesting the majority of the sites are occupied by lithium. It is interesting to note that after heating to 600 °C under hydrogen, cooling to 40 °C and re-running the TPR we observe a larger β-hydride peak, indicating removal of some of the interstitially located lithium, but not all, when compared to unmodified palladium.

4.5.2 Lithium Acetate as a Precursor

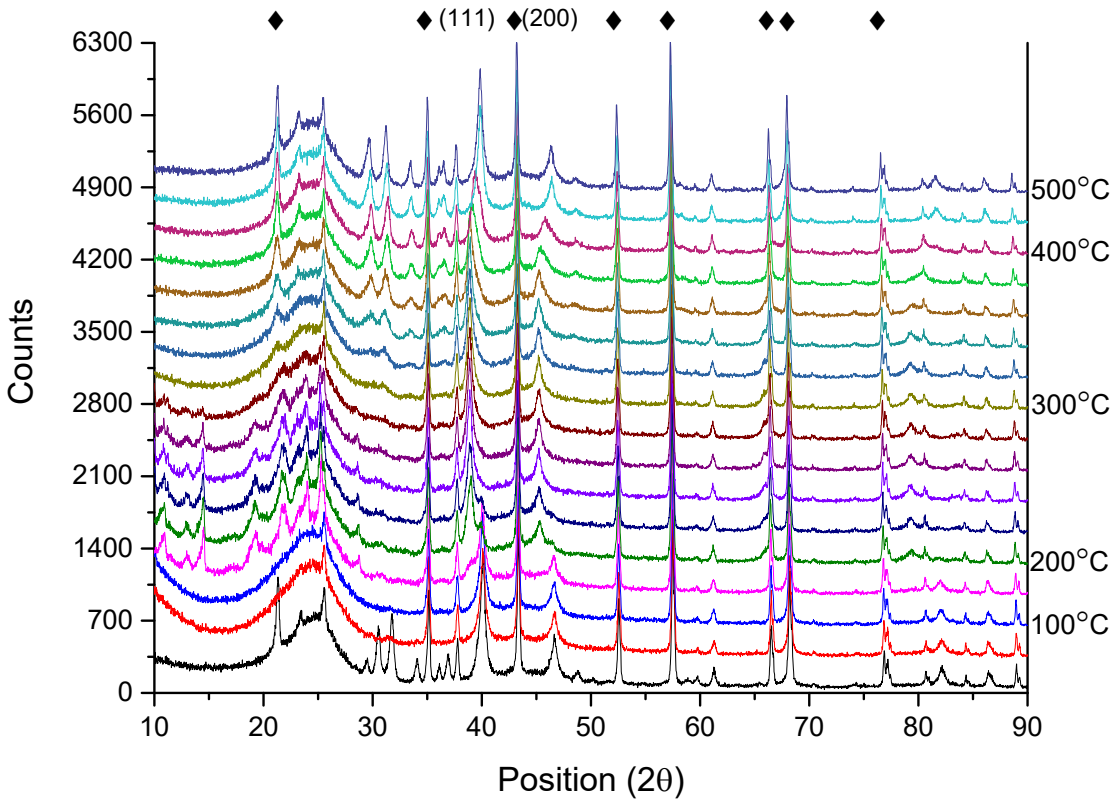

Figure 4.8: *In-situ* XRD profiles of Pd/C + LiOAc under heating. Scans were taken at 30, 50, 100, 150, 200, 220, 240, 260, 280, 300, 320, 340, 360, 380, 400, 450 and 500 °C and have been offset to clearly display the increase in lattice parameter in the 200 to 400 °C range. ♦'s indicate the peak positions of the alumina sample holder.

In order to probe the viability of grinding Pd/C with LiOAc as a synthetic route to Pd-$^{\text{interstitial}}$Li/C, the reaction was followed by *in-situ* XRD. The ground sample

was heated under a helium flow to 500 °C with scans taken at regular intervals (Figure 4.8). There are several interesting features to note in the profile, for example the features at 2θ = 10 to 30° showing a number of crystalline species, most likely lithium carbonate or lithium oxide, evolving as the temperature increases. This is corroborated by differential scanning calorimetry (DSC) analysis conducted on a Pd/C + LiOAc ground sample which sees some weight loss at this point consistent with the partial decomposition of the lithium acetate (Figure 4.10).

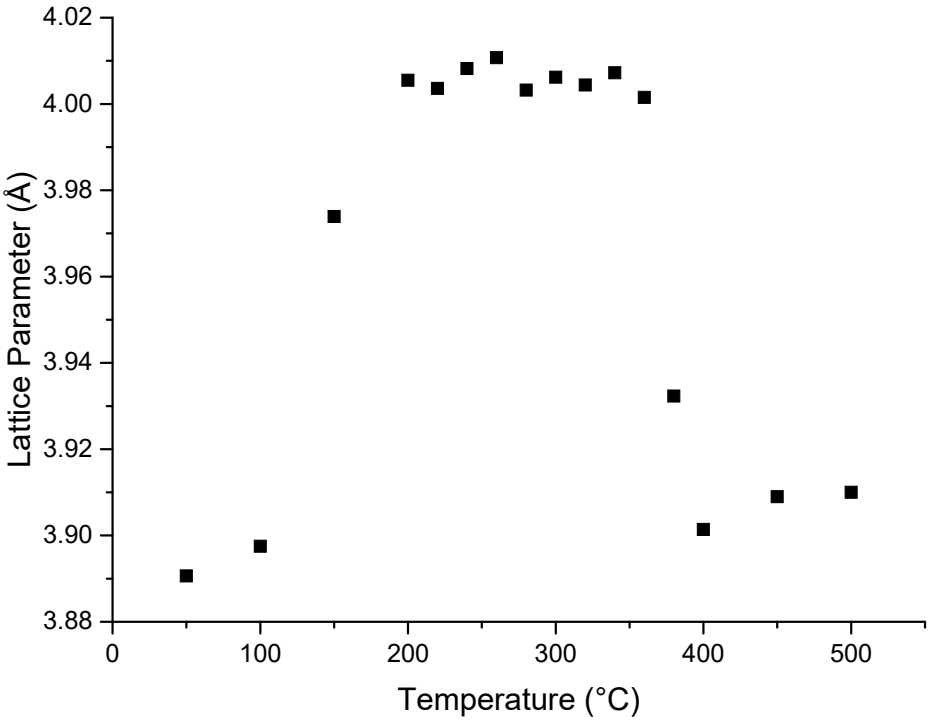

Figure 4.9: A graphical representation of how the palladium lattice parameter changes with heating.

The key feature in Figure 4.8 is how the palladium reflections change with heating (graphically shown in Figure 4.9). Taking the (111) peak as a reference, there is a clear shift in the lattice to 4.00 Å at 200 °C before reaching a maximum of 4.01 Å at 260 °C, the point of maximum palladium occupancy by lithium. Figure 4.10 shows a positive heat-flow in this 200 to 400 °C region due to the incorporation of lithium into the lattice. Similarly, beyond 400 °C there is an exothermic process which is consistent with Li leaving the lattice, with weight losses due to the breakdown

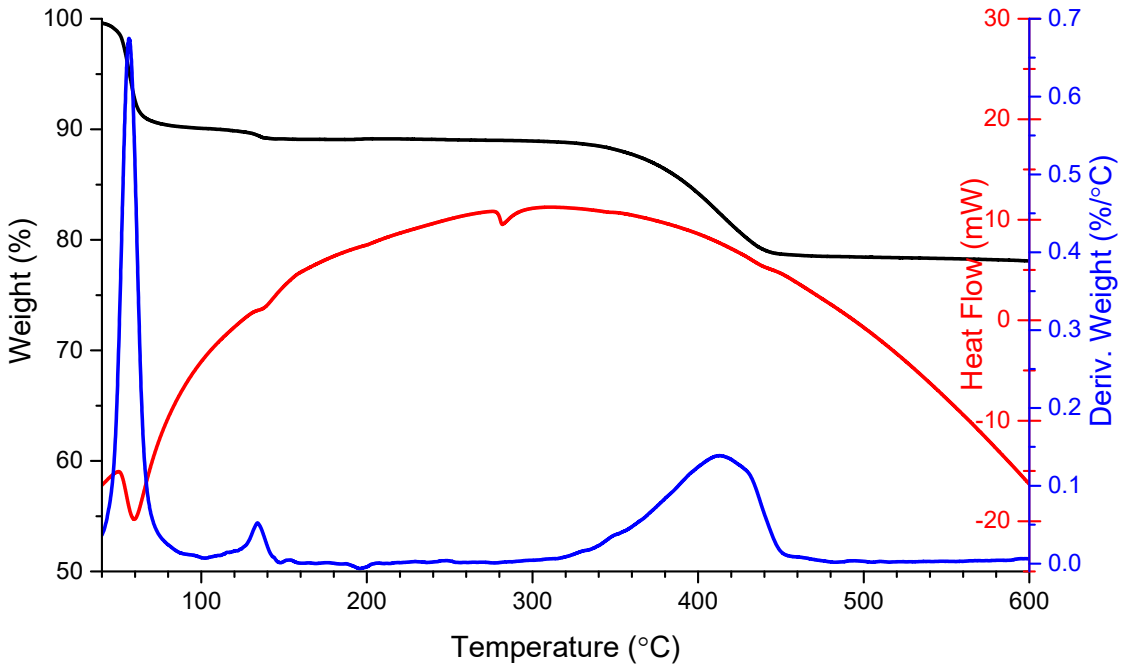

Figure 4.10: DSC of Pd/C + LiOAc (3.272 mg total mass). The sample was heated under a constant flow of nitrogen, with a furnace ramp rate of 5 °C min^{-1}

of some remaining lithiate species on the carbon support and sublimation of the lithium. The early weight loss in the sample is caused by the dehydration of the lithium acetate precursor which readily forms $LiOAc \cdot 2\,H_2O$.

From these results it is apparent that grinding with LiOAc is a viable route to Pd-^{interstitial}Li/C, with 250 °C an ideal temperature to heat the sample to achieve maximum lithium insertion, followed by washings with water and ethanol to remove unwanted lithium surface species.

A sample of Pd-^{interstitial}Li/C synthesised as above was subjected to similar *in-situ* XRD, this time in air. As shown in Figure 4.11, the sample is stable until 150 to 200 °C, at which point the lattice shrinks back to 3.889 Å, i.e. the lithium has left the palladium lattice. This suggests that the Pd-^{interstitial}Li/C system is stable in air at room temperature.

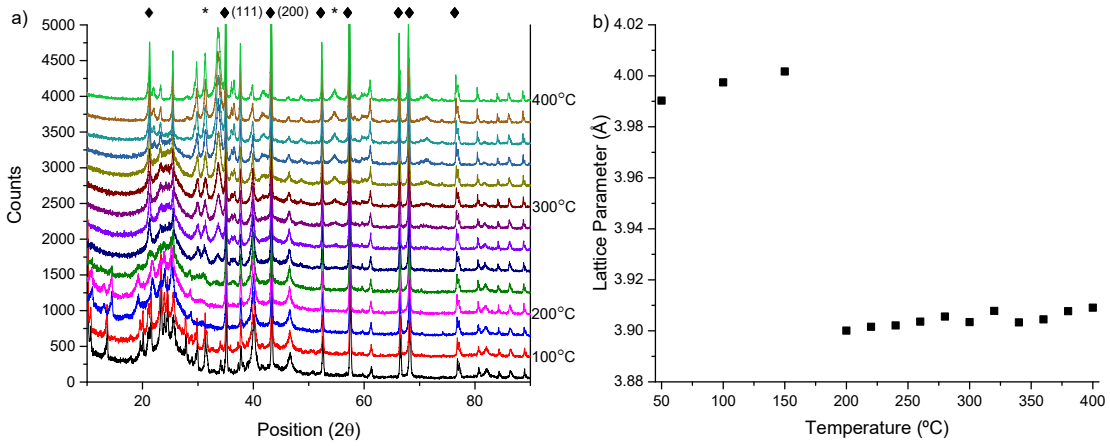

Figure 4.11: a) The *in-situ* XRD of heating Pd-$^{\text{interstitial}}$Li/C in air. At 300 °C palladium oxide starts to form as evidenced by the appearance of peaks at 34° and 55° (denoted with ∗), ♦'s indicate the peak positions of the alumina sample holder. b) The effect upon the lattice parameter.

4.6 Catalytic Screening of New Materials

Two new synthetic routes to Pd-$^{\text{interstitial}}$B/C have been successfully demonstrated, as have two routes to the novel material Pd-$^{\text{interstitial}}$Li/C. Initial verification of the intercalation of both boron and lithium into the palladium lattice came from TPR and XRD experimental results that coincided well with the characterisations of other known palladium interstitials (e.g. Pd-$^{\text{interstitial}}$C). Chapter 5 details the more in-depth characterisations undertaken on the Pd-$^{\text{interstitial}}$B/C and Pd-$^{\text{interstitial}}$Li/C materials. Before this however, it is important to screen the synthesised materials in order to determine which route gives the most active and selective catalyst as this will be of the most use in an industrial setting. After all, despite washing all catalyst samples with ethanol and water to remove unwanted boron or lithium species from the surface (see Figure 4.6b), some of these species still remain.

The Pd-$^{\text{interstitial}}$B/C materials prepared *via* the grinding techniques are likely to still have sodium present on the surface of the support. Alkali metals are known to have a promoting effect on some catalytic reactions so it will be of interest to see what difference the catalysts have in four trial hydrogenations.[53,54] In order

Table 4.3: Summary of the calculated catalyst surface areas (in $m^2 g^{-1}_{catalyst}$ and $m^2 g^{-1}_{Pd}$) by CO pulse chemisorption. All catalysts are 5 % Pd by weight and are labelled by their modifier.

Catalyst Modifier	Surface Area ($\mathbf{m^2 g^{-1}_{catalyst}}$)	Surface Area ($\mathbf{m^2 g^{-1}_{Pd}}$)
Unmodified	1.244	24.788
BH_3-THF	1.015	20.238
$NaBH_4$	0.978	19.495
$NaBH(OAc)_3$	0.543	10.823
n-BuLi	0.121	2.406
LiOAc	1.131	22.543

to minimise variance between the samples all catalysts were synthesised from the same batch of pre-made 5 % Pd/C. This had the advantage of ensuring that any changes in catalyst surface area would be a result of the modification techniques, and not due to variances between different batches.

For full details of the set-up for the catalytic studies see Chapter 3. The reactions studied cover the hydrogenation of a number of alkynes and a nitro group in ethanol containing molecule. The choice of reactants was to provide a good overview of the capabilities of each catalyst.

From the surface areas measured by CO chemisorption (Table 4.3) it is clear that the *n*-BuLi and $NaBH(OAc)_3$ modifiers have significantly decreased the palladium surface area and are therefore expected to perform poorest in the comparative hydrogenation studies.

4.6.1 Phenylacetylene Hydrogenation

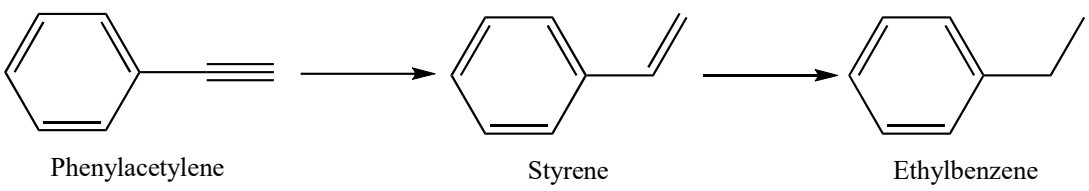

Figure 4.12: The hydrogenation of phenylacetylene (PA) proceeds *via* styrene (STY) with the final product being ethylbenzene (EB).

Table 4.4: A summary of the phenylacetylene hydrogenation products at the one uptake point. The rates of each stage of the reaction are also compared. Rates were measured for R_1 3 minutes (approximately 5 mL H_2 uptake) into the reaction to remove any activation effects due to the catalyst being partially oxidised, and for R_2 after 65 mL of H_2 uptake as by this point all phenylacetylene was consumed.

Catalyst Modifier	**One-Uptake Products (%)**			**R (s^{-1})**		
	PA	STY	EB	R_1	R_2	R_1/R_2
Unmodified	5.7	88.5	5.8	303	293	1.0
BH_3–THF	5.8	89.3	4.9	385	390	1.0
$NaBH_4$	8.5	85.3	6.2	365	368	1.0
$NaBH(OAc)_3$	5.5	88.9	5.6	241	269	0.9
LiOAc	4.3	88.9	6.9	346	404	0.9
n-BuLi	34.0	62.9	3.1	127	141	0.9

Phenylacetylene hydrogenation (reaction pathway: Figure 4.12) was used as an example of a terminal alkyne hydrogenation. Terminal alkyne hydrogenations are, in general, more difficult to control than the corresponding alkene due to the stronger alkyne adsorption on the metal surface.[55] Therefore, to see no appreciable change in reaction rate for the first hydrogenation stage of this reaction with a comparatively faster reaction rate for the second stage is not uncommon.

The first stage of the reaction is the period during which 0 to 60 mL of hydrogen is consumed by the system, corresponding to the uptake of one molar equivalent of hydrogen. 60 mL will be referred to as the one-uptake point. The second stage of the reaction starts after the 60 mL point and stops after two molar equivalents of H_2 have been consumed (i.e. all alkene has become alkane). Stopping the reaction slightly before the one-uptake point gives the selectivity of the catalysts to the desired alkene product. Samples were taken at just before the one-uptake point and at the end of the reaction and analysed by GC. All samples gave 100 % ethylbenzene at the end of the reaction. Similarly, comparing the rate of the reaction (in s^{-1}) before (R_1) and after (R_2) this point gives an indication of how selective a catalyst is, with a high R_1 and low R_2 desired.[56] These results are summarised in Table 4.4.

Figure 4.13 and Table 4.4 show that the Pd-$^{\text{interstitial}}$B/C catalyst modified with

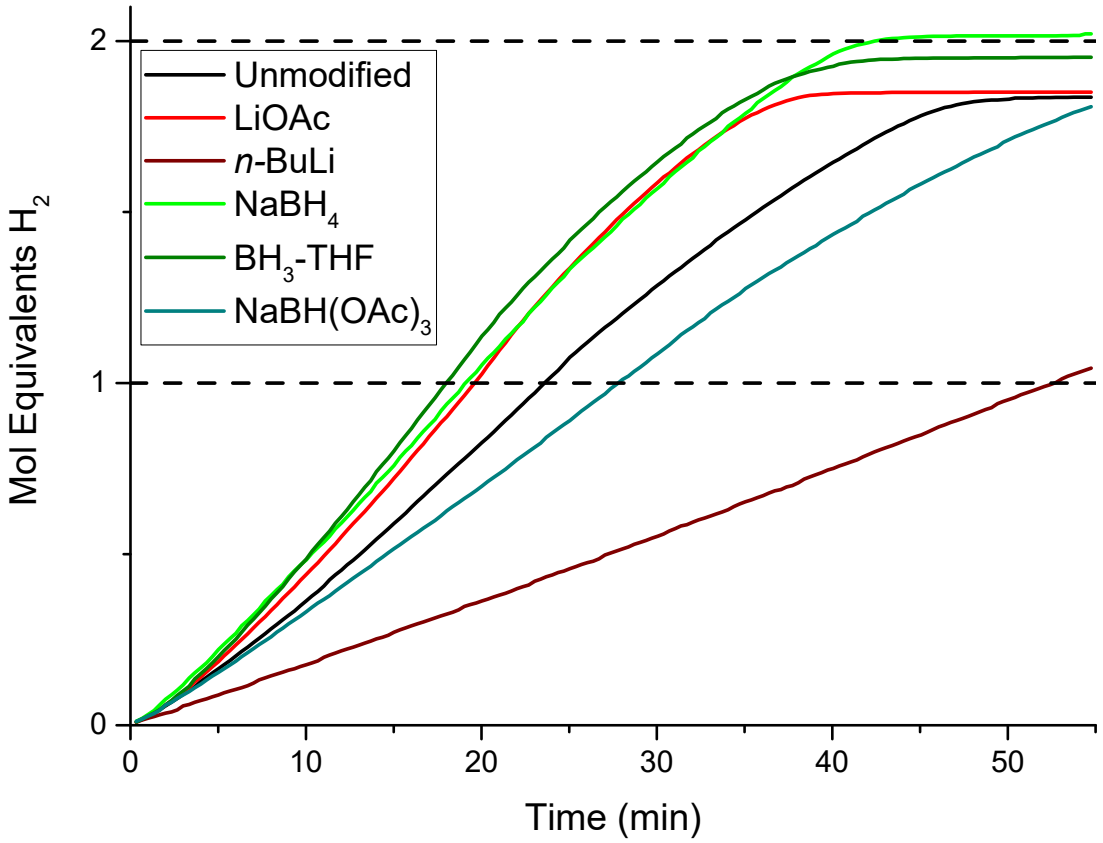

Figure 4.13: The hydrogenation of phenylacetylene with various catalysts. Conditions: 2.50 mmol alkyne, 2.50 µmol catalyst, in ethanol, 3 bar H_2, 30 °C, 1200 rpm stirrer speed.

borane-tetrahydrofuran complex is narrowly the most active catalyst, having a slightly higher reaction rate than the sodium borohydride modified catalyst (385 and 365 s^{-1} respectively). Both of which are more active than unmodified Pd/C, with the sodium boroacetate modified Pd-^{interstitial}B/C lagging considerably behind. This is likely due to the lower surface area of this catalyst compared to the other boron modification techniques. This is caused by the amount of $NaBH(OAc)_3$ required to fully boronate the lattice leaving a considerable amount of Na and other acetate decomposition fragments blocking the surface of the support and catalyst, along with potential "islands" of B_xO_y on the surface of the palladium that the washing treatment has not fully removed.[57] It is interesting to note however, that despite a lower surface area, the incomplete boronylation from the $NaBH(OAc)_3$ modifier somewhat offsets the loss in activity that would be expected from a purely

surface area related argument.

Furthermore, boron modification shows no appreciable improvement in catalyst selectivity, all giving R_1/R_2 values of between 0.9 ($NaBH_4$) to 1.0 (BH_3-THF) with unmodified Pd/C slightly above unity. GC analysis indicates that all catalysts have excellent selectivity approaching the one-uptake point with the borane modification having the best styrene selectivity at 89 %. Similarly, for the Pd-$^{\text{interstitial}}$Li/C catalysts, the R_1/R_2 values are around 0.9, slightly worse than the boron modified catalysts suggesting worsened selectivity in the second stage, despite the initial rate for the LiOAc modified catalyst being comparable to the best of the boron modified catalysts. It is apparent that the Pd-$^{\text{interstitial}}$Li/C synthesised *via* butyllithium is very slow in comparison to the lithium acetate modified Pd-$^{\text{interstitial}}$Li/C. This is likely due to the severity of butyllithium as a reagent. It will react with, and lithiate, the remaining functional groups on the carbon support as well as the palladium nanoparticles.[58] This degree of support modification has had a large negative impact on the surface area of the Pd nanoparticles, and hence the catalytic activity.

One interesting observation is the slight increase in the rate of hydrogenation for the terminal alkene phenylethylene as opposed to the terminal alkyne with some of the catalysts (Table 4.4). The rates for the hydrogenation of the terminal alkene relative to the terminal alkyne in are known to be similar.[59] It is often seen for internal alkenes that complete hydrogenation proceeds through a progressive bond shift to less stable isomers until the double bond reaches the terminal position and can be completely hydrogenated.[60] Therefore the terminal alkene is a very reactive species, and as the phenylacetylene binds so strongly to the palladium in this system, is more reactive than the terminal alkyne.

4.6.2 Diphenylacetylene Hydrogenation

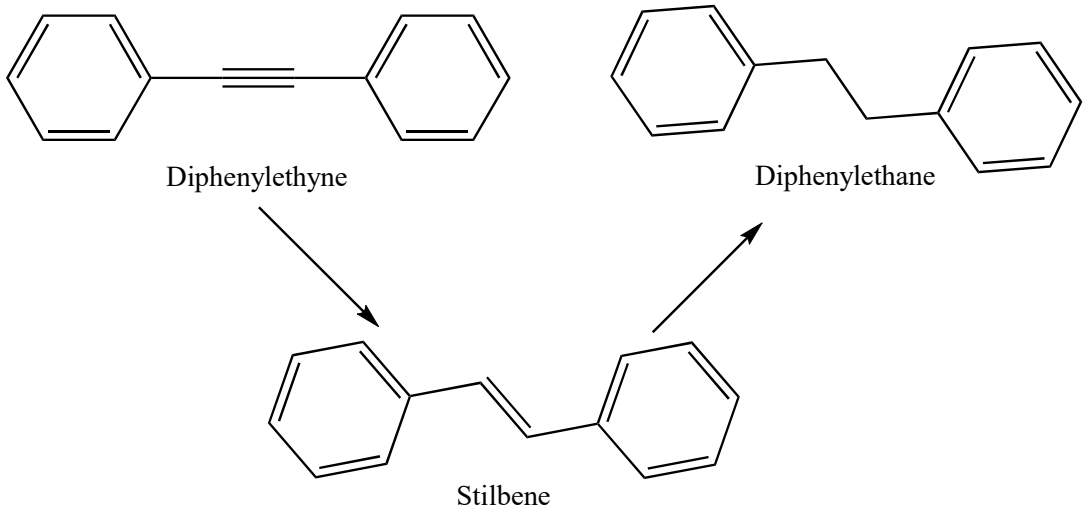

Figure 4.14: The hydrogenation of diphenylacetylene (DPA) proceeds *via* stilbene (STB) with the final product being diphenylethane (DPE).

Table 4.5: A summary of the diphenylacetylene hydrogenation products at the one uptake point. The rates of each stage of the reaction are also compared. Rates were measured for R_1 3 minutes (approximately 5 mL H_2 uptake) into the reaction to remove any activation effects due to the catalyst being partially oxidised, and for R_2 after 65 mL of H_2 uptake as by this point all diphenylacetylene was consumed.

Catalyst Modifier	**One-Uptake Products (%)**				**R (s^{-1})**			***cis*-Selectivity (%)**
	DPA	*cis*-STB	*trans*-STB	DPE	R_1	R_2	R_1/R_2	
Unmodified	10.3	84.1	2.1	3.5	511	180	2.8	93.7
BH_3-THF	14.0	79.9	2.1	4.0	455	153	3.0	92.8
$NaBH_4$	9.0	81.5	3.0	6.5	495	216	2.3	89.6
$NaBH(OAc)_3$	12.5	80.6	2.8	4.1	401	133	3.0	92.2
LiOAc	8.4	82.8	2.8	5.9	520	191	2.7	90.5
n-BuLi	66.8	30.4	1.1	1.7	172	105	1.6	91.6

The differences between the catalysts here are less pronounced than for the phenylacetylene hydrogenation, though again the sodium triacetoxyborohydride modified catalyst is the least active of the three Pd-$^{\text{interstitial}}$B/C catalysts and the butyllithium modified Pd-$^{\text{interstitial}}$Li/C catalyst is considerably worse than the

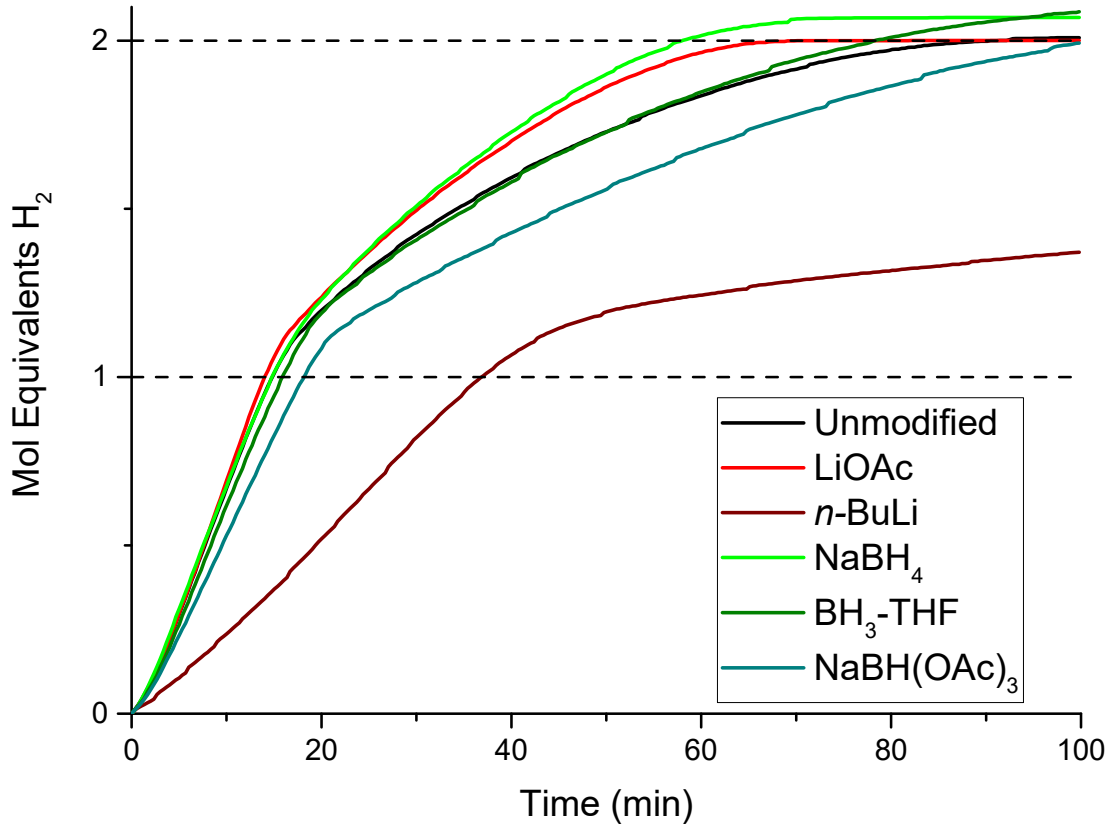

Figure 4.15: The hydrogenation of diphenylacetylene with various catalysts. Conditions: 2.50 mmol alkyne, 2.50 µmol catalyst, in ethanol, 3 bar H_2, 30 °C, 1200 rpm stirrer speed.

LiOAc modified catalyst. This is consistent with the result seen in the hydrogenation of phenylacetylene and the observed surface area differences.

Interestingly, the $NaBH_4$ modified palladium exhibits poor selectivity toward STB during the second stage of the reaction, as evidenced by an R_1/R_2 value of 2.3 compared to close to 3.0 for the other modification techniques. The $NaBH_4$ modified catalyst also shows slightly increased isomerisation with 3.0 % *trans*-STB at the one-uptake point, compared with 2.1 % for the unmodified and borane modified catalysts. The LiOAc modified catalyst also has a slightly higher isomerisation rate. This catalyst has an overall faster rate than the unmodified Pd/C for both stages of the reaction, with this small increase in overall rate, also seen by the $NaBH_4$ modified catalyst, causing a corresponding loss in *cis* selectivity. This drop in selectivity is small in relation to the other materials, 86.9 % compared with 91 to 94 %.

4.6.3 *ortho*-Chloronitrobenzene Hydrogenation

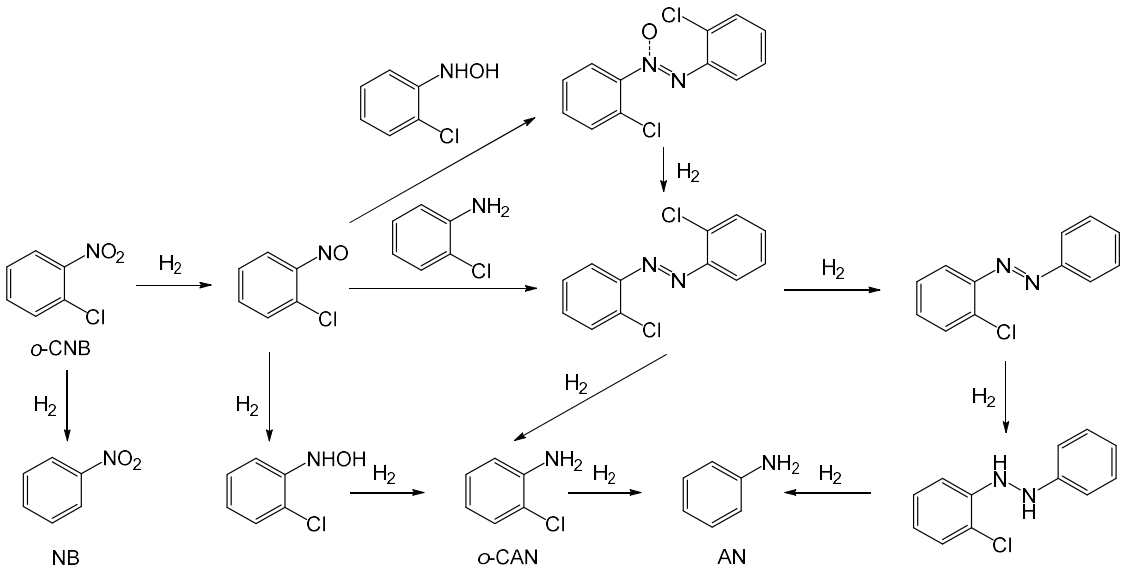

Figure 4.16: The hydrogenation of *ortho*-chloronitrobenzene (CNB) is complex and proceeds *via* a number of intermediates with several hydrogenation products possible. The major products are aniline (AN), chloroaniline (CAN) and nitrobenzene (NB).

The hydrogenation of the nitro group in *ortho*-chloronitrobenzene (CNB) to the corresponding chloroaniline (CAN), while limiting dechlorination to aniline (AN), is a strategically important reaction for a number of industries.[61] Here, differences in the reactivity and selectivity of the interstitially modified catalysts for the hydrogenation of a nitro group, as opposed to the more typical alkyne/alkene hydrogenation, can be investigated. Typically, platinum-based catalysts are used for this reaction because they are poor at cleaving the chlorine bond.[62–64] More recent works, however, have focussed on improving palladium catalysts for this reaction through the use of alloys or utilisation of different catalyst supports.[61,65–67]

Figure 4.16 shows there is no real difference between the unmodified Pd/C and the borane and sodium borohydride modified samples. Once again, the triacetoxyborohydride modified palladium was by far the least active Pd-$^{\text{interstitial}}$B/C catalyst, as was the butyllithium modified Pd-$^{\text{interstitial}}$Li/C which failed to complete the reaction within two hours. Table 4.6 illustrates the respective performances

Table 4.6: A summary of the *ortho*-chloronitrobenzene hydrogenation products at completion. The overall rate of the reaction is given as R. The unknown (Unk) products are the sum of up to 10 unknown trace products detected by GC.

Catalyst Modifier	**Final Products (%)**					**R (s^{-1})**
	CNB	CAN	AN	NB	Unk.	
Unmodified	0.1	81.0	16.1	0.0	2.8	334
BH_3–THF	< 0.1	85.4	14.1	0.0	0.5	276
$NaBH_4$	< 0.1	78.9	20.2	0.0	0.9	437
$NaBH(OAc)_3$	< 0.1	86.2	13.5	0.0	0.3	165
LiOAc	< 0.1	82.8	16.6	0.0	0.6	430
n-BuLi	55.4	35.8	4.6	2.4	1.7	58

of the boron catalysts in terms of selectivity and overall reaction rate R, with the hydrogen uptake curves shown in Figure 4.17.

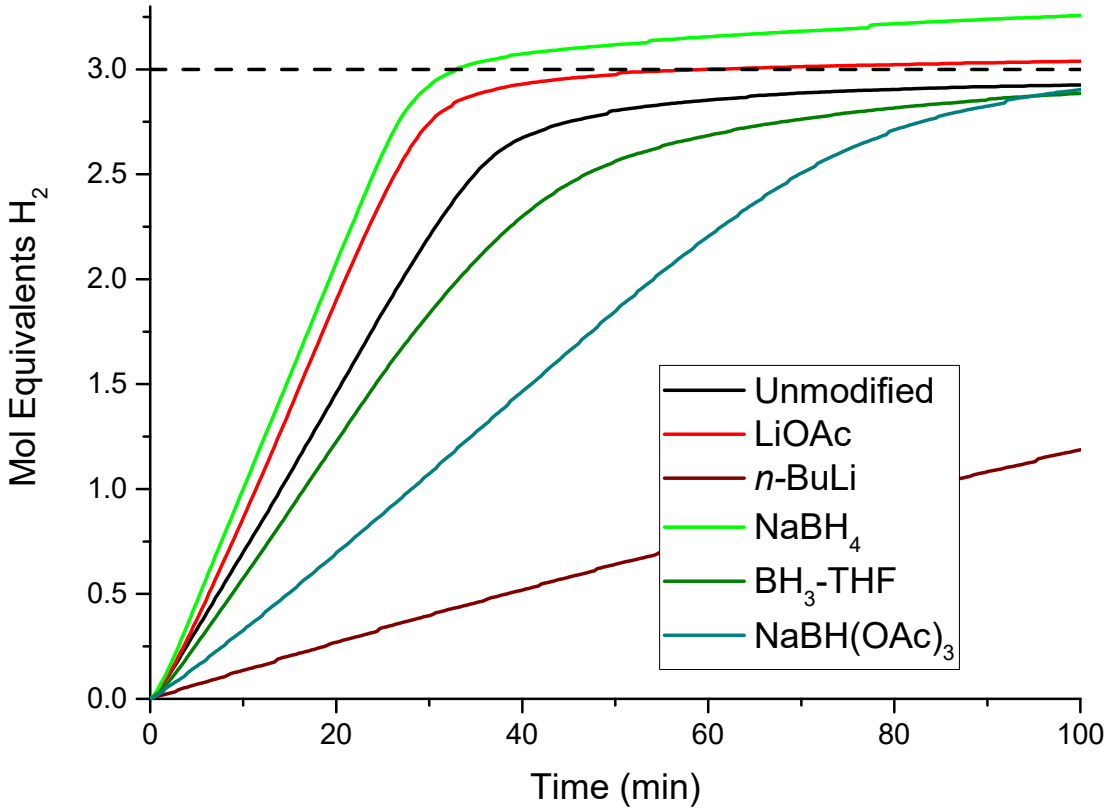

Figure 4.17: The hydrogenation of diphenylacetylene with various catalysts. Conditions: 2.50 mmol alkyne, 3.80 µmol catalyst, in ethanol, 3 bar H_2, 30 °C, 1200 rpm stirrer speed.

Due to the complexity of this reaction (see Figure 4.16) it is only worthwhile

analysing the final products (Table 4.6) along with an overall rate of reaction. The unmodified catalyst has a rate somewhat lower than the most active modified Pd-$^{\text{interstitial}}$B/C and Pd-$^{\text{interstitial}}$Li/C catalysts ($NaBH_4$ and LiOAc) which have rates of $\sim 430\,s^{-1}$. Despite the faster rate for these two catalysts, there was no significant change in the degree of *o*-CAN hydrodechlorination to form aniline (final aniline levels of 14 to 20 %). The borane modified catalyst is slightly better than the rest in this regard, although there is a correlation between the amount of time the catalyst has been at the three-uptake point (total hydrogenation of the nitro group) and level of dechlorination present, suggesting that this is not a fair comparator between catalysts with large differences in completion time, despite use elsewhere.[11] As before, the butyllithium modified catalyst was very poor at this reaction, reacting slowly due to its small surface area being around a tenth of the unmodified catalyst. Despite washing, the butyllithium treatment has most likely altered the catalyst support through the strongly basic nature of the reagent. The effect of this cannot be easily quantified in comparison to the other materials, where the reagents were much milder in comparison.

$NaBH_4$ and $NaBH(OAc)_3$ modifiers will leave traces of Na on the catalyst surface. Sodium can act as a reaction promoter in small quantities (however, with increasing prevalence bond hydrogenation can be supressed).[68,69] The hydrogenation of *ortho*- chloronitrobenzene which is known to be strongly affected by the presence of sodium (and other alkali metals, though not to the same degree) illustrated the effect of increased Na doping.[70] This reaction was the best for the $NaBH_4$ prepared Pd-$^{\text{interstitial}}$B/C, which outperformed the sodium free BH_3-THF modified catalyst, indicating a promotional effect. Both catalysts considerably outperformed the $NaBH(OAc)_3$ modified catalyst, which contained higher levels of sodium. It is known that larger quantities of alkali metals like sodium can supress a catalytic reaction and it appears to have a detrimental effect here.[58,68,69] In the other reactions, where the effect of sodium is lower or not known, the $NaBH_4$ modified catalyst

was second best to the cleaner BH_3-THF prepared material.

4.6.4 3-Hexyn-1-ol Hydrogenation

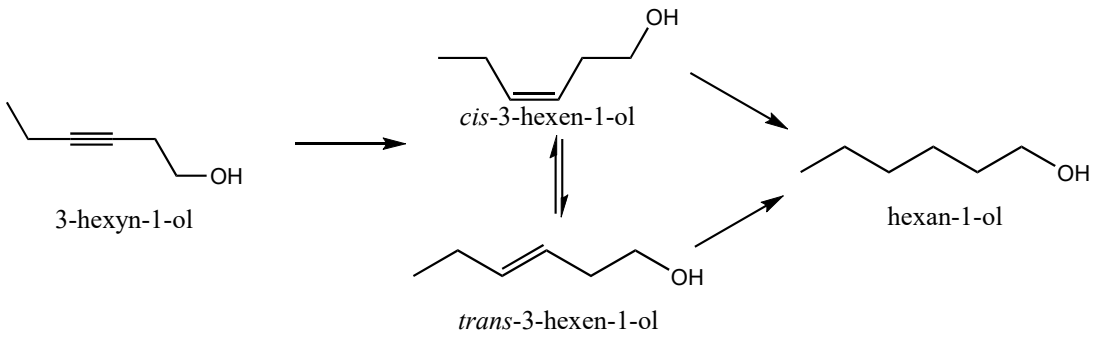

Figure 4.18: A simplified representation of the hydrogenation of 3-hexyn-1-ol, proceeding through both the *cis*- and *trans*- alkene products before finally fully hydrogenating.

The final hydrogenation studied was that of 3-hexyn-1-ol (HYL) (Figure 4.18). The hydrogenation product *cis*-3-hexen-1-ol (*cis*-HEL) is an important chemical in the perfumes industry.[71] Similar to the other alkyne hydrogenations, the reaction was studied under 3 bar hydrogen and run for one hour before the products were analysed by GC. As unmodified palladium can be quite selective for this reaction, all catalysts were held under reaction conditions for some time after the one-uptake point in order to study the degree of isomerisation to *trans*-3-hexen-1-ol (*trans*-HEL) or other bond-shifted products.

These results are summarised in Table 4.7, along with the observed rates, R_1 and R_2. Figure 4.19 displays the hydrogen uptake curves for this reaction. The BuLi modified palladium catalysed reaction was again considerably slower than its counterparts. The $NaBH_4$ modified catalyst displayed poor selectivity during the second stage of the reaction, comparable to that of unmodified Pd/C. There are again very good similarities between LiOAc and BH_3-THF modified catalysts, with the boron modified catalyst displaying slightly better selectivity for the second stage, with lower amounts of isomerisation and bond-shifted products.

Table 4.7: A summary of the 3-hexyn-1-ol hydrogenation products after one hour reaction time. Rates were measured for R_1 after 3 minutes (approximately 5 mL H_2 uptake) into the reaction to remove any activation effects due to the catalyst being partially oxidised and for R_2 after 65 mL of H_2 uptake. The overall rate of the reaction is given as R. The bond-shifted (BS) products are the sum of the trace components detected by GC.

Catalyst Modifier	**Final Products (%)**					**R (s^{-1})**		
	HYL	*cis*-HEL	*trans*-HEL	HAL	BS	R_1	R_2	R_1/R_2
Unmodified	0.1	4.5	20.1	50.4	25.0	442	92	4.8
BH_3-THF	0.1	45.3	21.9	21.2	11.5	392	29	10.6
$NaBH_4$	< 0.1	9.2	25.3	43.7	21.7	380	74	5.1
$NaBH(OAc)_3$	0.1	44.4	22.4	20.5	12.6	321	29	11.0
LiOAc	0.0	30.6	26.7	27.9	14.9	380	38	10.0
n-BuLi	0.0	68.9	12.3	11.5	7.2	164	27	6.2

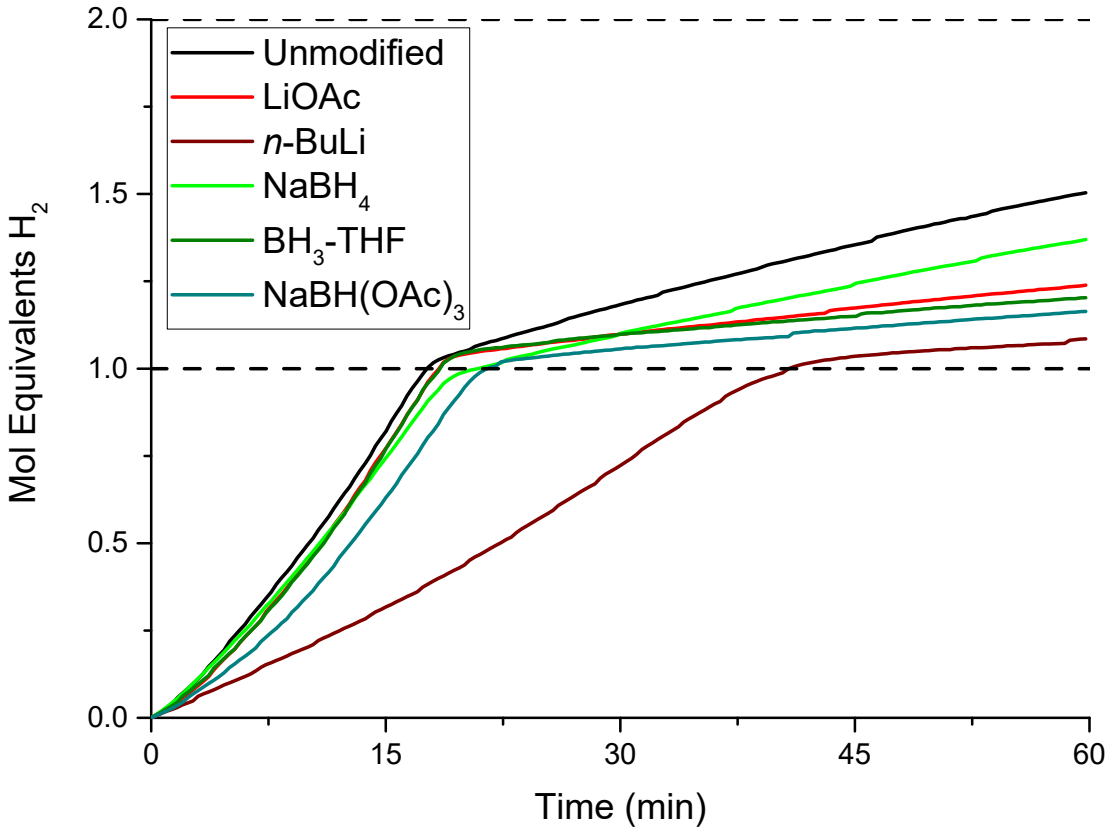

Figure 4.19: The hydrogenation of 3-hexyn-1-ol with various catalysts. Conditions: 2.50 mmol alkyne, 2.50 µmol catalyst, in ethanol, 3 bar H_2, 30 °C, 1200 rpm stirrer speed.

4.7 Conclusions

From the initial characterisation data it is reasonable to assume that all the synthetic routes to interstitial catalysts have successfully doped the palladium nanoparticles, though further characterisation, especially of the novel Pd-$^{\text{interstitial}}$Li/C will follow in Chapter 5.

It is apparent from the initial characterisation of Pd-$^{\text{interstitial}}$B/C that all doping methods lead to the expanded β-palladium boride phase. This coupled with the blockage of the β-hydride is a good indication of boron insertion into the lattice. A simple washing of the sample after synthesis removes a considerable amount of unwanted surface species without compromising the boron doping.

From surface area measurements it was probable that the Pd-$^{\text{interstitial}}$B/C synthesised from $NaBH(OAc)_3$ would be the least active as it has the lowest surface area. This was confirmed by the the catalytic studies. The reduction in surface area is probably due to the large excess of sodium triacetoxyborohydride required to dope the catalyst. Another consideration is the probably relatively large amount of sodium left behind on the surface of the support and catalyst, despite washing. Sodium is known to suppress hydrogenations when present in large amounts.[68] Other carbon fragments from the decomposition of the precursor have deactivated this catalyst relative to the other tested materials.

The $NaBH_4$ doping route gave a catalyst that varied considerably in activity and selectivity depending on the reaction in question, suggesting the presence of low levels of sodium from the doping procedure are influencing each reaction differently. From the characterisation, it is clear that the two-pot approach gives the most consistent catalyst with the one-pot approach having a wide range of particle sizes. Despite this, there is potential to optimise the reaction conditions to allow the production of Pd-$^{\text{interstitial}}$B/C through a completely solvent free method.

The lack of surface sodium in the BH_3-THF modified catalyst, and its superior

activity and selectivity in comparison to the boron catalysts made *via* the grinding techniques, aids it in the reactions studied. For the work shown in later chapters of this thesis, only Pd-$^{\text{interstitial}}$B/C synthesised *via* BH_3-THF will be used as it will be free of any sodium or other contaminants, and is the most consistent performer across the complete range of tested hydrogenations.

With two routes devised to the Pd-$^{\text{interstitial}}$Li/C material, the same preliminary catalytic experiments were undertaken to see how the doping techniques altered the catalyst. To summarise the aforementioned results, both doping techniques create an interstitial lithium catalyst, as seen through the Pd lattice expansion by XRD and the β-hydride elimination by TPR. *In-situ* on the material produced *via* grinding showed clearly the evolution of the expanded palladium lattice with temperature, with Li insertion beginning at at 200 °C with the decomposition of lithium acetate. Similarly Pd-$^{\text{interstitial}}$Li/C's thermal stability in air was evaluated with it stable to approximately 175 °C, similar to the other interstitial catalysts.[8,11]

However, it is clear that the butyllithium approach, unlike the grinding approach, does not produce a viable catalyst. At times the *n*-BuLi produced catalyst was a full order of magnitude less active than the unmodified and lithium acetate modified catalysts. This is most likely caused by the severity of the reagent required to deposit Li into the system. Pd-$^{\text{interstitial}}$Li prepared by this method has a surface area a tenth of that produced *via* the grinding approach. LiOAc gave a much more active catalyst and does not require the use of harsh chemicals in its synthesis, so this Pd-$^{\text{interstitial}}$Li/C catalyst will be used in later chapters. This is the first reported synthesis and investigation into the Pd-$^{\text{interstitial}}$Li/C material.

4.8 References

(1) A. J. McCue, C. J. McRitchie, A. M. Shepherd and J. A. Anderson, *Journal of Catalysis*, 2014, **319**, 127–135.

(2) A. York, *Education in Chemistry*, 2011, **48**, 107.

(3) J. A. McCaulley, *The Journal of Physical Chemistry*, Oct. 1993, **97**, 10372–10379.

(4) M. García-Mota, B. Bridier, J. Pérez-Ramírez and N. López, *Journal of Catalysis*, 2010, **273**, 92–102.

(5) H. L. M. Bakker, M. J. C. de Jong, P. M. Oppeneer, R. Griessen, A. Lodder, R. Vis and H. Brodowsky, *Journal of Physics F: Metal Physics*, 1986, **16**, 707–720.

(6) K. Okitsu, Y. Mizukoshi, H. Bandow, T. A. Yamamoto, Y. Nagata and Y. Maeda, *The Journal of Physical Chemistry B*, 1997, **101**, 5470–5472.

(7) D. Teschner, J. Borsodi, A. Wootsch, Z. Révay, M. Hävecker, A. Knop-Gericke, S. D. Jackson and R. Schlögl, *Science*, May 2008, **320**, 86.

(8) C. W. A. Chan, K. Y. Tam, J. Cookson, P. Bishop and S. C. Tsang, *Catalysis Science & Technology*, 2011, **1**, 1584–1592.

(9) C. W. A. Chan, Y. Xie, N. Cailuo, K. M. K. Yu, J. Cookson, P. Bishop and S. C. Tsang, *Chemical Communications*, July 2011, **47**, 7971–3.

(10) D. Teschner, E. Vass, M. Havecker, S. Zafeiratos, P. Schnorch, H. Sauer, A. Knop-Gericke, R. Schögl, M. Chamam and A. Wootsch, *Journal of Catalysis*, Aug. 2006, **242**, 26–37.

(11) C. W. A. Chan, A. H. Mahadi, M. M.-J. Li, E. C. Corbos, C. Tang, G. Jones, W. C. H. Kuo, J. Cookson, C. M. Brown, P. T. Bishop and S. C. E. Tsang, *Nature Communications*, Jan. 2014, **5**, 5787.

(12) K. D. Allard, T. B. Flanagan and E. Wicke, *The Journal of Physical Chemistry*, 1967, **616**, 298–305.

(13) H. Husemann and H. Brodowsky, *Zeitschrift für Naturforschung A*, 1968, **23A**, 1693.

(14) R. Burch and F. A. Lewis, *Transactions of the Faraday Society*, 1970, **66**, 727–735.

(15) M. Beck, M. Ellner and E. Mittemeijer, *Zeitschrift für Kristallographie*, 2001, **216**, 591–594.

(16) M. Beck, M. Ellner and E. Mittemeijer, *Acta Materialia*, Apr. 2001, **49**, 985–993.

(17) G. Hägg, *Zeitschrift für Physikalische Chemie B*, 1929, **12**, 221.

(18) G. Hägg, *Zeitschrift für Physikalische Chemie B*, 1931, **12**, 33.

(19) Sigma-Aldrich, *Tetrahydrofuran*, Gillingham, UK.

(20) M. Krawczyk, *Applied Surface Science*, 1998, **135**, 209–217.

(21) J.-Y. Wang, Y.-Y. Kang, H. Yang and W.-B. Cai, *The Journal of Physical Chemistry C*, May 2009, **113**, 8366–8372.

(22) T. Nohira, K. Amezawa and Y. Ito, *Journal of Applied Electrochemistry*, 1995, **25**, 48–53.

(23) F. Dalard, M. Ulmann, J. Augustynski and P. Selvam, *Journal of Electroanalytical Chemistry*, 1989, **270**, 445–450.

(24) M. Ulmann, J. Liu, J. Augustynski, F. Meli and L. Schlapbach, *Journal of Electroanalytical Chemistry*, June 1990, **286**, 257–264.

(25) Y. Sakamoto, F. L. Chen, M. Ura and T. B. Flanagan, *Berichte der Bunsengesellschaft für physikalische Chemie*, 1995, **99**, 807–820.

(26) P. Yu, B. S. Haran, J. A. Ritter, R. E. White and B. N. Popov, *Journal of Power Sources*, Dec. 2000, **91**, 107–117.

(27) W. Liu, X. Huang, Z. Wang, H. Li and L. Chen, *Journal of The Electrochemical Society*, 1998, **145**, 80–83.

(28) Y. Idota, T. Kubota, A. Matsufuji, Y. Maekawa and T. Miyasaka, *Science*, 1997, **276**, 1395–1397.

(29) *CRC Handbook of Chemistry and Physics*, ed. R. C. Weast, M. Astle and W. H. Beyer, CRC Press, Boca Raton, Florida, 66th edn., 1986.

(30) Y. Sakamoto, F. L. Chen, J. Muto and T. B. Flanagan, *Zeitschrift für Physikalische Chemie*, Jan. 1991, **173**, 235–250.

(31) A. R. Denton and N. W. Ashcroft, *Physical Review A*, 1991, **43**, 3161–3164.

(32) L. Vegard, *Zeitschrift für Physik*, 1921, **5**, 17–26.

(33) T. B. Flanagan, A. P. Craft, R. Foley, Y. Sakamoto and S. Kishimoto, *Acta Metallurgica*, 1988, **36**, 1791–1796.

(34) C. D. Gelatt, Jr., A. R. Williams and V. L. Moruzzi, *Physical Review B*, 1983, **27**, 2005–2013.

(35) S. A. H. Zaidi, *Applied Catalysis*, 1986, **26**, 155–159.

(36) Y. Lin, K. A. Watson, M. J. Fallbach, S. Ghose, J. G. Smith, D. M. Delozier, W. Cao, R. E. Crooks and J. W. Connell, *ACS Nano*, Apr. 2009, **3**, 871–884.

(37) S. A. Kondrat, G. Shaw, S. J. Freakley, Q. He, J. Hampton, J. K. Edwards, P. J. Miedziak, T. E. Davies, A. F. Carley, S. H. Taylor, C. J. Kiely and G. J. Hutchings, *Chemical Science*, 2012, **3**, 2965–2971.

(38) P. J. Miedziak, S. A. Kondrat, N. Sajjad, G. M. King, M. Douthwaite, G. Shaw, G. L. Brett, J. K. Edwards, D. J. Morgan, G. Hussain and G. J. Hutchings, *Catalysis Science & Technology*, 2013, 2910–2917.

(39) C. Nützenadel, A. Züttel, D. Chartouni, G. Schmid and L. Schlapbach, *The European Physical Journal D*, 2000, **8**, 245–250.

(40) S. A. Kondrat, T. E. Davies, Z. Zu, P. Boldrin, J. K. Bartley, A. F. Carley, S. H. Taylor, M. J. Rosseinsky and G. J. Hutchings, *Journal of Catalysis*, July 2011, **281**, 279–289.

(41) S. V. Pol, V. G. Pol, I. Felner and A. Gedanken, *European Journal of Inorganic Chemistry*, 2007, **2007**, 2089–2096.

(42) J. C. De Jesus, I. González, A. Quevedo and T. Puerta, *Journal of Molecular Catalysis A: Chemical*, 2005, **228**, 283–291.

(43) H. I. Schlesinger, H. C. Brown, B. Abraham, A. C. Bond, N. Davidson, A. E. Finholt, J. R. Gilbreath, H. Hoekstra, L. Horvitz, E. K. Hyde, J. J. Katz, J. Knight, R. A. Lad, D. L. Mayfield, L. Rapp, D. M. Ritter, A. M. Schwartz, I. Sheft, L. D. Tuck and A. O. Walker, *Journal of the American Chemical Society*, 1953, **75**, 186–190.

(44) A. T. Russo, K. L. Amezcua, V. A. Huynh, Z. M. Rousslang and D. B. Cordes, *Tetrahedron Letters*, 2011, **52**, 6823–6826.

(45) A. L. Kolpin, D.Phil. Thesis, University of Oxford, 2014.

(46) J. O. Osby, S. W. Heinzman and B. Ganem, *Journal of the American Chemical Society*, 1986, **108**, 67–72.

(47) K. L. Amezcua, T. J. Mull, A. L. Mayhugh and D. B. Cordes, *International Journal of Undergraduate Research and Creative Activities*, 2015, **7**, Article 5.

(48) M. Beck, Dr. rer. nat. Dissertation, Institut für Metallkunde der Universität Stuttgart, Max-Planck-Institut für Metallforschung Stuttgart, 2001.

(49) M. Yamauchi, R. Ikeda, H. Kitagawa and M. Takata, *The Journal of Physical Chemistry C*, 2008, **112**, 3294–3299.

(50) P. K. Gallagher and M. E. Gross, *Journal of Thermal Analysis*, 1986, **31**, 1231–1241.

(51) R. Lamber, S. Wetjen and N. I. Jaeger, *Physical Review B*, 1995, **51**, 10968.

(52) W. Qi, B. Huang and M. Wang, *Nanoscale Research Letters*, Jan. 2009, **4**, 269–273.

(53) N. Mahata, K. V. Raghavan, V. Vishwanathan and M. A. Keane, *Reaction Kinetics and Catalysis Letters*, 2001, **72**, 297–302.

(54) N. Seriani, *The Journal of Physical Chemistry C*, 2012, **116**, 22974–22979.

(55) Á. Molnár, A. Sárkány and M. Varga, *Journal of Molecular Catalysis A: Chemical*, 2001, **173**, 185–221.

(56) I. T. Caga, E. Shutt and J. Winterbottom, *Journal of Catalysis*, 1976, **44**, 271–280.

(57) M. Krawczyk, J. Sobczak and W. Palczewska, *Catalysis Letters*, 1993, **17**, 21–28.

(58) R. Pellegrini, G. Leofanti, G. Agostini, E. Groppo, M. Rivallan and C. Lamberti, *Langmuir*, 2009, **25**, 6476–6485.

(59) G. Carturan and G. Cocco, *Journal of Molecular Catalysis*, 1984, **26**, 375.

(60) J. G. Ulan and W. F. Maier, *Journal of Molecular Catalysis*, 1989, **54**, 243–261.

(61) H. Liu, M. Liang, C. Xiao, N. Zheng, X. Feng, Y. Liu, J. Xie and Y. Wang, *Journal of Molecular Catalysis A: Chemical*, 2009, **308**, 79–86.

(62) M. Liang, X. Wang, H. Liu, H. Liu and Y. Wang, *Journal of Catalysis*, 2008, **255**, 335–342.

(63) B. Sreedhar, D. K. Devi and D. Yada, *Catalysis Communications*, 2011, **12**, 1009–1014.

(64) K. Xu, Y. Zhang, X. Chen, L. Huang, R. Zhang and J. Huang, *Advanced Synthesis and Catalysis*, 2011, **353**, 1260–1264.

(65) Z. Yu, S. Liao, Y. Xu, B. Yang and D. Yu, *Journal of the Chemical Society, Chemical Communications*, 1995, 1155–1156.

(66) W. Tu, S. Cao, L. Yang and W. Wang, *Chemical Engineering Journal*, 2008, **143**, 244–248.

(67) R. Raja, V. B. Golovko, J. M. Thomas, A. Berenguer-Murcia, W. Zhou, S. Xie and B. F. G. Johnson, *Chemical Communications*, 2005, 2026–2028.

(68) H. B. Cho, J. C. Lee and Y. H. Park, *Catalysis Today*, 2006, **111**, 417–422.

(69) N. Mahata, K. V. Raghavan and V. Vishwanathan, *Applied Catalysis A: General*, 1999, **182**, 183–187.

(70) V. Vishwanathan, V. Jayasri, P. Mahaboob Basha, N. Mahata, L. Sikhwivhilu and N. J. Coville, *Catalysis Communications*, 2008, **9**, 453–458.

(71) J. C. A. A. Roelofs and P. H. Berben, *Chemical Communications*, 2004, **1**, 970–971.

5

In-Depth Characterisation of Novel Interstitial Materials

Contents

5.1 Background

Detailed characterisation of new materials is vital in order to understand the structure, and therefore properties, of said materials.[1] A number of techniques are commonly used to characterise interstitially doped palladium. Two of the simplest, powder XRD and TPR, were covered in the previous Chapter.

Palladium's potential as a hydrogen storage material has resulted in palladium

hydride being the best characterised of the interstitial palladium species.[2–17] It is also the simplest. Earlier studies focussed on the adsorption isotherms and temperature programmed desorption techniques available at the time, which lay the groundwork for the studies that followed. Work in the 1960's by Allard, Flanagan, Bond and others noted the formation of a stable β phase of palladium where the face centred cubic (fcc) structure was retained but the lattice parameter (a_o) of the metal increased from 3.889 to 4.012 Å. This phase change was dependent on the amount of hydrogen located within the palladium lattice, and is a common feature of all palladium interstitial materials.[4,6,8,14,18] Indeed, all the synthesised Pd-$^{\text{interstitial}}$B and Pd-$^{\text{interstitial}}$Li materials within this work have this feature. When the external hydrogen partial pressure rises, causing between 20 to 60 % of the octahedral sites being occupied by the disassociated hydrogen, both the α and β phases co-exist, and cycling between these two phases induces large defects in the palladium that can radically alter the mechanical properties of the material.[8,19]

The majority of analytical techniques rely on inferring the presence of the interstitial dopant as the quantities present – particularly in catalytic materials – are very small. For example, only 15 % of the octahedral sites of palladium in Pd-$^{\text{interstitial}}$C are filled with carbon, and 20 % for Pd-$^{\text{interstitial}}$B.[4,6]

5.2 Objectives

The aim of this chapter is to thoroughly characterise the novel Pd-$^{\text{interstitial}}$Li system through a mix of spectroscopy and microscopy techniques. Where possible the data will be compared to other interstitial palladium systems in the literature or to the Pd-$^{\text{interstitial}}$B made in-house. The wide range of techniques used will give an unparalleled understanding of the Pd-$^{\text{interstitial}}$Li system with conclusions that will be applicable to the other known interstitial systems.

5.3 Particle Size Analysis

An investigation was undertaken how the different dopant techniques affected the particle size of the catalysts. For this analysis all materials were prepared using the same source Pd/C except the one-pot Pd-$^{\text{interstitial}}$B/C where palladium acetate was the precursor. The results are summarised in Table 5.1 and graphically in Figure 5.1.

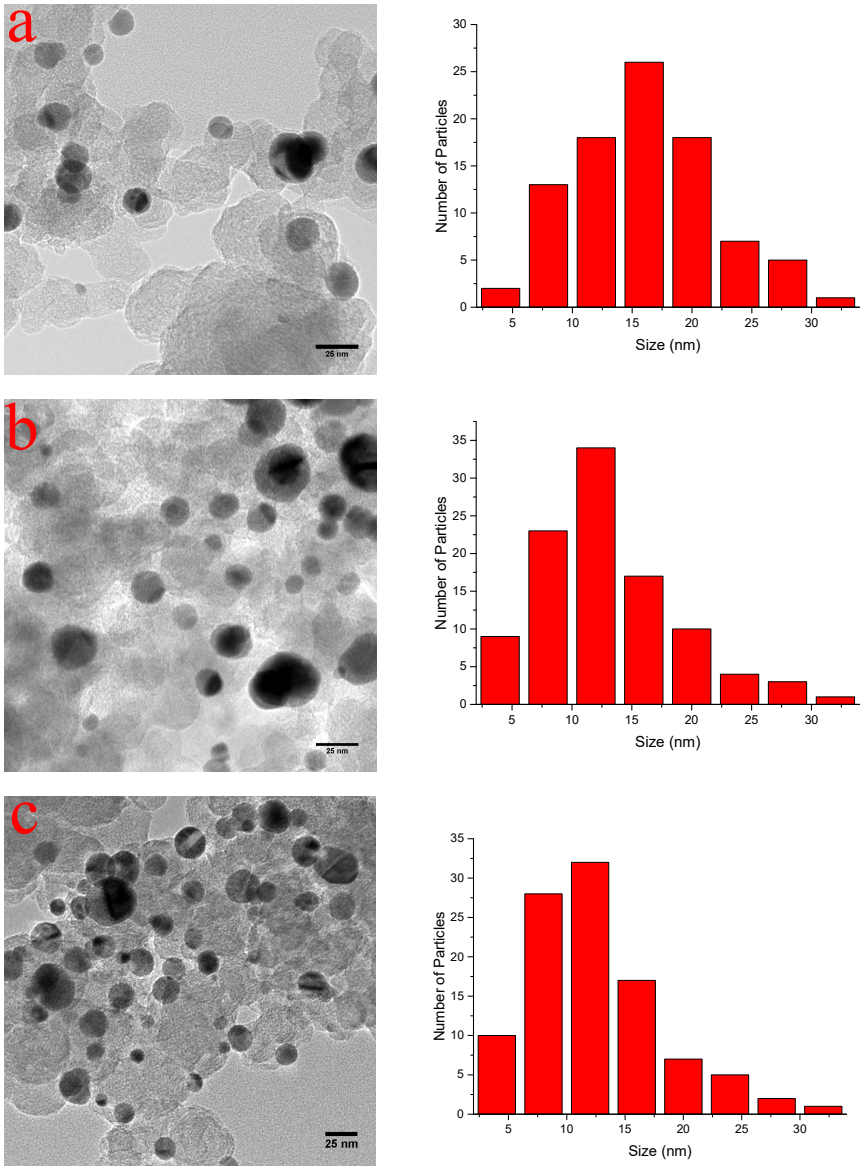

Figure 5.1: A summary of the particle sizes for unmodified Pd/C, Pd-$^{\text{interstitial}}$B/C and Pd-$^{\text{interstitial}}$Li/C

Before modification the particle size was 13.72 nm with a standard deviation

Table 5.1: A summary of the particle sizes of the various interstitial catalysts, a minimum of 100 particles were used in each case.

Catalyst	Particle Size (nm)	Standard Deviation (nm)
Pd/C	13.72	5.73
Pd-$^{\text{interstitial}}$B/C	15.14	5.46
Pd-$^{\text{interstitial}}$Li/C	14.89	5.51

of $\sigma = 5.73\,\text{nm}$. Both boron and lithium modification show a slight increase in particle size from this to 14.50 to 15.20 nm. As this system is outside the region where size effects dominate the activity of a catalyst, it can be assumed that size will not play a major role in further catalytic study.[20]

5.4 X-Ray Photoelectron Spectroscopy

As XPS is a surface sensitive technique (probing the top 2 to 5 nm of a sample's surface), it should be effective for determining the surface elemental composition of the samples. A typical instrument can detect $0.10 \pm 0.01\,\text{atom}\,\%$. For a 5 % weight palladium sample (i.e. $0.1\,\text{mol}\,\%$), the interstitial boron content, with 20 % of the octahedral sites occupied has a maximum bulk value of $0.5\,\text{mol}\,\%$. Boron's relatively poor XPS response factor of 0.486 (compared to Pd 3d response factor of 16), coupled with the small amount of boron within a sample, makes boron particularly hard to detect through this technique. Therefore, the position of the Pd 3d peak is used to see how the doping by boron has influenced the surface electronics of the metal.[21,22] The response factor of Li is much lower again than B, (0.0568) making it almost impossible to detect and again meaning the position of the Pd 3d peak must be used to infer the effects of interstitial modification in both cases.

With this in mind, a 50 % weight loaded Pd/C material was synthesised for lithiation. This was achieved through the grinding of a carbon support with palladium acetate followed by heating to 200 °C in order to decompose the acetate. This method gave a material with particles of mean size = 13.2 nm ($\sigma = 8.50\,\text{nm}$),

Table 5.2: A summary of the observed peaks for the relevant elements in the Pd/C, Pd-$^{\text{interstitial}}$B and Pd-$^{\text{interstitial}}$Li systems. Peaks were corrected to the C 1s peak signal of 284.8 eV in order to account for charging effects.

Sample	**Peak Position (eV)**				
	C 1s	C_xO_y 1s	Pd $3d_{5/2}$	B 1s	Li 1s
5 % Pd/C	284.8	289.1	335.9	—	—
5 % Pd-$^{\text{interstitial}}$B/C (washed)	284.8	289.1	335.6	—	—
5 % Pd-$^{\text{interstitial}}$B/C (unwashed)	284.8	289.4	335.3	193.0	—
5 % Pd-$^{\text{interstitial}}$Li/C (washed)	284.8	290.6	335.7	—	—
5 % Pd-$^{\text{interstitial}}$Li/C (unwashed)	284.8	289.0	336.0	—	—
50 % Pd/C	284.8	289.0	335.8	—	—
50 % Pd-$^{\text{interstitial}}$Li/C	284.8	289.7	336.0	—	—

suitable for doping. The wide particle size distribution can be seen in Figure 5.2. As this material will not be catalytically studied this size distribution is not of major concern, and is to be expected of a highly loaded palladium sample.[23]

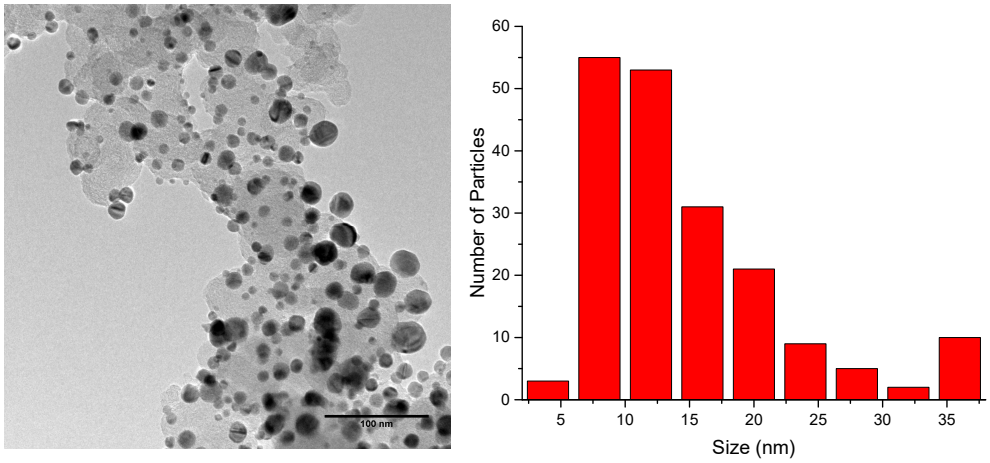

Figure 5.2: A representative TEM image of the 50 % Pd/C sample produced *via* palladium acetate decomposition and a histogram showing the particle size distribution. The particles have a mean size of 13.2 nm with a standard deviation of $\sigma = 8.50$ nm.

Both 50 % and 5 % weight palladium samples were lithiated and compared to unwashed and washed versions of the 5 % Pd-$^{\text{interstitial}}$B/C and Pd-$^{\text{interstitial}}$Li/C catalysts *via* XPS characterisation (Table 5.2).

Of all tested catalysts, only the unwashed 5 % Pd-$^{\text{interstitial}}$B/C catalyst had any amount of detectable dopant. This boron species (binding energy = 193.0 eV)

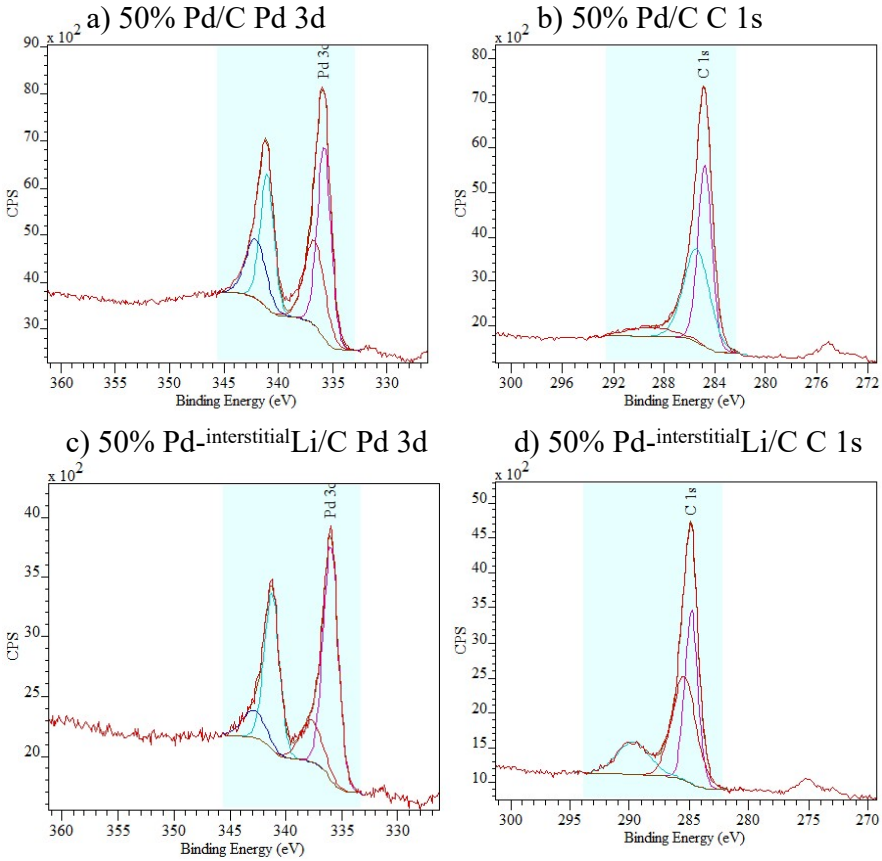

Figure 5.3: Pd 3d and C 1s XPS spectra for 50 % Pd/C (a and b) and 50 % Pd-$^{\text{interstitial}}$Li/C (c and d). Deconvolution of the peaks shows the growth of the carbonate peak in the 50 % Pd-$^{\text{interstitial}}$Li/C sample compared to the unmodified sample, as well as the lack of Pd 3d peak shift between the two samples.

is highly likely to be a boron oxide or boron carbonate species, confirming Chan *et al.*'s observations for this material.[6] The loss of the boron peak after washing supports the hypothesis that these boron species are soluble in water and can be readily removed. The presence of boron in the washed sample can be inferred, if not directly observed, by the growth of carbonate species peak at 289 eV and the large overall increase in surface oxygen as compared to the unmodified Pd/C.[24,25]

As expected, no lithium was detectable in either the 5 % or 50 % samples, likely due to the extremely low response factor lithium has in XPS. For the 50 % Pd-$^{\text{interstitial}}$Li/C sample, observation of lithium was further complicated by the presence of Pd 3p at 55 eV. This is the expected position of Li 1s which is, if at all present,

obscured by it. The peak at this position was small and unable to be deconvoluted to check for separate Li 1s and Pd 3p components due to a poor signal to noise ratio. As with the boron doped catalysts, there is a growth of a carbon peak at ~ 289 eV (Figure 5.3) after treatment with LiOAc. This is indicative of the growth of surface oxygen species, likely in the form of carbonates or oxides caused by the interaction of surface Li with the carbon support.[26]

There are very minor shifts in the Pd 3d peaks for all materials from the unmodified peak position (335.8 eV), however movements of at most 0.6 eV are too small for meaningful conclusions to be drawn as to how the interstitial modification has altered the surface electronics. The electronic effect of the interstitial dopant can be delocalised throughout the entire system (including the bulk), so the net effect at the surface, with only a fraction of the octahedral sites occupied, is expected to be small. This is unfortunately unobservable on our instrument.[6,27]

5.5 Density Functional Theory

DFT was used in order to understand the theoretical contribution of the interstitial dopant to the electronics of a palladium nanoparticle. This work was done in collaboration with Dr Glenn Jones of Johnson Matthey. A palladium fcc (111) surface was constructed with a bulk lattice parameter of $a = 3.89$ Å, consisting of four atomic layers with a vacuum gap of 12 Å. The bottom two layers were frozen and the top layers allowed to relax (Figure 5.4). Two structural models were examined for the interstitial dopant elements (B and Li), one with the dopant placed on the metal surface, the other model with the dopant located in the subsurface.

$$E_{seg} = E_{onsurf} - E_{subsurf} \tag{5.1}$$

The segregation energy (E_{seg}) (as defined in Equation 5.1) can be used to study

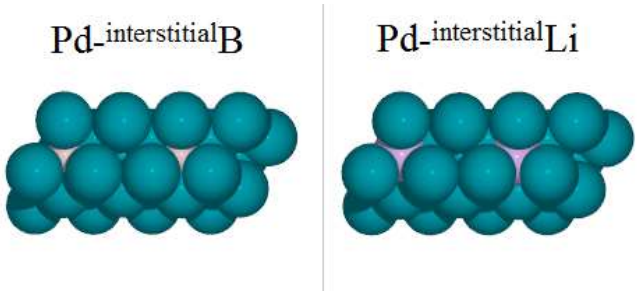

Figure 5.4: Top view of the Pd(111) unit cells after relaxation. Visible within the Pd lattice are B (pink) and Li (purple).

the stability of the interstitial atom by comparing the relaxed energies with the dopant within the lattice ($E_{subsurf}$) to the dopant on the surface (E_{onsurf}). E_{seg} for the Pd-$^{\text{interstitial}}$B system was positive, (+1.4 eV) suggesting that it is more stable than the Pd-$^{\text{interstitial}}$Li system which was found to be metastable ($E_{seg} = -1.85$ eV). From this it would be expected that Pd-$^{\text{interstitial}}$B/C would exhibit greater thermal stability than Pd-$^{\text{interstitial}}$Li/C. This is what was seen experimentally through *in-situ* XRD, where Pd-$^{\text{interstitial}}$Li/C is stable to 150 °C (see Chapter 4) whereas Pd-$^{\text{interstitial}}$B/C is stable in air to 200 °C.[6]

Table 5.3 shows the Bader and d-band analysis on the studied systems. The analyses show the net change in the d band's centre and width is more pronounced than the change in the position of the Fermi level ($\Delta\epsilon_f$).[28] This is small for all systems, corroborating that this effect would be hard to detect through Pd 3d peak shifts observed in XPS. Despite the charged nature of the dopants, it is worth noting that no significant oxidation or reduction of palladium occurred. Bader analysis of the host metal showed a net change of ±0.03 electrons, within error of no net change.

Focussing on the electronic structure of the surface models, with a particular interest on the influence of our dopant and its interaction with the transition metal, the density of states for each system was projected (Figure 5.5).

Figure 5.5 shows that although the d band of the palladium at any one point may have moved after interstitial modification, the lack of change in the DOS integral

Table 5.3: A summary of the d band centre and Bader analyses for the positions of the d band and the charges of the individual dopant elements in the studied systems. All numbers are relative to an unmodified Pd slab and are in eV.

System	d band centre	d band width	$\Delta\epsilon_f$	Bader Charges
Pd-$^{\text{interstitial}}$B	−0.4	+0.1	+0.03	B: +0.4
Pd-$^{\text{interstitial}}$Li	+0.2	−0.2	+0.06	Li: +0.8

shows there is little to no alteration in the position of the Fermi level. Its position has not changed, but the distribution of electron density has. Boron modification has lowered the electron density at the Fermi level, lithium modification has increased it.

Interstitial B shows a marked broadening (the d-band width has increased by 0.1 eV) and lowering (d-band centre has dropped by 0.4 eV) of the d-band centre suggesting a strong overlap of the B p and Pd d bands (Figure 5.5). Most of the electron redistribution comes from the "effective coordination" covalent overlap of the orbitals, rather than addition or subtraction of electrons into the Pd d-band In effect, this overlap with the tail of the d-band counteracts the energy cost of expanding the palladium lattice.[6]

Focussing on the electronic structure of the surface models, with a particular interest on the influence of our dopant and its interaction with the transition metal, the density of states for each system was projected (Figure 5.5).

Figure 5.5a,c shows how the d band of the palladium host has been redistributed after interstitial modification. There is little to no alteration in the position of the Fermi level, however the distribution of electron density has at the Fermi level has. Boron modification has lowered the electron density at the Fermi level, lithium modification has increased the electron density.

Interstitial B shows a marked broadening (the d-band width has increased by 0.1 eV) and lowering (d-band centre has dropped by 0.4 eV) of the d-band centre suggesting a strong overlap of the B p and Pd d bands (Figure 5.5). Most of the electron redistribution comes from the "effective coordination" covalent overlap of

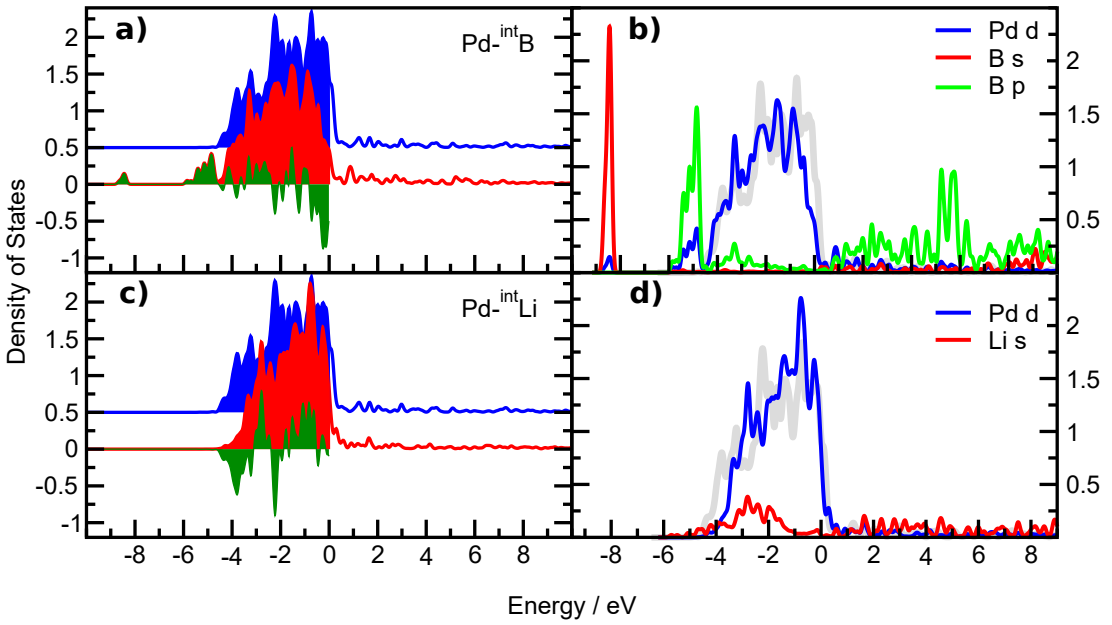

Figure 5.5: Density of states plots for the a) Pd-$^{\text{interstitial}}$B and c) Pd-$^{\text{interstitial}}$Li systems. The blue curve is the DOS of unmodified palladium, red is the DOS of the doped system, green is the change between the two. b) and d) show the relative positions of the Pd 3d, B sp and Li s orbitals for both systems. The overlap between the dopant species' DOS and that of the host palladium is shown. The grey curve represents the Pd d band for the clean surface.

the orbitals, rather than addition or subtraction of electrons into the Pd d-band In effect, this overlap with the tail of the d-band counteracts the energy cost of expanding the palladium lattice.[6]

As expected, we can qualitatively see that lithium modification behaves markedly differently to the boron system. Bader analysis shows that the interstitial lithium has a significantly larger charge suggesting that it is present as an ion. However, it is notable that the compensating negative charge does not result in a localised charge on a neighbouring Pd, the compensating negative charge is instead delocalised across all of the Pd in the system, such that each Pd is effectively charge neutral.

In general, when a light atom is inserted interstitially into a metal lattice the d-band centre will narrow and increase in energy, due to the increased lattice parameter reducing the effective overlap of Pd d orbitals. The fact that lithium has no p-orbitals to interact and stabilise the transition metal d-orbitals causes a narrowing (d-band

width −0.2 eV) and raising of the d-band (d-band centre +0.2 eV) (Table 5.3).

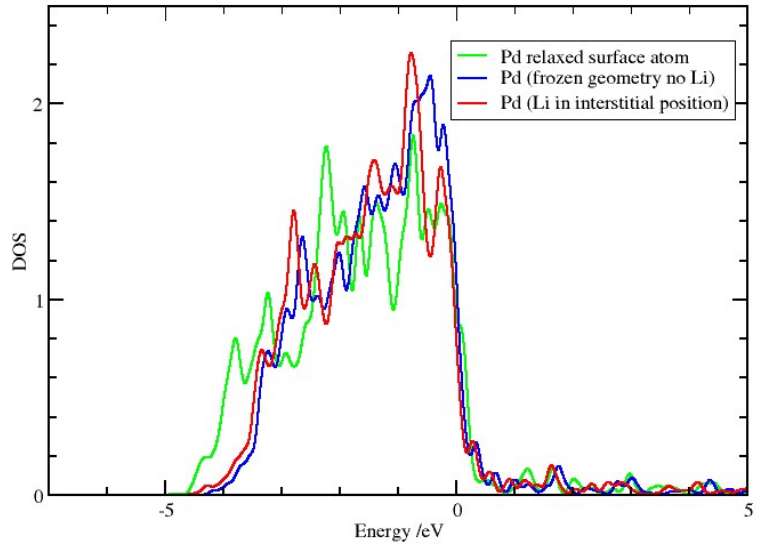

Figure 5.6: Density of states for the Pd surface during Li absorption, green: fully relaxed system with no Li absorbed, red: Li interstitially located, blue the frozen geometry of the Pd-$^{\text{interstitial}}$Li system with the Li removed (as an indicator of the influence of lattice distortion due to Li).

Figure 5.6 depicts the density of states of the d band for: unmodified palladium, the Pd−Li system, and an expanded palladium lattice (the density of states of Pd with the Li atom removed, but the geometry fixed to 3.99 Å). This allows us to separate out the influence of lattice expansion and electronic transfer due to the presence of Li. It can clearly be seen that the majority of the narrowing and broadening of the Pd d-band is a result of the increasing outermost Pd−Pd bond distances. This is caused by the intersititial location of Li; despite this the overall contribution of lithium's orbitals is relatively minor. Indeed, it is possible to view the Pd-$^{\text{interstitial}}$Li system as having "undercoordinated" lithium within the metal lattice. The stabilisation of the lithium within the lattice is not coming from an orbital overlap, but rather a charge-transfer from lithium to the palladium host. Gelatt Jr. and co-workers calculated in 1983 that there would be very little orbital overlap between Li and Pd, but that the system would still be theoretically stable.[29]

To summarise, TPR and XRD (Chapter 4) show the same lattice expansion and

blocking of the interstitial sites observed for hydrogen, indicating the interstitial materials are structurally very similar. The main difference between them is due to how the interstitial atom is affecting the electronics of the system. DFT calculations have shown that the boron modified catalyst will have lowered electron density at the Fermi level relative to the lithium modified catalyst, and therefore this effect will have an impact on how the two materials behave catalytically.

5.6 Solid State NMR

Solid state magic-angle spinning ^{11}B NMR was used to investigate the boron environments both on the carbon support and located interstitially within the palladium nanoparticles. Similarly ^{7}Li NMR was used to investigate the lithium environments. As NMR is tuned to one nucleus at a time (in these cases ^{11}B and ^{7}Li), it is possible to distinguish the different components in a material from their own individual chemical shifts and relaxation parameters. These parameters are dependent on the local environment of the nucleus and can be investigated individually.[30] The experiments were conducted by Thomas Hooper of the Hanna group at the University of Warwick.

5.6.1 ^{11}B MAS NMR

Figure 5.7 shows the presence of two distinct peaks in the ^{11}B MAS NMR of Pd-$^{\text{interstitial}}$B/C at 12.61 ppm and 0.66 ppm. In order to understand the local environment of each peak more fully, a saturation-relaxation experiment was performed. The generated data can be fit in three ways, either with a single-exponential, or if there is more than one component, a multi-exponential or a stretched exponential (Equations 5.2 to 5.4 respectively).[31]

$$I = I_0(1 - e^{(\frac{\tau}{T_1})}) \tag{5.2}$$

$$I = I_0(1 - e^{(\frac{\tau}{T_1})}) + I_0\prime(1 - e^{(\frac{\tau}{T_1\prime})}) \tag{5.3}$$

$$I = I_0(1 - e^{(\frac{\tau}{T_1})})^x \quad 0.6 \leqslant x \leqslant 1 \tag{5.4}$$

Equation 5.2 fits the exponential T_1 relaxation. Equations 5.3 and 5.4 fit the non-exponential T_1 relaxation. Where there is more than one environment, the stretched exponential can be used if there is a distribution of different relaxation rates, as determined by the fitting factor x. This factor needs a value between 0.6 and 1 to be deemed valid. Outside of this range it is unlikely that the non-exponential relaxation is due to inhomogeneously distributed paramagnetic impurities.[31] A multi-exponential fit is used when two different environments in a sample cause identical nuclei to relax at substantially different rates.[31]

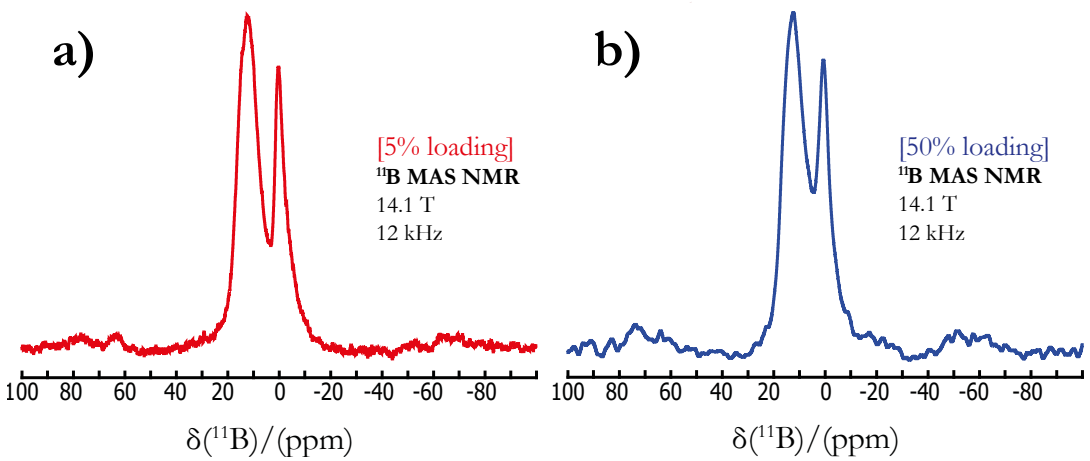

Figure 5.7: ^{11}B MAS NMR for both a) 5 % loaded Pd-$^{\text{interstitial}}$B/C and, b) 50 % Pd-$^{\text{interstitial}}$B/C samples.

Figure 5.8 contains the single-, multi- and stretched exponential fits (summarised in Table 5.4) for the deconvoluted 50 % Pd-$^{\text{interstitial}}$B/C environments. The single exponential successfully fits the environment at 0.66 ppm which is likely due to surface boron species. For the 12.61 ppm environment an exponential fit with more than one term is required. The stretched exponential gives a T_1 value of 0.49 ± 0.10 s,

Table 5.4: A summary of the single-, multi-, and stretched exponential fits to the saturation recovery data for the T_1 relaxation times of ^{11}B in 50 % Pd-$^{\text{interstitial}}$B/C.

Exponential Fit		**^{11}B NMR peak** 12.61 ppm	0.66 ppm
Single	T_1	—	0.64 ± 0.10
Multi	T_1	0.848 ± 0.007	—
	$T_1\prime$	0.003 ± 0.009	—
Stretched	T_1	0.49 ± 0.10	—
	x	0.63 ± 0.03	—

but the fitting factor $x = 0.63 \pm 0.03$, which is on the lower edge of acceptability. It is therefore likely that the multi-exponential determined relaxation times are more reliable. As the multi-exponential relaxation implies different environments we assume one environment to be the interstitially located boron, and the other to be boron on the surface of the nanoparticles. We believe that the ^{11}B $T_1\prime$ relaxation for interstitial boron is much faster than surface boron, i.e. the $T_1\prime$ component of the multi-exponential fit at 12.61 ppm (a relaxation of $T_1\prime$ of 0.003 ± 0.009 s as opposed to the slower T_1 relaxation of 0.848 ± 0.007 s).

This is because boron located within the octahedral site of the palladium can relax in concert with the fast relaxing metal environment.[32] Interestingly, Chan *et al.* saw just one peak in their solid state ^{11}B NMR, which was attributed to interstitial boron. Their system was unwashed so it is much more likely that they have miss-assigned their boron peak to a boron species on the surface of the carbon support.[6]

To study this further, the sample was washed with a dilute 0.1 M HCl solution in order to strip the majority of the boron surface species from the system. This does have the disadvantage of severely depleting both the external surface and interstitial boron content as 29 075 scans were required for the washed sample as opposed to 475 for the unwashed. (Figure 5.9a). Unfortunately, the depletion was to such a degree that a complete saturation-relaxation experiment could not be conducted. However, by varying the recycle delay of the experiment (D1) it is

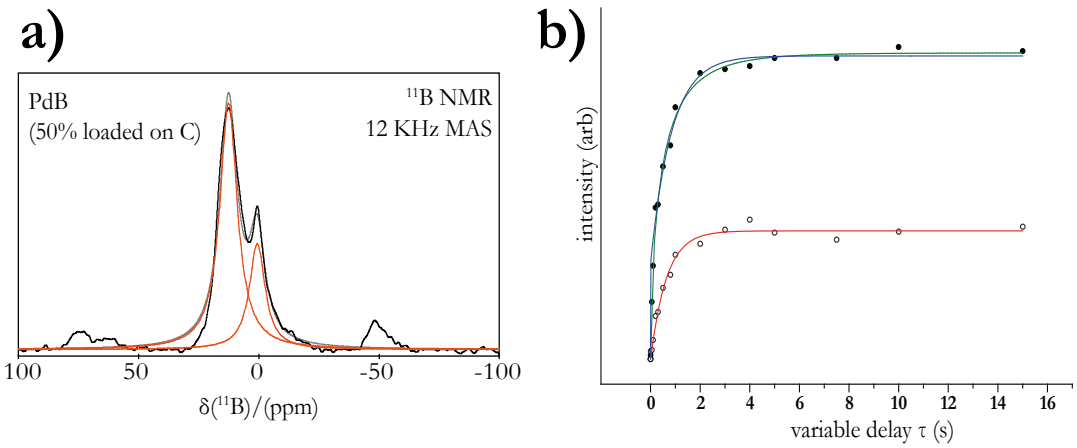

Figure 5.8: a) Deconvolution of the 50 % Pd-$^{\text{interstitial}}$B NMR with b) the saturation-recovery fitting for the T_1 relaxation for the two resolved environments. The red line is the single-exponential fit for the boron environment with a shift of 0.66 ppm (hollow circles). Green and blue lines are the stretched-exponential and multi-exponential fits respectively for the 12.61 ppm boron environment (solid circles).

possible to gain a rough estimation of the T_1 relaxation without doing an in depth T_1 measurement. For maximum signal in an NMR experiment the recycle delay should be above $5 \times T_1$. This ensures the system has time to relax to its equilibrium state before being perturbed and measured again.

As shown in Figure 5.9b, the signal does not increase by increasing the recycled delay from 0.1 to 5 s. This suggests that the T_1 of the components in the washed Pd-$^{\text{interstitial}}$B samples is less than 0.1 s. It does therefore appear that the slow relaxing components have been washed away leaving a fast relaxing interstitial component. However, there is another fast relaxing component present at 2.1 ppm, potentially due to a new boron species forming after the acid treatment like boron chloride on the surface of the metal (Figure 5.9a). This new boron species has a large chemical shift meaning it is unlikely to be the remnant of the 0.66 ppm peak seen prior to acid washing. This, with a caveat on the large amount of uncertainty in the results due to the very poor signal to noise allows a tentative assignment of the fast relaxing component of the unwashed peak at 12.61 ppm to interstitial boron.

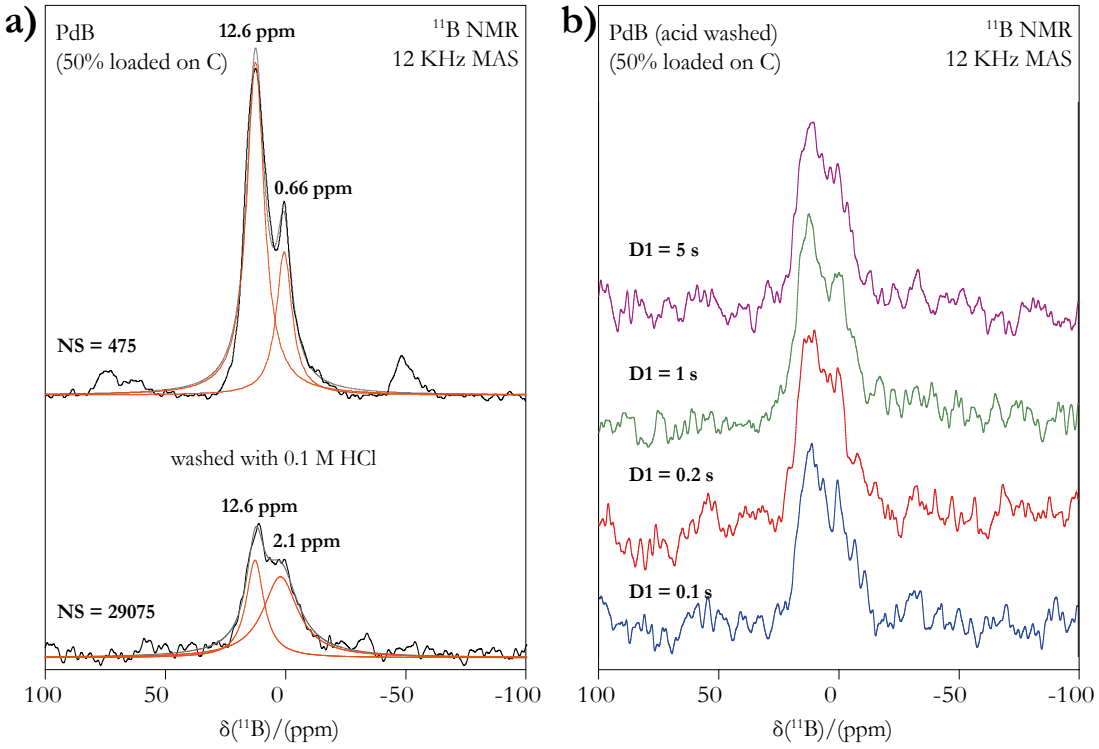

Figure 5.9: a) Signal intensities and positions in ^{11}B NMR before and after acid washing, showing the great reduction in B signal as evidenced by the much higher number of scans (NS). b) D1 delay variation study on acid washed Pd-$^{\text{interstitial}}$B.

5.6.2 ^{7}Li MAS NMR

As with the Pd-$^{\text{interstitial}}$B samples, solid state magic-angle spinning NMR was used to probe the environments of the Li nuclei in Pd-$^{\text{interstitial}}$Li/C. Both the 5 % and 50 % weight loaded samples were synthesised using the same amount of lithium acetate (in large excess). Figure 5.10 shows the much improved signal to noise that arises with more Li in the 50 % Pd-$^{\text{interstitial}}$Li sample, and the stronger magnetic field reducing quadrupolar broadening.[30] The 50 % sample is used for saturation-recovery experiments in order to maximise interstitial lithium content in the sample.

The deconvolution of the ^{7}Li NMR data shows two environments at $\delta = 0.91$ ppm and $\delta = -0.58$ ppm respectively, however the lack of separation makes analysis more difficult. Saturation recovery experiments were performed to determine the nature of the lithium environments. Figure 5.11 contains the deconvoluted 50 %

Table 5.5: A summary of the single-, multi-, and stretched exponential fits to the saturation recovery data for the T_1 relaxation times of ^{7}Li in 50 % Pd-$^{\text{interstitial}}$Li/C.

Exponential Fit		**^{7}Li NMR peak** 0.91 ppm	−0.58 ppm
Single	T_1	40 ± 10	1.7 ± 0.8
Multi	T_1	140 ± 40	70 ± 30
	$T_1\prime$	0.07 ± 0.05	0.006 ± 0.004
Stretched	T_1	1000 ± 1000	1000 ± 3000
	x	0.22 ± 0.03	0.15 ± 0.02

Pd-$^{\text{interstitial}}$Li/C NMR spectrum and the multi- and stretched exponential fits (see Equations 5.3 and 5.4). The results are summarised in Table 5.5.

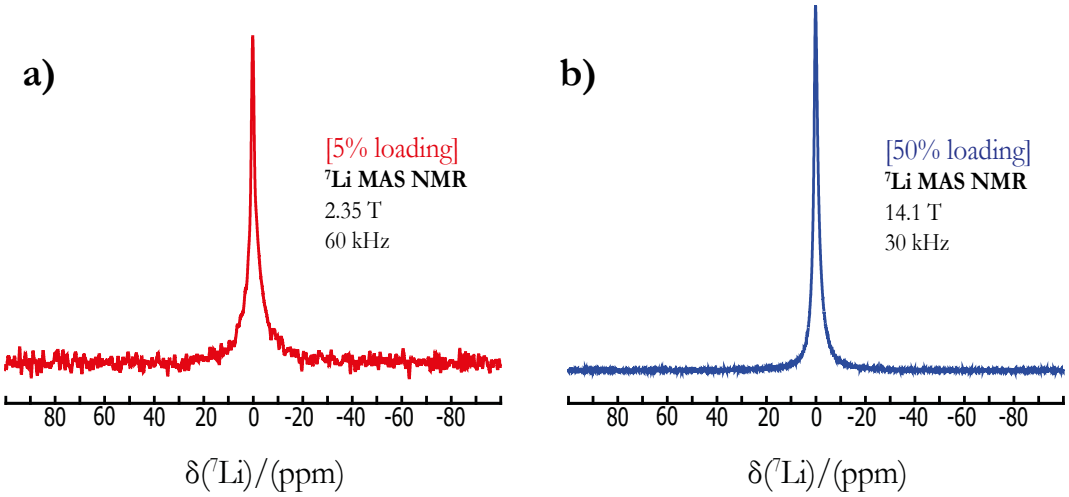

Figure 5.10: ^{7}Li MAS NMR for both a) 5 % loaded Pd-$^{\text{interstitial}}$Li/C and, b) 50 % Pd-$^{\text{interstitial}}$Li/C samples.

Interestingly, a single exponential could not acceptably fit either deconvoluted environment, this would suggest that the spectra contain four different environments of which only two were resolvable due to their very similar chemical shifts. The stretched exponential fits for both environments are much worse than for the boron sample with x values of 0.22 ± 0.03 and 0.15 ± 0.02 for the 0.91 ppm and −0.58 ppm environments respectively. These are far too low to be considered valid.

From the multi-exponential fits of each peak there are slower relaxing lithium environments on the second scale. Present in the −0.58 ppm peak is the fastest

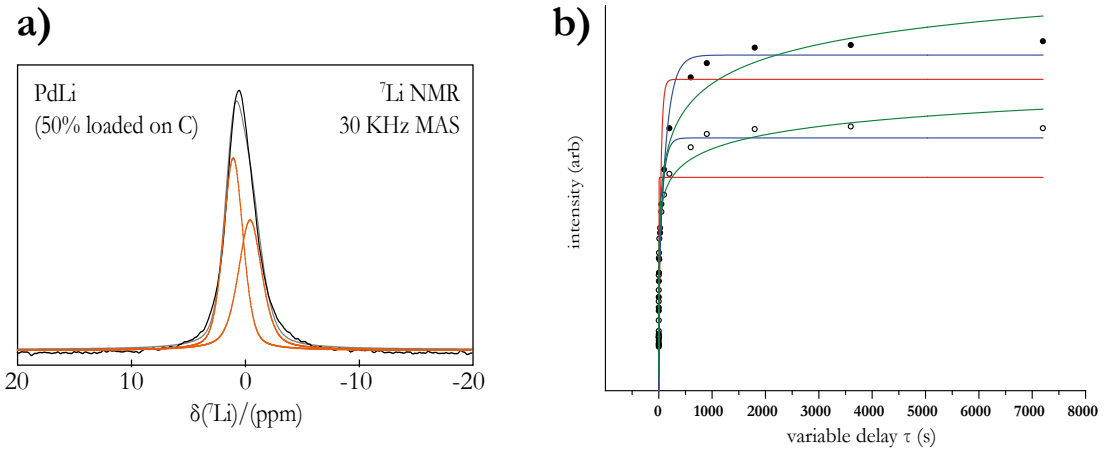

Figure 5.11: a) Deconvolution of the 50 % Pd-$^{\text{interstitial}}$Li/C NMR with b) the saturation-recovery fitting for the T_1 relaxation of the two resolved environments. The green and blue lines are the stretched-exponential and multi-exponential fits respectively for the 0.91 ppm (solid circles) and −0.58 ppm (hollow circles) lithium environments respectively.

relaxing component of 0.006 ± 0.004 s. This is of the same magnitude as the fast relaxing component in the ^{11}B NMR of the Pd-$^{\text{interstitial}}$B system, and an order of magnitude faster than the quickest relaxing component of the 0.91 ppm (0.07 ± 0.05 s. It is likely therefore, there are three surface environments and one interstitial environment. Again, the sample underwent an acid wash with dilute 0.1 M HCl to remove the majority of the surface lithium species (Figure 5.12). This treatment also removed some of the interstitial lithium (the ^{7}Li NMR peak in Figure 5.10 was reduced by approximately 90 %), but unlike the boron system, enough Li remained for a saturation-recovery experiment to be performed. This was also aided by the increased sensitivity of the ^{7}Li nucleus to NMR compared to the ^{11}B nucleus.

None of the exponentials fit the data particularly well due to the poor signal to noise ratio of the sample. There is no real difference in the quality of the fit between the single- and multi- exponentials for the slightly shifted peak at −0.83 ppm, although the stretched exponential has a fitting value of $x = 0.46$, too low to be valid. The results are summarised in Table 5.6.

It is likely therefore that the acid wash has removed the majority, if not all of

Table 5.6: A summary of the single-, multi-, and stretched exponential fits to the saturation recovery data for the T_1 relaxation times of ^{7}Li in acid washed 50 % Pd-$^{\text{interstitial}}$Li/C.

Exponential Fit		**^{7}Li NMR peak** -0.83 ppm
Single	T_1	0.007 ± 0.001
Multi	T_1	0.0014 ± 0.0005
	$T_1\prime$	0.046 ± 0.002
Stretched	T_1	0.012 ± 0.003
	x	0.46 ± 0.06

the surface lithium species, retaining a small quantity of interstitial lithium. This tallies with the observed T_1 relaxation times as determined by the single exponential (0.007 ± 0.001 s) which matches the $T_1\prime$ component of the multi-exponential fit of the -0.58 ppm prior to washing with acid (0.006 ± 0.004 s).

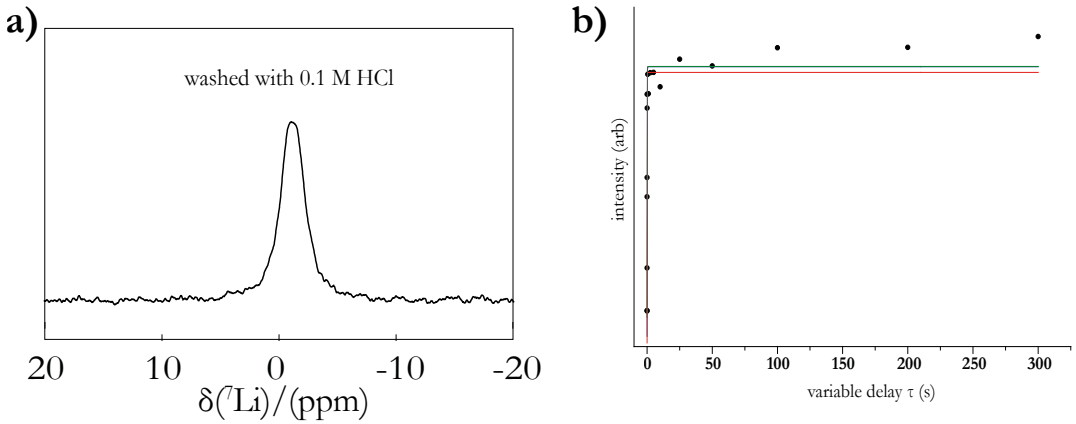

Figure 5.12: a) ^{7}Li MAS NMR on 50 % Pd-$^{\text{interstitial}}$Li washed with 0.1 M HCl. b) The saturation-recovery fitting for the T_1 relaxation for the resolved environments at -0.83 ppm was fit with a single-exponential (red), stretched-exponential (green) and a multi-exponential (blue).

From saturation recovery NMR experiments on both the boron modified and lithium modified systems, it is reasonably certain that the fast relaxing component (on the order of ms) is due to the dopant element being interstitially located. For boron this would be at a chemical shift of 12.61 ppm, and, with more certainty, for lithium at -0.83 ppm.

5.7 SQUID

The effect of the interstitial dopant on the paramagnetism of palladium can be studied by using a superconducting quantum interference device (SQUID). This measures the change in magnetic susceptibility of a sample in an increasing magnetic field. Palladium hydride, as a known interstitial compound, can be used to compare the observed magnetism in the Pd-$^{\text{interstitial}}$B/C and Pd-$^{\text{interstitial}}$Li/C catalysts. It is known that cycling hydrogen in and out of palladium (i.e. forcing the phase transitions α to β to α again) causes a significant number of dislocations in the palladium with incoherent phase boundaries.[33,34] Whilst Pd is saturated with hydrogen, the hydrogen is trapped with an average energy of 0.2 eV and in the deeper dislocations by more than 0.7 eV. Indeed, it is likely that the local concentration of H located at these dislocations is greater than the 70 % of filled octahedral sites seen throughout the bulk.[2,3,35–37] The result is a significant diamagnetic contribution to the paramagnetism of palladium, which has been extrapolated to imply a weak superconducting effect.[19,38]

Figure 5.13 shows how at 300 K the diamagnetism of the carbon support totally obscures the paramagnetism of the palladium. However, at 5 K, the paramagnetism of the palladium dominates.

It is clear that the interstitial doping with boron or lithium has a significant impact on the paramagnetism of the palladium, with boron having a larger dampening effect than lithium. In the case of boron this is possibly due to the lone unpaired B 2p electron countering the induced dipole from within the lattice. As lithium is likely to be ionic (Li^+), it is less able to counter the induced dipole and hence some of the paramagnetic character of the palladium remains. As the two interstitial catalysts behave similarly to the palladium hydride studied in the literature it is a reasonable to conclude that both elements are interstitially located in the palladium lattice.

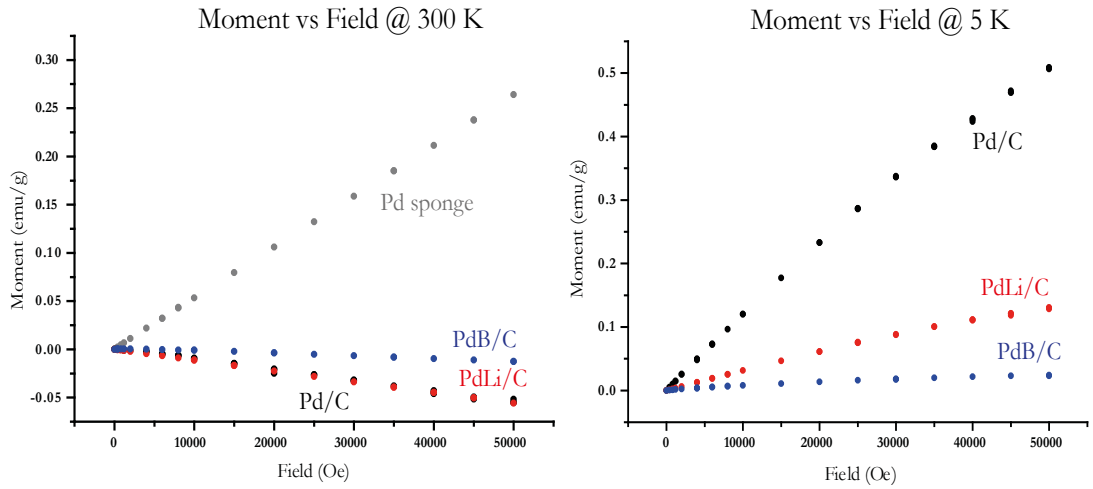

Figure 5.13: SQUID studies on a Pd sponge, Pd/C, Pd-$^{\text{interstitial}}$Li/C and Pd-$^{\text{interstitial}}$B/C at 5 K and 300 K.

5.8 Synchrotron X-Ray Pair Distribution Function

In order to attempt to observe the effect of lithium on the palladium lattice, the I15 Beamline, Diamond Light Source was utilised for X-ray PDF experiments conducted by Ben Lo. Synchrotron generated X-rays have a very short wavelength, $\lambda = 0.163\,14$ Å, and correspondingly large energy (76.0 keV). Using the Rapid Acquisition Pair Distribution Function method it is possible to measure the probablilty of finding two atoms of distance x apart within a sample.[39] A huge advantage with this technique is that crystallinity is not a pre-requisite for evaluating a sample. The lithium within the Pd lattice has no long range order so with this technique, direct observation of the Pd−Li distance should be possible unlike with more traditional X-ray based techniques. The data itself, once corrected for all interferences, normalised, and converted into an integrated one-dimensional pattern from the original two-dimensional source, is shown in Figure 5.14.

The data was refined in PDFgui, in which scale factor, lattice parameters, dampening and broadening factors were set to be refined, with the fit range set to

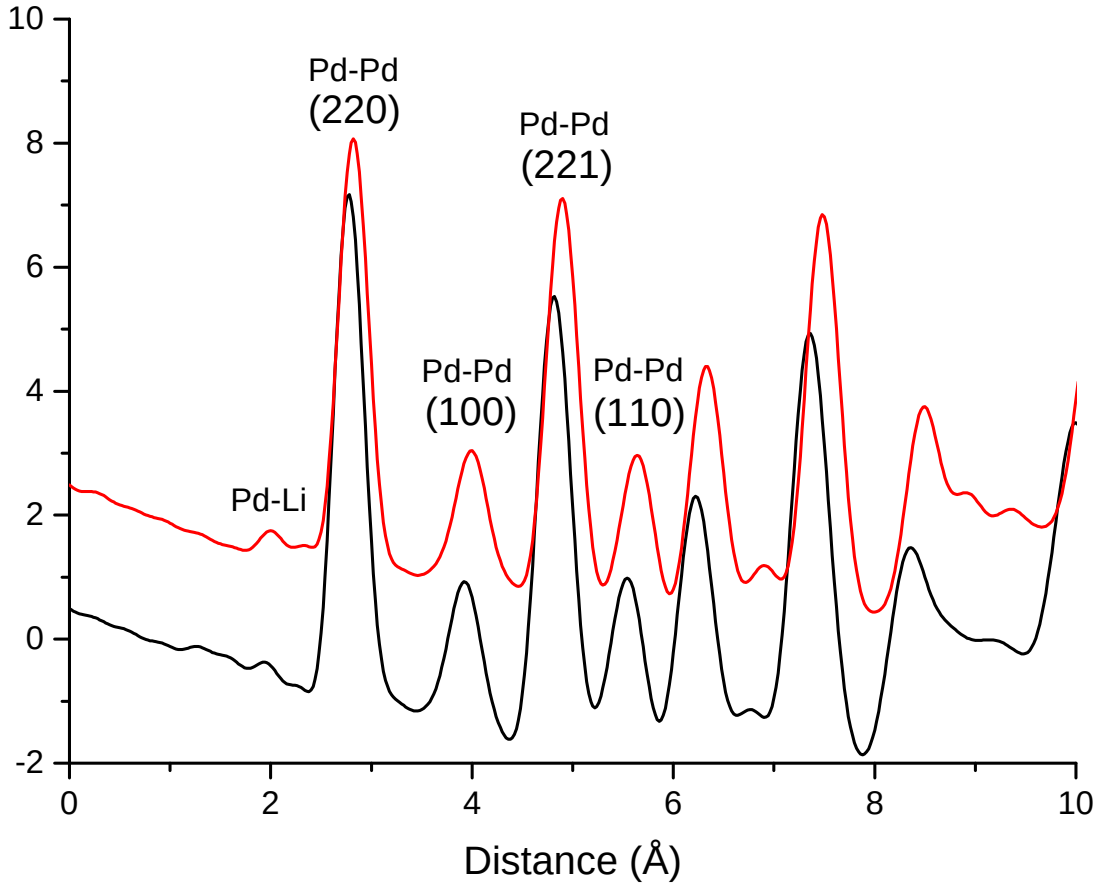

Figure 5.14: PDF patterns of 50 % Pd/C (black) and Pd-$^{\text{interstitial}}$Li/C (red). The positions of the Pd–Pd distances corresponding to the (220), (100), (221) and (110) Miller indicies are highlighted, along with the peak assigned to Pd–Li. The data was collected over the range $0.5 < Q < 50\,\text{Å}^{-1}$. This was corrected for background, Compton and multiple scattering, and beam attenuation by the sample holder interference by the GudrunX package. GudrunX also took the one-dimensional pattern, generated by the DAWN software from the two-dimensional source, and normalised it to the normalised structure factor ($S(Q)$), and hence, by using Keen's method, outputted the PDF as a $d(r)$ function.[40–42]

be from 1.5 to 10 Å.[43] After building a model in PDFgui with lithium occupying a set percentage of the octahedral sites, the best fit was found with 13.7 % of the sites filled with lithium. It is important to note that there is likely a large error in this estimation. With certainty it only possible to say that interstitial site occupation is of the same order as Pd-$^{\text{interstitial}}$C and Pd-$^{\text{interstitial}}$B materials (15 % and 20 % respectively). In corroboration, a theoretical study by Gelatt Jr. *et al.* had proposed that there would be a 0.1 electron transfer from Li to Pd in Pd-$^{\text{interstitial}}$Li, which

would equate to approximately 10 % of the sites filled.[29]

Apparent is the expansion of the palladium lattice from an original 3.9106 to 4.0053 Å. The unmodified 50 % Pd/C sample has a slightly larger lattice parameter than would be expected of bulk palladium (3.89 Å) although 3.91 Å is the maximum lattice parameter of the α phase of palladium.[44] Interestingly, the unmodified Pd/C sample has a small peak in the interstitial position, this is either due to atmospheric oxygen diffusing slowly through the palladium lattice, or some residual carbon fragments from the synthesis which involved the decomposition of palladium acetate. This peak was fit for both elements, and would be equivalent to 1 to 2 % occupancy of the octahedral sites for either.[45,46]

The increased size of the peak attributed to occupation of the octahedral interstitial site coupled with the expanded lattice is a good indication that this peak arises due to interstitial doping, rather than an experimental error arising from truncation ripples.

The observation of octahedral site occupation by lithium is very promising, and it holds that the previous assumptions about lithium occupancy within the palladium lattice were accurate.

This data, and that generated by the other experimental techniques confirm the successful synthesis of the novel Pd-$^{\text{interstitial}}$Li material as well as providing more detailed evidence towards the nature of the Pd-$^{\text{interstitial}}$B catalyst.

5.9 Scanning Transmission Electron Microscopy

It has been widely shown that the intercalation of an interstitial species into the palladium lattice induces large numbers of defects and dislocations in the lattice.[8,34–36] To investigate how doping the palladium nanoparticles with boron or lithium has affected the host lattice, scanning transmission electron microscopy (STEM) was used in three modes. The first of which, annular bright-field (ABF), is

particularly useful in imaging the graphitic sheets of the carbon support. Atoms shown through this detector angle are dark in comparison to the background. The remaining two modes were low-angle annular dark-field (LAADF) from which particle strain information can be derived, and finally medium-angle annular dark-field (MAADF), ideal for density information. For both of these, the light areas are caused by electron scattering by the atomic columns. All images used a 50 % weight loaded sample.

5.9.1 Pd-$^{\text{interstitial}}$Li/C STEM

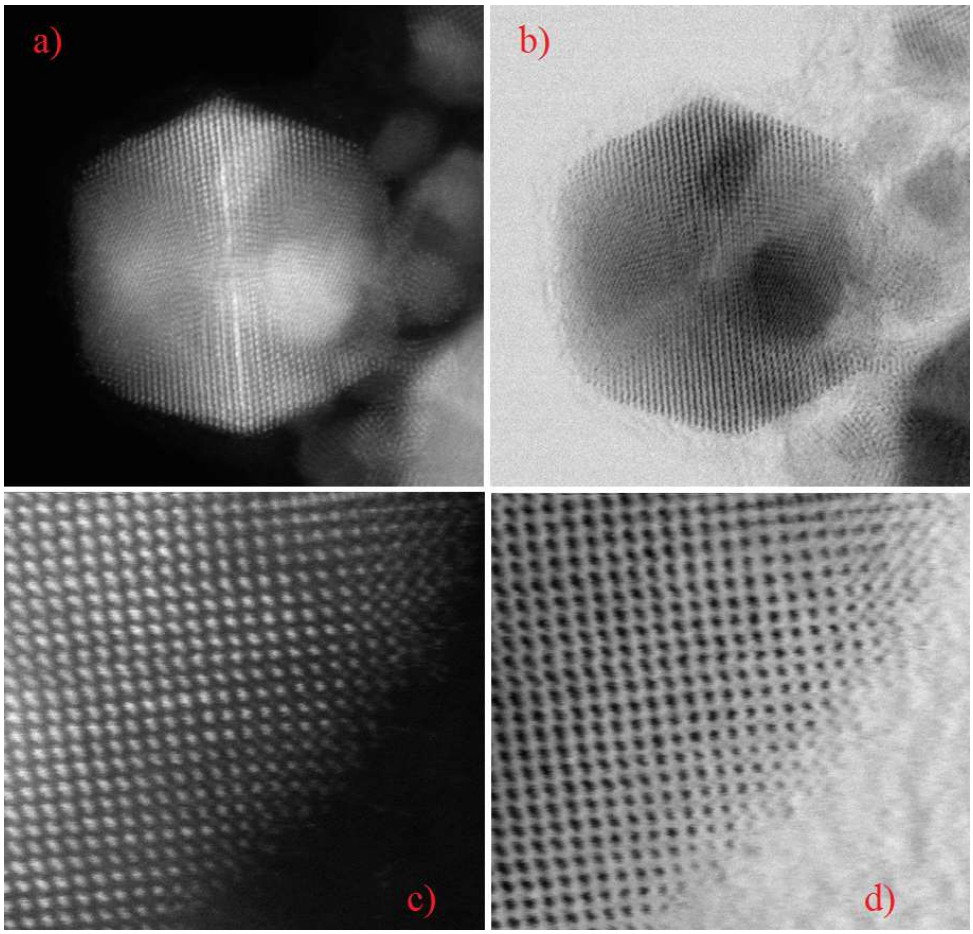

Figure 5.15: Pd-$^{\text{interstitial}}$Li/C STEM images of a particle in a) MAADF, b) in ABF. The view area width for both a) and b) is 25 nm. The corresponding edges of another particle are in c) MAADF and d) ABF. The view area width for both a) and b) is 8 nm.

The Pd-^{interstitial}Li/C system was investigated using MAADF and ABF (Figure 5.15) and there is a large amount of five-fold particle twinning present. This is a feature arising from alternate co-planar twin planes. They are enclosing an angle of about 0.4π rad and are typical of fcc materials and are inherently metastable.[47] The particle itself has an area of increased mass-thickness (the bright spot in Figure 5.15a) which is most likely due to another smaller nanoparticle located underneath the larger main particle.

Focussing on the edge images (Figure 5.15c, d) the fcc structure of the palladium lattice is clear, albeit with signs of dislocations commonly caused by interstitial modification.

5.9.2 Pd-^{interstitial}B/C STEM

Figure 5.16a highlights another multiply twinned palladium nanoparticle, this one modified with boron. The particle has undergone significant structural reconstructions in order to try to lower the surface energy of the particle.

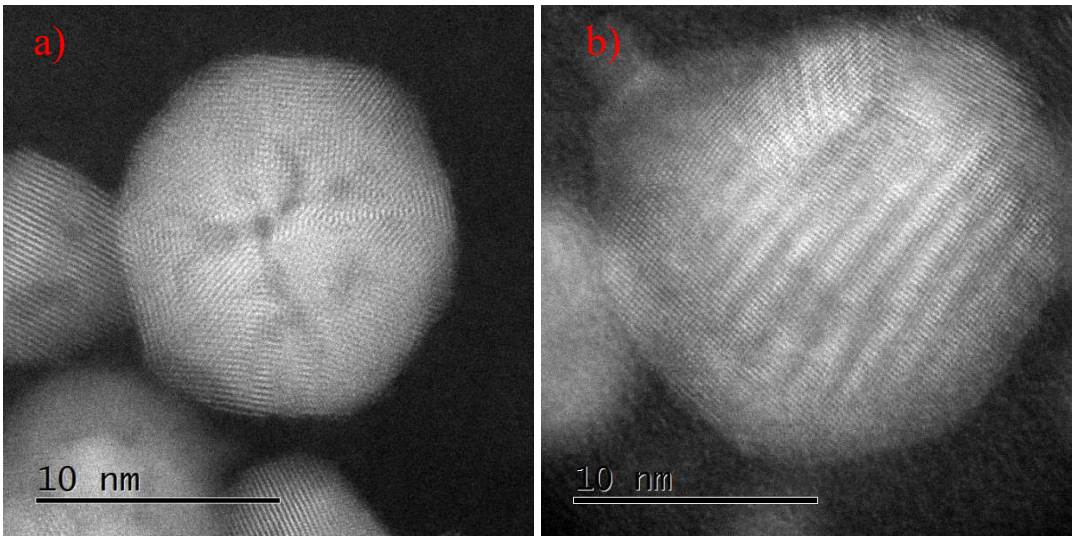

Figure 5.16: a) Pd-^{interstitial}B/C MAADF-STEM image of a particle showing five-fold twinning and a large number of lattice defects, b) Pd-^{interstitial}B/C LAADF-STEM image of an untwinned particle. The 'ripples' are a strong indication of high lattice strain.

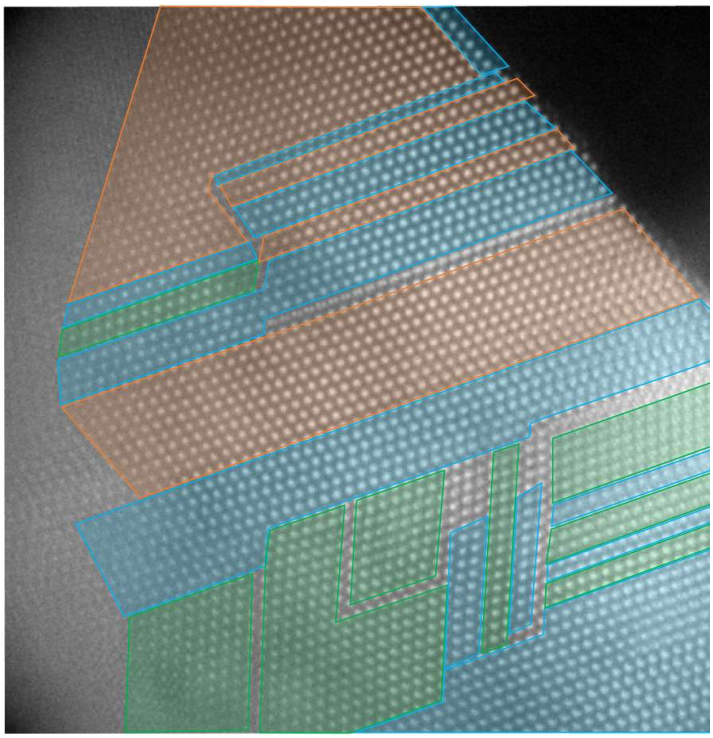

Figure 5.17: A colourised image of the phase transition in a Pd-$^{\text{interstitial}}$B/C nanoparticle. The areas orange and green correspond to an fcc lattice structure, and blue a hcp structure

Taking the untwinned particle (Figure 5.16b) the strain induced by boron modification is shown by the rippling effect over the surface of the particle. Indeed, the extent of the surface rearrangement becomes clear when we focus on the edge of the particle in Figure 5.16a.

Figure 5.17 shows the extent of the reconstruction; palladium, a well-known fcc structured material has in some regions converted to a hcp structure. Palladium possessing an hcp atom arrangement is a particularly uncommon material. It has been seen before but only through templating the growth of a Pd nanoparticle on a hcp support such as Nb, W or graphite.[48–51] Some computational work on hcp palladium has focussed on its potential effect on the magnetism of the palladium or as a potential surface site for acetylene adsorption.[48] Here however, the hcp site is caused by a step through the crystal rather than a major reconstruction.[52,53]

Maxelon *et al.* has shown that, in a PdH system, hydrogen concentrates at

the locations of the induced dislocations.[35] DFT calculations by Yoo *et al.* have shown that boron will adsorb most strongly on the hcp site in palladium, similar to what has been seen for hydrogen.[54] Hydrogen has much greater mobility in the lattice than boron due to its size so it is easier for hydrogen to concentrate in one area. However, it is possible for there to be higher boron concentration at the hcp sites than elsewhere within the particle, as boron is likely necessary to stabilise the observed fcc to hcp transition. As lithium content within a palladium nanoparticle is lower there appears to be a smaller degree of rearrangement relative to boron modification. The greater rearrangement may also be due to the much stronger orbital interactions between the B sp and Pd d bands as shown by DFT.

5.9.3 Smart Aligned STEM for Pd-$^{\text{interstitial}}$B/C

STEM imaging can cause particles to drift as the microscope's electron beam is focussed upon them, lowering the quality of the resulting image. However, taking several images in quick succession and using the recently developed Smart Align algorithm by Jones *et al.* can reconstruct a very high quality image by correcting these non-rigid distortions.[55] Using this image correction technique, it is possible to see great detail in a nanoparticle. Indeed, in an ideal single-crystal of palladium it is possible to see between the columns of palladium atoms. Unfortunately, interstitial boron cannot be directly visualised by this technique due to the huge mass difference between Pd and B, leading to the contrast being dominated by the palladium.

This can be seen in Figure 5.18 where new columns of Pd atoms can be seen starting inside the nanoparticle, dislocated from their original position by interstitial modification.

Figure 5.19 shows an aberration corrected Pd-$^{\text{interstitial}}$B/C nanoparticle. The MAADF image gives information about the density of the particle, which as expected appears brighter in the centre compared to the outer edges. Looking at the LAADF

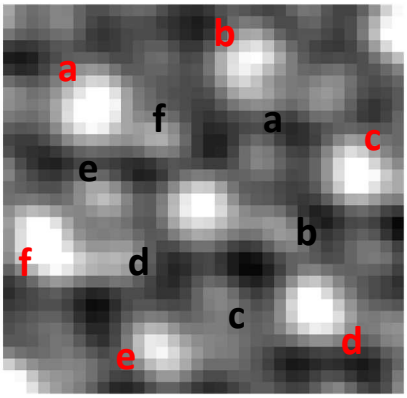

Figure 5.18: a-f in black are the tops of new columns of palladium atoms several layers into a particle. They are dislocated from the surface columns (a-f in red) by interstitial modification.

image, a bright central band becomes apparent caused by the twinning in the particle. It is so much brighter because the face visible is preferentially orientated towards the detector. Some strain information is also visible at this detector angle, notably the brighter ring around the outer edge of the particle. MAADF shows there is no increased density at the outer edge and therefore this can be ascribed to greater strain around the outside of the particle caused by boron doping. The ABF image shows good detail about the nature of the support, the graphitic layers visible along with the twinned nature of the particle. Detailed elemental mapping of a Pd-$^{\text{interstitial}}$B/C will be able to confirm the cause of the apparent strain

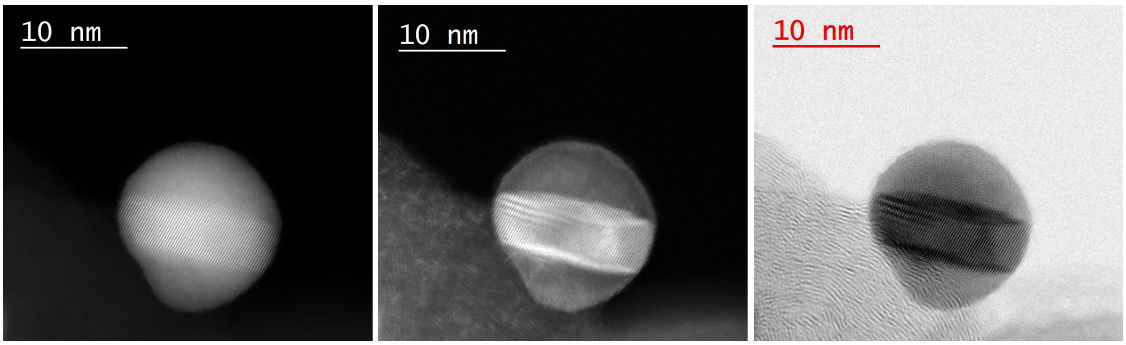

Figure 5.19: A Pd-$^{\text{interstitial}}$B/C particle imaged by (from left to right) MAADF-STEM, LAADF-STEM and ABF-STEM and image corrected by the Smart Align algorithm.[55]

5.10 Electron Energy Loss Spectroscopy

In order to map the boron content within a palladium nanoparticle, electron energy loss spectroscopy (EELS) was undertaken. The inelastic interaction of electrons from the electron beam with the electron shells of atoms in its path gives rise to characteristic edges (Figure 5.20). Only the boron modified material could be analysed by EELS as lithium, which has a poor response factor anyway, has its K edge obscured by that of the palladium N edge.

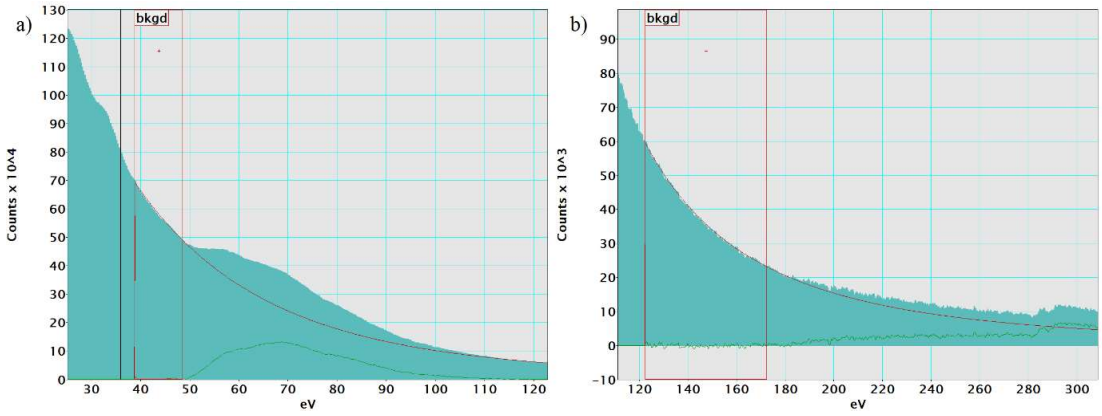

Figure 5.20: EELS spectra for a Pd-$^{\text{interstitial}}$B/C nanoparticle. The Pd N edge is apparent at 51 eV in a) as evidenced by the spectrum rising above the red baseline, the difference between the theoretical baseline and the actual spectrum is the green line. The B K edge is present at 188 eV in b) with a slight lift from the baseline. The peak at 284 eV in b) is due to the carbon K edge from the support.

The electron beam detects a considerable presence of Pd, as expected, with the N edge shown in Figure 5.20a at 51 eV.[56] Similarly, a small amount of boron is detected (Figure 5.19b) as the beam is scanned over the particle, with B's K edge at 188 eV. The carbon support can be seen with a K edge of 284 eV. From this it is possible to build up a compositional map detailing the location of the palladium and boron atoms within a particle.

Figure 5.21 shows how this compositional data can be mapped. It is important to note that this is a two-dimensional representation of a three-dimensional particle and each point is the average signal of the beam passing through the particle. The

palladium map shows a higher concentration of Pd in the centre of the particle, whereas the boron map has a higher relative concentration around the edges of the particle. This matches with what was observed in terms of particle strain in the LAADF images (Figure 5.19). The false-coloured image of the Pd-$^{\text{interstitial}}$B/C nanoparticle in Figure 5.21 is graphically represented in Figure 5.22.

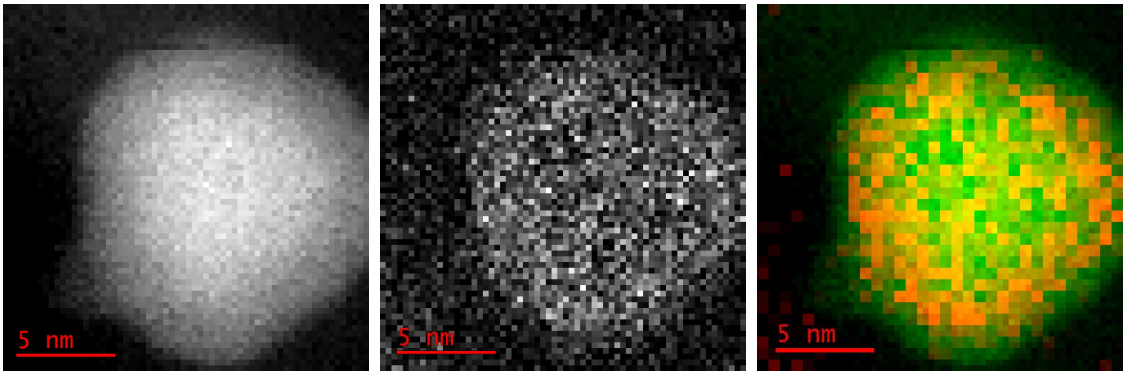

Figure 5.21: Compositional maps of a Pd-$^{\text{interstitial}}$B/C particle. From left to right, Pd compositional map, the boron compositional map and a false-coloured combined map. Green are palladium atoms, orange are boron.

The fact the boron density is not uniform with palladium density suggests there is a concentration gradient of boron through the particle with the majority located in the upper layers. This makes sense from a synthetic point of view with the palladium particle existing prior to boron modification. The movement of boron within the particle will be slow considering the size of the boron atom. This is the closest to direct visualisation of boron within the palladium lattice reported so far. Indeed, these results plus the evident strain in the LAADF-STEM (Figure 5.19) allows the conclusion that boron has penetrated to a depth of at least 3 to 4 nm (3 atomic layers). It is likely boron is deeper within the lattice but that there is a decreasing concentration of boron further into the particle. During the synthesis of these particles perhaps holding the material for a longer time at 200 °C, or using more of the boron precursor will drive it deeper into the lattice.

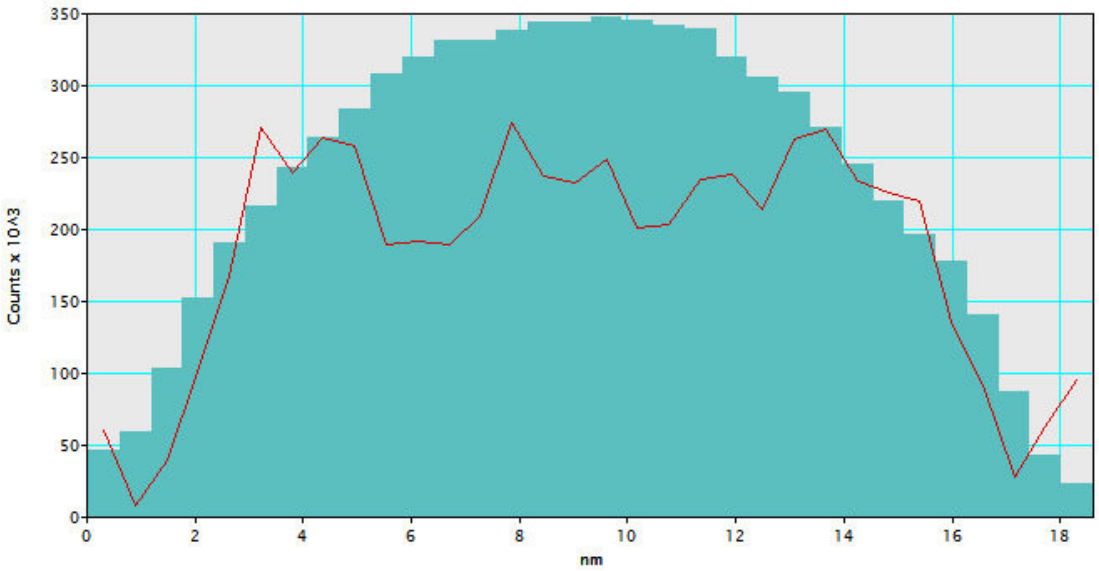

Figure 5.22: A graphical representation of the elemental composition of a Pd-$^{\text{interstitial}}$B/C particle. The green bars refer to palladium concentration within the particle. The red line refers to boron concentration within the particle. The boron signal has been multiplied 30× to aid clarity.

5.11 Conclusions

In conclusion, the novel material, Pd-$^{\text{interstitial}}$Li/C has been fully characterised using a range of techniques, building upon the simple techniques discussed in Chapter 4. This has been coupled with computational analysis to strongly conclude that the lithium is indeed interstitially located within the palladium lattice.

Results of interest include the solid state NMR, which confirmed the presence of Li and B within the palladium lattice that was not detectable by XPS after sample cleaning. The NMR also showed several other environments present that, in addition to the interstitial element, there are still unwanted boron and lithium species remaining upon the surface of the support, despite the cleaning. The maximum boron loading within a Pd nanoparticle has been known for many years, however the lithium modified species had not been quantified prior to this work. PDF has allowed a tentative estimate of the maximum interstitial doping of a palladium lattice by Li at 13.7 % of the octahedral sites, though this value will

have a significant error, it is the first attempt to quantify the maximum amount of Li able to be present within a palladium nanoparticle.

STEM allows the effect of doping upon the structure of the host Pd particles to be observed. This is beyond the bulk information that was gained through the use of the X-ray techniques (e.g. the lattice expansion seen through XRD). There are a large number of induced defects in the host palladium particle that are attributable to interstitial modification, similar dislocations have been observed in palladium hydride materials. The action of inserting the dopant atom into the lattice is balanced energetically by surface reconstructions. This was most clearly seen with the structural transformation of the palladium fcc surface to hcp in places by boron insertion. EELS provided the most direct visualisation of boron within the palladium lattice to date, showing the boron has concentrated in the top few layers of the nanoparticles.

DFT studies of the interstitial systems have shown the interactions between the orbitals of the dopant and the palladium. The effects of this interaction (boron reducing electron density at the Fermi level and lithium increasing it) will alter the catalytic properties of the Pd nanoparticles. This will be explored further in Chapter 6 where a variety of media and conditions will be studied.

5.12 References

(1) *Encyclopedia of Materials Characterization*, ed. C. R. Brundle, C. A. Evans, Jr. and S. Wilson, Butterworth-Heinemann, Greenwich, Connecticut, 1992.

(2) A. G. Lipson, B. J. Heuser, C. H. Castano and A. Celik-Aktas, *Physics Letters, Section A: General, Atomic and Solid State Physics*, 2005, **339**, 414–423.

(3) A. G. Lipson, B. J. Heuser, C. H. Castano, B. F. Lyakhov and A. Y. Tsivadze, *Journal of Experimental and Theoretical Physics*, 2006, **103**, 385–397.

(4) C. W. A. Chan, K. Y. Tam, J. Cookson, P. Bishop and S. C. Tsang, *Catalysis Science & Technology*, 2011, **1**, 1584–1592.

(5) C. W. A. Chan, Y. Xie, N. Cailuo, K. M. K. Yu, J. Cookson, P. Bishop and S. C. Tsang, *Chemical Communications*, July 2011, **47**, 7971–3.

(6) C. W. A. Chan, A. H. Mahadi, M. M.-J. Li, E. C. Corbos, C. Tang, G. Jones, W. C. H. Kuo, J. Cookson, C. M. Brown, P. T. Bishop and S. C. E. Tsang, *Nature Communications*, Jan. 2014, **5**, 5787.

(7) J. A. McCaulley, *The Journal of Physical Chemistry*, Oct. 1993, **97**, 10372–10379.

(8) T. B. Flanagan and W. A. Oates, *Annual Review of Materials Science*, 1991, **21**, 269–304.

(9) Y. Sakamoto, F. L. Chen, M. Ura and T. B. Flanagan, *Berichte der Bunsengesellschaft für physikalische Chemie*, 1995, **99**, 807–820.

(10) K. D. Allard, T. B. Flanagan and E. Wicke, *The Journal of Physical Chemistry*, 1967, **616**, 298–305.

(11) M. Yamauchi, R. Ikeda, H. Kitagawa and M. Takata, *The Journal of Physical Chemistry C*, 2008, **112**, 3294–3299.

(12) G. J. Thomas and J. M. Mintz, *Journal of Nuclear Materials*, 1983, **116**, 336–338.

(13) V. F. Rybalko, A. N. Morozov, I. M. Neklyudov and V. G. Kulish, *Physics Letters A*, 2001, **287**, 175–182.

(14) A. Maeland and T. B. Flanagan, *The Journal of Physical Chemistry*, 1960, **68**, 1419–1426.

(15) S. Kishore, J. Nelson, J. Adair and P. Eklund, *Journal of Alloys and Compounds*, Mar. 2005, **389**, 234–242.

(16) T. B. Flanagan, A. P. Craft, R. Foley, Y. Sakamoto and S. Kishimoto, *Acta Metallurgica*, 1988, **36**, 1791–1796.

(17) M. C. Cadeville and C. Lerner, *Philosophical Magazine*, May 1976, **33**, 801–824.

(18) M. Beck, Dr. rer. nat. Dissertation, Institut für Metallkunde der Universität Stuttgart, Max-Planck-Institut für Metallforschung Stuttgart, 2001.

(19) M. Suzuki, I. S. Suzuki and J. Walter, *J. Phys: Condens. Matter*, 2004, **16**, 903–918.

(20) *Nanocatalysis*, ed. U. Heiz and U. Landman, Springer, Berlin, 2007.

(21) *Handbook of Analytical Techniques*, ed. H. Günzler and A. Williams, Wiley-VCH Verlag GmbH & Co. KGaA, Weinheim, Germany, 2nd edn., 2002.

(22) *Surface Analysis – The Principal Techniques*, ed. J. C. Vickerman and I. S. Gilmore, John Wiley and Sons, Ltd, Chichester, 2nd edn., 2009.

(23) Y. Lin, K. A. Watson, M. J. Fallbach, S. Ghose, J. G. Smith, D. M. Delozier, W. Cao, R. E. Crooks and J. W. Connell, *ACS Nano*, Apr. 2009, **3**, 871–884.

(24) C. Vincent, H. Vincent, H. Mourichoux and J. Bouix, *Journal of Materials Science*, 1992, **27**, 1892–1900.

(25) L. Jacobsohn, R. Schulze, M. Maia da Costa and M. Nastasi, *Surface Science*, 2004, **572**, 418–424.

(26) A. V. Shchukarev and D. V. Korolkov, *Central European Journal of Chemistry*, 2004, **2**, 347–362.

(27) W. Oates and A. Stoneham, *Journal of Physics F: Metal Physics*, 1983, **13**, 2427–2436.

(28) G. Henkelman, A. Arnaldsson and H. Jónsson, *Computational Materials Science*, 2006, **36**, 354–360.

(29) C. D. Gelatt, Jr., A. R. Williams and V. L. Moruzzi, *Physical Review B*, 1983, **27**, 2005–2013.

(30) K. J. D. MacKenzie and M. E. Smith, *Multinuclear Solid-State NMR of Inorganic Materials*, ed. R. W. Cahn, Pergamon, Kidlington, 1st edn., 2002.

(31) A. Narayanan, S. J. Hartman and A. D. Bain, *Journal of Magnetic Resonance, Series A*, 1995, **112**, 58–65.

(32) J. van der Klink and H. Brom, *Progress in Nuclear Magnetic Resonance Spectroscopy*, 2000, **36**, 89–201.

(33) B. J. Heuser and J. S. King, *Journal of Alloys and Compounds*, 1997, **261**, 225–230.

(34) B. J. Heuser and J. S. King, *Metallurgical and Materials Transactions A*, 1998, **29A**, 1593.

(35) M. Maxelon, A. Pundt, W. Pyckhout-Hintzen, J. Barker and R. Kirchheim, *Acta Materialia*, 2001, **49**, 2625–2634.

(36) R. Kirchheim, *Acta Metallurgica*, 1981, **29**, 835–843.

(37) R. Lässer and K. .-.-H. Klatt, *Physical Review B*, 1983, **28**, 748–758.

(38) N. W. Ashcroft, *Physical Review Letters*, 2004, **92**, 187002.

(39) P. J. Chupas, X. Qiu, J. C. Hanson, P. L. Lee, C. P. Grey and S. J. L. Billinge, *Journal of Applied Crystallography*, 2003, **36**, 1342–1347.

(40) A. K. Soper and E. R. Barney, *Journal of Applied Crystallography*, 2011, **44**, 714–726.

(41) D. A. Keen, *Journal of Applied Crystallography*, 2001, **34**, 172–177.

(42) M. Basham, J. Filik, M. T. Wharmby, P. C. Y. Chang, B. El Kassaby, M. Gerring, J. Aishima, K. Levik, B. C. A. Pulford, I. Sikharulidze, D. Sneddon, M. Webber, S. S. Dhesi, F. Maccherozzi, O. Svensson, S. Brockhauser, G. Náray and A. W. Ashton, *Journal of Synchrotron Radiation*, 2015, **22**, 853–858.

(43) C. L. Farrow, P. Juhas, J. W. Liu, D. Bryndin, E. S. Božin, J. Bloch, T. Proffen and S. J. L. Billinge, *Journal of physics. Condensed matter : an Institute of Physics journal*, 2007, **19**, 335219.

(44) A. Rose, S. Maniguet, R. J. Mathew, C. Slater, J. Yao and A. E. Russell, *Physical Chemistry Chemical Physics*, 2003, **5**, 3220–3225.

(45) D. Wang and T. B. Flanagan, *Scripta Materialia*, Apr. 2005, **52**, 599–601.

(46) J. Gegner, G. Hörz and R. Kirchheim, *Journal of Materials Science*, Sept. 2008, **44**, 2198–2205.

(47) H. Hofmeister, *Journal of Metastable and Nanocrystalline Materials*, 1999, **2-6**, 325.

(48) E. Hüger and K. Osuch, *Europhysics Letters*, 2003, **63**, 90–96.

(49) J. Walter, J. Heiermann, G. Dyker, S. Hara and H. Shioyama, *Journal of Catalysis*, Jan. 2000, **189**, 449–455.

(50) J. Walter, *Philosophical Magazine Letters*, 2000, **80**, 257–262.

(51) J. Walter, *Advanced Materials*, 2000, **12**, 31–33.

(52) M. Armbrüster, M. Behrens, F. Cinquini, K. Föttinger, Y. Grin, A. Haghofer, B. Klötzer, A. Knop-Gericke, H. Lorenz, A. Ota, S. Penner, J. Prinz, C. Rameshan, Z. Révay, D. Rosenthal, G. Rupprechter, P. Sautet, R. Schlögl, L. Shao, L. Szentmiklósi, D. Teschner, D. Torres, R. Wagner, R. Widmer and G. Wowsnick, *ChemCatChem*, Aug. 2012, **4**, 1048–1063.

(53) B. Yang, R. Burch, C. Hardacre, P. Hu and P. Hughes, *The Journal of Physical Chemistry C*, Feb. 2014, **118**, 3664–3671.

(54) J. S. Yoo, Z.-J. Zhao, J. K. Nørskov and F. Studt, *ACS Catalysis*, 2015, **5**, 6579–6586.

(55) L. Jones, H. Yang, T. J. Pennycook, M. S. J. Marshall, S. Van Aert, N. D. Browning, M. R. Castell and P. D. Nellist, *Advanced Structural and Chemical Imaging*, 2015, **1**, 8.

(56) *Transmission Electron Energy Loss Spectrometry in Materials Science and the EELS Atlas*, ed. C. C. Ahn, Wiley-VCH Verlag GmbH & Co. KGaA, Weinheim, 2nd edn., 2004.

6

Catalytic Testing of the Interstitially Doped Materials

Contents

6.1 Background

The selective hydrogenation of alkynes is an area of huge industrial interest, and therefore a vast amount of work has been published in this field.[1–5] Noble metals, including palladium are incredibly active catalysts for this reaction.[6] In fact, a major issue in hydrogenation reactions is the potency of the palladium catalyst; it will readily over-hydrogenate alkyne species to alkanes destroying the functionality of the molecule. In industry as well as in smaller scale work, it is often necessary to partially hydrogenate a triple bond to the corresponding alkene.[7] There are many routes to controlling the activity of palladium including doping the metal surface, adding reaction modifiers or alloying with another metal to name a few.[1,2,8]

The role of interstitial hydrogen (palladium hydride) in over-hydrogenation is well-known; the labile hydrogen is readily able to leave the lattice and attack an unsaturated bond.[9] Indeed, under industrial conditions it was found that palladium catalysts became more selective under certain conditions that allowed the build-up of sub-surface, or interstitial carbon, blocking the formation of palladium hydride.[10,11]

Interstitial modification is known to affect the surface electronics of the palladium catalyst, a finding which was also discussed in Chapter 5 based on DFT for the novel Pd-$^{\text{interstitial}}$Li system, and for the other interstitial materials.[5,10,12] From an understanding of the Sabatier principle, how the catalyst surface and the reactant interact is sensitive to changes in the electronics of the system.[13] Boron modification has been shown in Chapter 5 to make the palladium surface less electron dense, whilst lithium modification has the opposite effect. Catalytic testing is therefore required to see how this modification has affected these systems in a 'real-world' scenario.

6.2 Objectives

The overarching aim of this chapter is to develop a bank of catalyst testing data for the two interstitially doped materials and their undoped Pd/C counterpart. Hydrogenation reactions were studied in the gas, vapour and liquid phases in order to probe which materials perform best in each system. For the liquid phase hydrogenations, both a non-polar aprotic solvent (dichloromethane) and a polar protic solvent (ethanol) were utilised to elucidate any potential solvent effects on the interstitial materials. The hydrogenation of 3-hexyn-1-ol (HYL) in ethanol was looked at in greater depth to study how the kinetics of the reaction have altered for the palladium catalyst both before and after interstitial doping. The gas-phase hydrogenation of acetylene will be studied under both dilute (a low concentration of acetylene in nitrogen) and industrial (a very low concentration of acetylene in ethylene) conditions. Conclusions will be drawn on how the modification of the

catalyst electronics has affected performance.

6.3 Liquid Phase Hydrogenation

For full details of the experimental set-up for these reactions see Section 3.5.1. In brief, pressurised hydrogenations were undertaken in a High Pressure HEL Chemscan reactor equipped with eight parallel stainless steel Hastelloy reactors. The reactor cells were purged three times with N_2, twice with H_2, and heated to the desired reaction temperature before the reaction was started. The reaction progress was monitored through hydrogen uptake curves (i.e. the amount of H_2 required to maintain the pressure within the reaction vessel). The one uptake point is the point where one mole equivalent of hydrogen has been taken up by the reaction, theoretically converting 100 % of the alkyne to alkene.

Each substrate (Table 3.1, Figure 3.1) was hydrogenated under a pressure of 3 bar hydrogen, temperature of 30 °C and a stirring rate of 1200 rpm. Each reaction consisted of 5 mL of a 0.5 M solution (2.5 mmol) of the substrate in either dichloromethane (DCM) or ethanol and was hydrogenated using 2.50 µmol palladium (except *ortho*-chloronitrobenzene in ethanol where 3.80 µmol catalyst was used). For GC analysis, a 0.5 M solution of dioxane in ethanol was used as the internal standard.

6.3.1 Initial Selectivity Investigations

From the initial catalytic screening discussed in Section 4.6, the hydrogenations of 3-hexyn-1-ol (HYL), diphenylacetylene (DPA), phenylacetylene (PA) and *ortho*-chloronitrobenzene (CNB) to the corresponding alkane/amine (hydrogen uptake curves summarised in Figure 6.1) in ethanol have been analysed.

The hydrogen uptake curves for 3-hexyn-1-ol hydrogenation give the clearest indication of the improvement in selectivity resulting from interstitial doping when compared to an unmodified Pd catalyst, an observation which has previously been

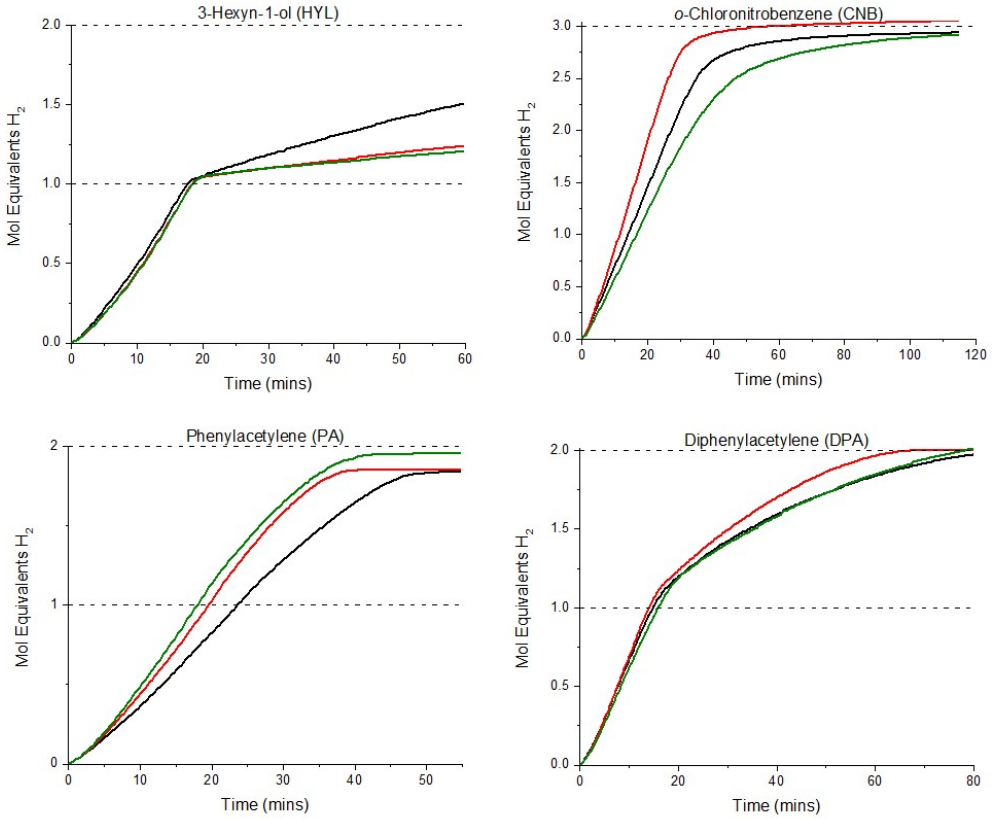

Figure 6.1: Summary of the hydrogen uptake curves for the hydrogenation of PA, DPA, HYL and CNB. Black is the unmodified Pd/C, green Pd-$^{\text{interstitial}}$B/C and red Pd-$^{\text{interstitial}}$Li/C. For the alkyne hydrogenations the dashed lines indicate the one- and two-uptake points. For CNB hydrogenation the dashed line indicates the three-uptake point corresponding to the complete hydrogenation of the nitro group to an amine.

observed in the literature.[5,12] At the one-uptake point the selectivities toward the *cis*-alkene are very similar (88 %) for all catalysts, however it is apparent that the interstitially doped palladium catalysts are more resistant to over-hydrogenation should the reaction be allowed to proceed beyond the one uptake point, similar to what has been previously observed for the known Pd-$^{\text{interstitial}}$B and Pd-$^{\text{interstitial}}$C systems.[5,12,14]

6.3.2 Solvent Effects

It is necessary to build a bank of catalytic testing data to investigate how the subtle modification of the catalyst by interstitial insertion of boron and lithium

affects catalysis. The investigated molecules had a variety of functional groups. The reactions were followed by hydrogen uptake, in the manner of the initial selectivity investigations, and rate constants were calculated from the start of the reaction (stage 1 (R_1), i.e. alkyne to alkene conversion) and from just past the one-uptake point (stage 2 (R_2), alkene to alkane conversion).

The reactions were conducted in both ethanol and DCM to study how the solvent polarity affects the reaction rates. Reaction profiles for the substrates 2-pentyne (PNT), cyclohexylacetylene (CHA), 1-dimethylamino-2-pentyne (DAP) and 5-hexynenitrile (HNN) in both ethanol and dichloromethane can be seen in Figure 6.2. Several other substrates, 4,4-dimethyl-2-pentyne (DMP), ethyl-2-pentynyl ether (EPE), 1-phenyl-1-pentyne (PHP) and 1-bromo-2-pentyne (BRP) were also studied, giving similar reaction curves to Figure 6.2. The ratio of the reaction rate before (R_1) and after (R_2) the one-uptake point is a useful indicator of the selectivity of the catalyst to the alkene.

Rajadhyashka and Karwa, studying the hydrogenation of *ortho*-nitrotoluene, pointed out that other solvent interactions are important, in particular the interaction between the solvent and catalyst surface, the dispersion of heterogeneous catalysts in the reaction media and the solvent-substrate interactions.[15] A body of work has grown studying the effect of solvent on various reactions.[15–24] Rajadhyashka concluded that there was a strong positive correlation between the activity constant of the solvent (a measure of the solvent's non-ideality) and the activity of the catalyst, which retroactively explained Lemcoff's earlier results studying acetone hydrogenation.[25]

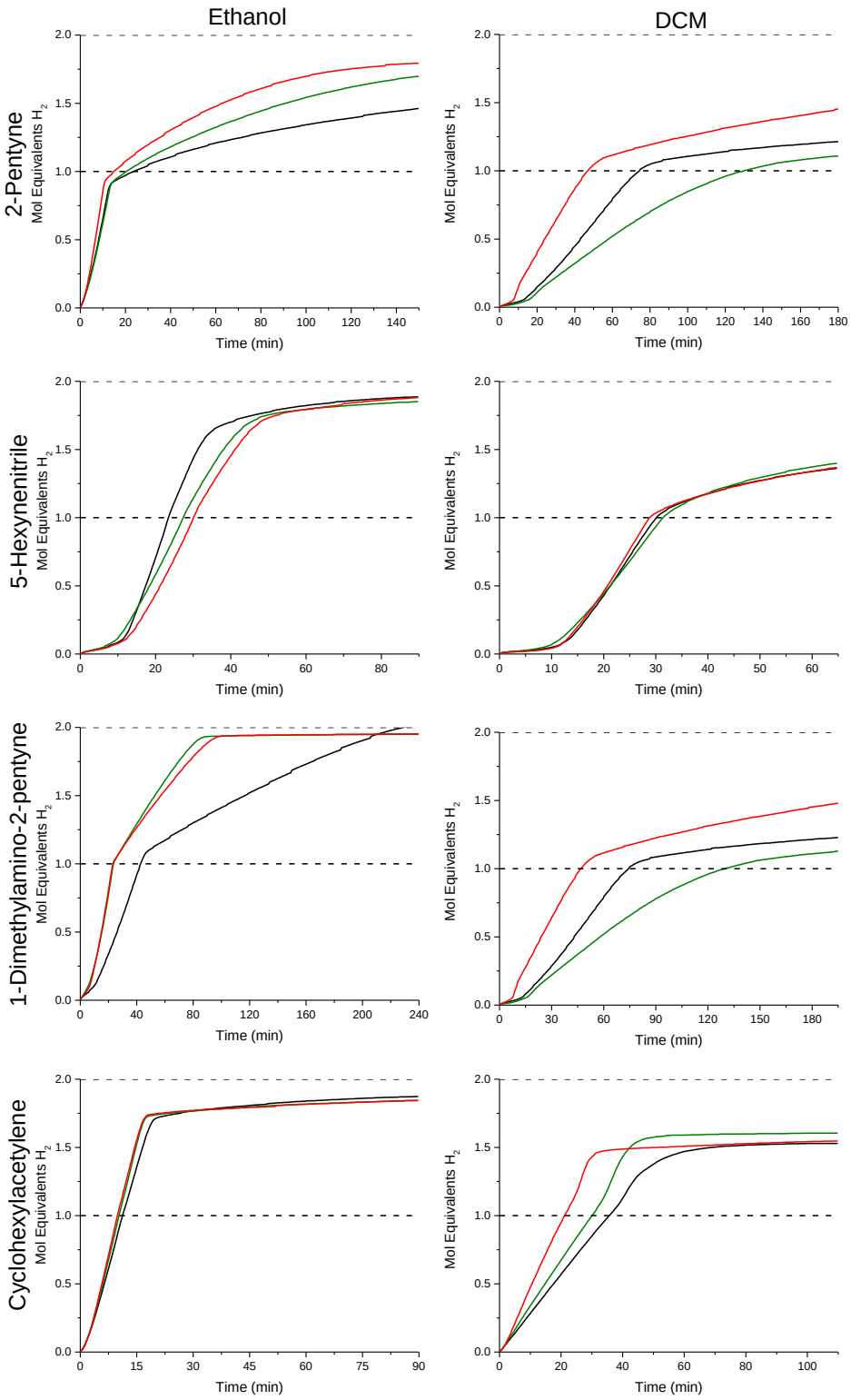

Figure 6.2: The hydrogen uptake curves for four of the studied substrates in dichloromethane and ethanol. The dashed lines indicate that one or two molar equivalents of hydrogen have been taken up by the system. The black line is Pd/C, green Pd-$^{\text{interstitial}}$B/C and the red Pd-$^{\text{interstitial}}$Li/C.

More recent work in this area has studied the effect of solvent on the hydrogenation of 4-phenyl-2-butanone over Pt/TiO_2. The solvent choice affected both the overall reaction rate, and the selectivity towards the hydrogenation of either the phenyl ring or the carbonyl moiety.[26] Aromatic solvents such as toluene bind strongly to the same Pt site that was required for the hydrogenation of the ring. In the case of primary alcohols, the solvent can interact with both the support and the metal, forming a dense over-layer. As the carbon number increases the packing efficiency of the alcohol increases, reducing the overall rate. These observations allowed Wilkinson *et al.* to propose a kinetic model which matched well to the experimental data.[27] The reaction was found to have two reaction sites, the phenyl ring was hydrogenated over the platinum surface and was strongly influenced by the solvent-catalyst interaction, conversely, the ketone hydrogenation was not affected by solvent choice as it was hydrogenated at the metal-support interface.[27]

There is a large limitation to this approach however, as it assumes a uniform rate expression for the hydrogenation of each reactant regardless of the solvent used. The work of Gamez and others have shown that reactant orders do change depending on the solvent, so the solvent contribution needs to be considered rather than applying a solvent activity constant as a general factor at the end of the rate analysis.[18]

It is clear that the balance between the interactions of the solvent, substrate and catalyst goes beyond simply accounting for hydrogen solubility variance. Hydrogen solubility figures for the two solvents are: for ethanol, $3.45\,\mathrm{mmol\,dm^{-3}\,atm^{-1}}$ and for DCM, $2.77\,\mathrm{mmol\,dm^{-3}\,atm^{-1}}$.[28–30] Taking the rate constants for the reactions in ethanol and DCM (summarised in Tables 6.1 and 6.2 respectively), it is clear that the vast majority of reactions proceed faster in ethanol than in DCM. These differences in reactivity cannot be attributed solely to the differences in hydrogen solubility. Should H_2 solubility be the sole factor, all reactions would be 25 % quicker in ethanol. This is not the case. Also, the catalysts are supported on carbon so there is less likely to be a major metal-support interaction as seen in other alumina

or titania systems.[31] Similarly, all catalysts disperse equally well in DCM or ethanol. Differences between how the catalysts perform in each solvent system are due to intrinsic properties of the catalyst rather than an external physical property.

Table 6.1: A summary of the rate constants (in s^{-1}) for first (alkyne to alkene) and second (alkene to alkane) stages of the reaction for the 11 alkyne hydrogenations studied in ethanol. R_1/R_2 is the ratio of the reaction rate before (R_1) and after (R_2) the one-uptake point

Substrate	**Pd/C**			**PdB/C**			**PdLi/C**		
	R_1	R_2	$\frac{R_1}{R_2}$	R_1	R_2	$\frac{R_1}{R_2}$	R_1	R_2	$\frac{R_1}{R_2}$
HNN	545.0	409.2	1.33	365.2	314.8	1.16	374.0	305.2	1.23
HYL	426.0	97.6	4.36	401.4	37.8	10.62	387.4	38.2	10.14
EPE	270.4	225.4	1.20	223.0	184.2	1.21	439.6	265.0	1.66
DMP	406.6	108.8	3.74	501.2	145.6	3.44	488.0	68.8	7.09
PNT	551.4	44.8	12.31	529.2	75.2	7.04	684.6	91.0	7.52
BRP	15.8	10.2	1.55	20.4	10.4	1.96	13.0	9.4	1.38
DAP	183.4	100.4	1.83	372.0	123.4	3.01	396.2	108.4	3.65
PA	295.6	284.0	1.04	372.8	370.2	1.01	413.2	355.8	1.16
CHA	731.2	654.2	1.12	832.0	684.4	1.22	859.8	693.0	1.24
DPA	516.0	176.0	2.93	484.0	167.6	2.89	566.8	200.2	2.83
PHP	28.6	4.6	6.22	36.4	3.4	10.71	36.8	8.0	4.60

Table 6.2: A summary of the rate constants (in s^{-1}) for first (alkyne to alkene) and second (alkene to alkane) stages of the reaction for the 11 alkyne hydrogenations studied in DCM. R_1/R_2 is the ratio of the reaction rate before (R_1) and after (R_2) the one-uptake point

Substrate	**Pd/C**			**PdB/C**			**PdLi/C**		
	R_1	R_2	$\frac{R_1}{R_2}$	R_1	R_2	$\frac{R_1}{R_2}$	R_1	R_2	$\frac{R_1}{R_2}$
HNN	394.6	89.4	4.41	336.0	118.0	2.85	401.0	77.4	5.18
HYL	323.2	55.4	5.83	306.0	56.8	5.39	395.0	34.0	11.62
EPE	291.2	178.6	1.63	324.4	195.6	1.66	455.6	140.0	3.25
DMP	21.8	2×10^{-5}	2×10^{6}	28.2	2×10^{-5}	2×10^{6}	56.2	2×10^{-5}	4×10^{6}
PNT	334.8	1.3	233.3	284.4	3.7	81.93	442.8	0.62	711.3
BRP	1.36	—	—	0.91	—	—	1.0	—	—
DAP	115.6	12.8	9.03	74.0	12.2	6.07	172.4	27.0	6.39
PA	243.6	118.8	2.05	195.2	100.4	1.94	269.8	200.4	1.35
CHA	195.2	57.8	3.38	232.6	35.6	6.53	349.4	14.2	24.61
DPA	30.0	14.8	2.03	33.6	4.8	7.00	42.2	21.2	1.99
PHP	0.54	—	—	0.39	—	—	2.23	—	—

Some of the reactions can be discounted from analysis, for example BRP

exhibited cleavage of the C−Br bond leading to rapid catalyst deactivation.[32] Mastalir however, achieved an excellent reaction rate for the hydrogenation of PHP under similar conditions in tetrahydrofuran.[33] Tetrahydrofuran as a solvent exhibits similar hydrogen solubility and dielectric constant to DCM, yet the reaction behaviour is transformed.[34] Here, the reaction in ethanol and DCM exhibited very little to no activity suggesting that the selection of solvent plays a large role in the rate of a reaction.

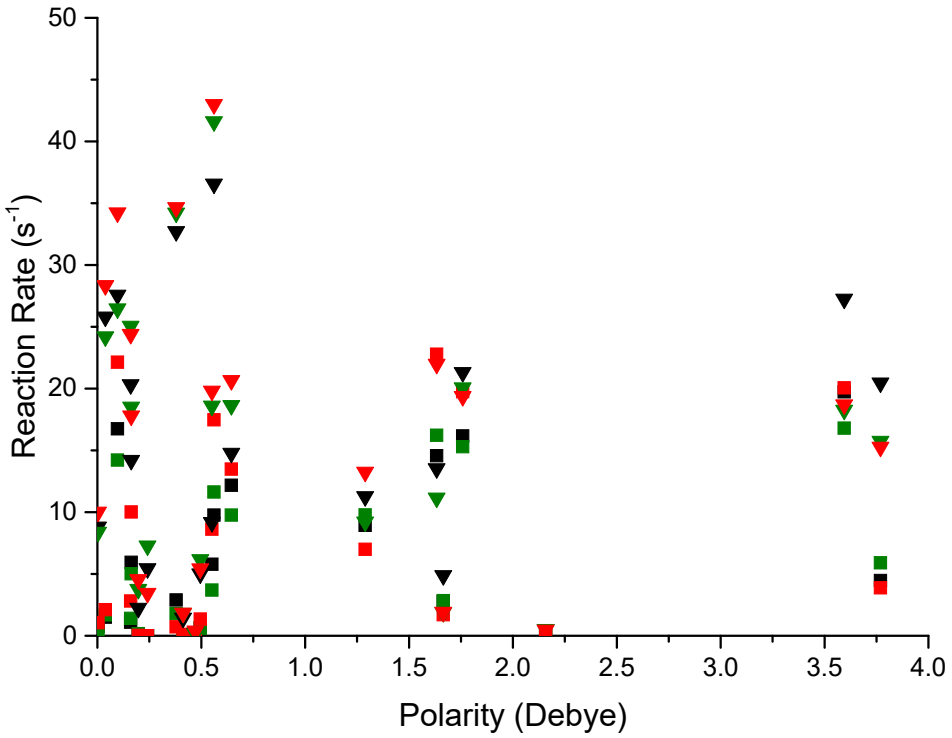

Figure 6.3: The reaction rates for each of the studied hydrogenations during the first stage against the calculated polarity of the substrate molecule. ▼ are the reactions in ethanol, ■ are the reaction in DCM. Black is unmodified Pd/C, green Pd-$^{\text{interstitial}}$B/C and red Pd-$^{\text{interstitial}}$Li/C.

A more studied reaction is that of the hydrogenation of 2-pentyne. Jackson *et al.* observed that by keeping all other things equal and simply changing the support oxide, the ratio of the *cis*/*trans* isomers changed as well as the rate of reaction.[35] Bennett and co-workers conducted a more exhaustive study on this system, including several solvent regimes, and concluded that (at least for Pd/Al_2O_3) a non-polar

aprotic solvent in heptane gave a much higher rate of reaction than the polar protic solvent, isopropanol.[16] This is in direct contradiction to what was seen here, with rates of the alkyne hydrogenation in ethanol consistently higher than in DCM for all three catalysts (about 550 to 350 s^{-1} respectively). Notable differences in activity of several orders of magnitude were seen for 4,4-dimethyl-2-pentyne and diphenylacetylene hydrogenations which were virtually inactive in the non-polar solvent. Other reactions such as the hydrogenation of ethyl-2-pentynyl ether showed little change in activity between the two solvent regimes. It is apparent that there are a large number of variables controlling the equilibria between the substrate, catalyst and solvent and their precise interplay varies from system to system.

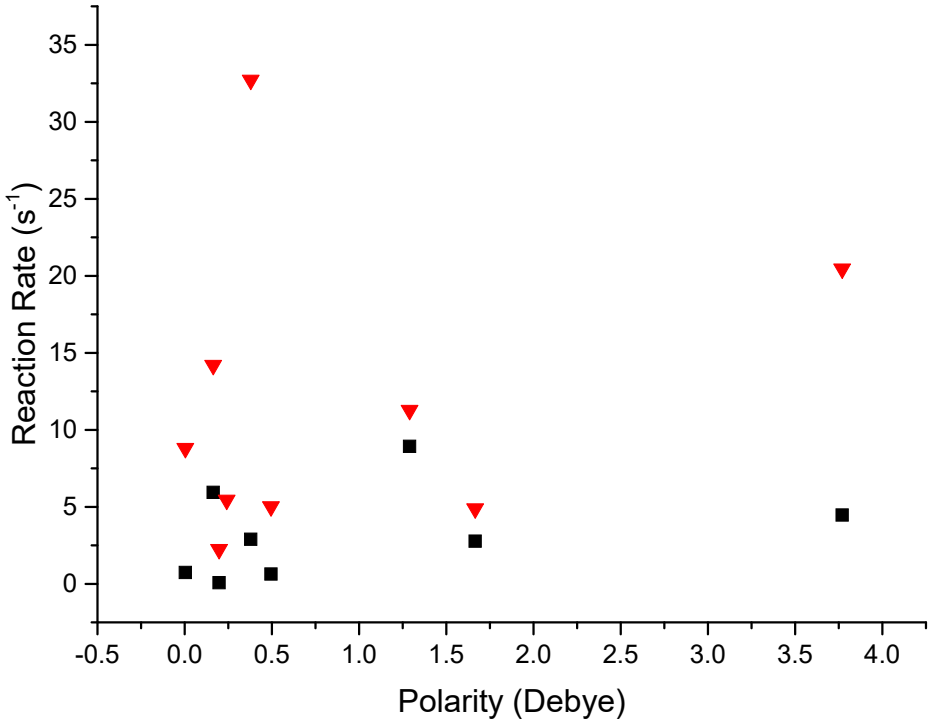

Figure 6.4: The reaction rates for the second stage of the reactions in ethanol (▼) and DCM (■) for only the unmodified Pd/C.

An attempt was made to study the correlation between the polarity of the substrate and the rate of hydrogenation for either stage of the reaction in either solvent (Figure 6.3). There is what appears to be a slight trend toward a faster reaction rate for an increasingly polar molecule; however, the uncertainty in this is

much too great to be considered a firm conclusion. This is illustrated by Figure 6.4, where even with taking one small subset of the data there is still too much variance to ascribe the differences in reaction rate to reactant polarity. It is much likelier that a combination of molecular sterics and solvent effects are the dominating factors under these conditions. Therefore, it is not possible to draw an overarching conclusion with this number of potential variables but it is possible to see that interstitial modification by either boron or lithium has changed how the catalyst behaves in each reaction.

6.3.3 Kinetic Analysis of the 3-Hexyn-1-ol Hydrogenation

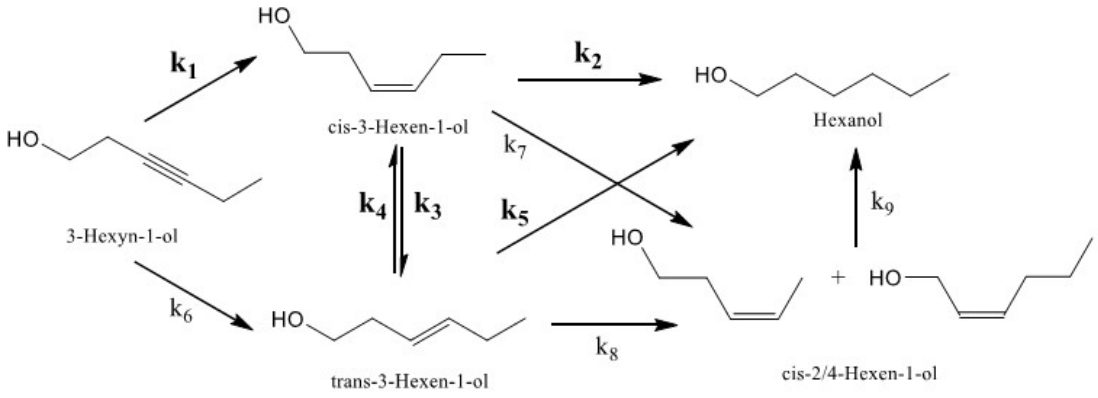

Figure 6.5: The detailed mechanism for the hydrogenation of 3-hexyn-1-ol over palladium based catalysts

It is of interest to see how the modification of the palladium through interstitial insertion has affected the reaction of the well-studied molecule, 3-hexyn-1-ol.[12,36] The advantage this reaction has over the other studied hydrogenations is that it has an easily analysable rate of reaction, the intermediates are not toxic or too volatile, and it is a key molecule in the fragrance industry.[37] Detailed kinetic analysis was performed on the reaction data for this hydrogenation, conducted in ethanol at ambient pressure. The analysis took into account bond-shifted

product formation (Figure 6.5) with the rate equations derived from this reaction schematic (Equations 6.1 to 6.6).

$$\frac{d[A]}{dt} = -\theta_A(k_1 + k_6) \tag{6.1}$$

$$\frac{d[B]}{dt} = k_1\theta_A + k_4\theta_C - \theta_B(k_2 + k_3 + k_7) \tag{6.2}$$

$$\frac{d[C]}{dt} = k_6\theta_B + k_8\theta_C - \theta_C(k_4 + k_5 + k_8) \tag{6.3}$$

$$\frac{d[D]}{dt} = k_7\theta_B + k_8\theta_C - k_9\theta_D \tag{6.4}$$

$$\frac{d[E]}{dt} = k_2\theta_B + k_5\theta_C - k_9\theta_D \tag{6.5}$$

$$\theta_i = \frac{K_i P_{(i)}}{1 + \int_A^E K_i P_{(i)}} \tag{6.6}$$

Where A = 3-hexyn-1-ol, B = *cis*-3-hexen-1-ol, C = *trans*-3-hexen-1-ol, D = *cis*-2/4-hexen-1-ol, E = hexan-1-ol, K_i = adsorption constant of species i, $P_{(i)}$ = equilibrium concentration of i, and θ_i = probability of a surface site being occupied by i. The equations are based upon the Horiuti-Polanyi understanding of alkyne and alkene hydrogenation, and the Langmuir-Hinshelwood mechanism which requires both alkyne/alkene and hydrogen to be bound to the metal surface for the reaction to proceed (see Section 1.4).

The reaction profiles (Figure 6.6) show an excellent agreement between the experimental and fitted data, with a maximum spoil of 0.04. The derived rate constants for the catalysts are summarised in Table 6.3.

There are several interesting features to observe here. Firstly, the Pd-$^{\text{interstitial}}$B/C

Table 6.3: Summary of the calculated rate constants for the observed hydrogenation and isomerisation process seen in the catalytic conversion of 3-hexyn-1-ol over various Pd catalysts. k_n is in units of min^{-1}, $\sum k_{semi} = k_1 + k_6$, $\sum k_{isom} = k_3 + k_4$ and $\sum k_{full} = k_2 + k_5 + k_7 + k_8 + k_9$

Rate Constant	Pd/C	Pd-$^{\text{interstitial}}$B/C	Pd-$^{\text{interstitial}}$Li/C
k_1	679.0	703.4	518.5
k_2	339.0	486.5	432.0
k_3	1131.4	884.2	1143.2
k_4	776.0	617.6	596.7
k_5	651.9	199.3	1145.4
k_6	0.6	0.0	0.0
k_7	629.5	59.8	657.1
k_8	6.4	24.6	5.3
k_9	65.1	574.4	92.3
$\sum k_{semi}$	679.7	703.4	518.5
$\sum k_{full}$	1692.0	1344.6	2332.1
$\sum k_{isom}$	1907.5	1501.8	1739.8
$\sum k_{full} / \sum k_{semi}$	0.89	0.90	1.34

catalyst exhibits much less conversion to 1-hexanol after five hours than the other catalysts (34 % against 49 % for unmodified Pd/C and 57 % for Pd-$^{\text{interstitial}}$Li/C). In the reaction conducted at 3 bar hydrogen, both lithium modified and boron modified catalysts had a similar rate for the alkene to alkane step (Table 6.1) which suggests that at reduced pressure how the catalysts and the reagents interact is different. There is also very little to no activity for the direct conversion of 3-hexyn-1-ol to *trans*-3-hexyn-1-ol with any of the catalysts (k_6).

The unmodified catalyst has the intermediate reaction rate but the highest incidence of isomerisation products. This is matched by the higher rate of *trans*-3-hexen-1-ol hydrogenation to the alkane. There is a large amount of interconversion between the *cis*- and *trans*-3-hexen-1-ol isomers (k_3/k_4), with k_3, the isomerisation of the *cis*- product slightly larger, as would be expected given that the *trans*- isomer is thermodynamically more stable by 0.14 eV.[12]

The most potent catalyst for this reaction is the lithium modified palladium. It exhibits the highest rate of full hydrogenation and an intermediate level of

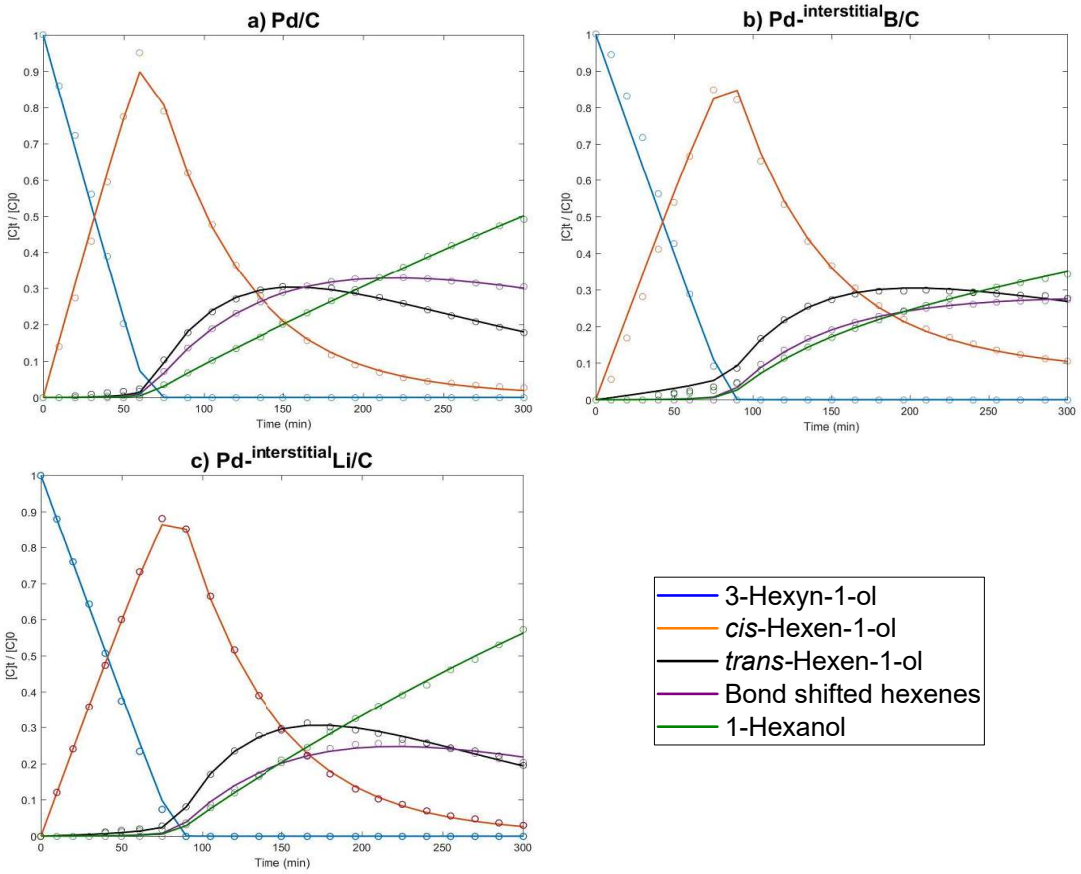

Figure 6.6: The calculated fits (lines) to the experimental data (points) for the three catalysts a) Pd/C, b) Pd-$^{\text{interstitial}}$B/C and c) Pd-$^{\text{interstitial}}$Li/C for the hydrogenation of HYL.

isomerisation. Focussing on the individual components of the reaction, it appears that the key area is the isomerisation between the *cis*- and *trans*-3-hexen-1-ol isomers and their subsequent full hydrogenation to 1-hexanol. Pd-$^{\text{interstitial}}$Li/C has a similar rate of isomerisation to the *trans*-3-hexen-1-ol product as the unmodified Pd/C (1100 min^{-1}, but the lithium modified catalyst has a considerably higher rate of hydrogenation from this component compared to the unmodified Pd/C. The initial hydrogenation step from alkyne to alkene is also slower than the other catalysts. Potentially, the increased electron density in the lithium-modified catalyst has an excessively strong interaction with the alkyne triple bond in comparison to the other two catalysts. This can be considered almost a poisoning effect with the alkyne blocking active sites on the Pd-$^{\text{interstitial}}$Li metal surface.

Kinetic analysis of the ambient pressure reaction shows that the boron modified palladium is the ideal catalyst for the alkyne to alkene hydrogenation. It has the fastest rate for the initial hydrogenation step ($700\,\mathrm{min}^{-1}$) coupled with the lowest rate for the further hydrogenation of 3-hexen-1-ol. There is also a remarkably low amount of isomerisation in comparison to the other catalysts. This suggests that once the 3-hexyn-1-ol has hydrogenated it has a lower residence time on the electron deficient Pd-$^{\mathrm{interstitial}}$B/C surface, lowering the available time for subsequent hydrogenation or bond-shifting events. This theory ties in with what is seen for the unmodified Pd/C (essentially electron neutral) which is intermediate of the two catalysts in terms of full hydrogenation rate but has the highest rates in terms of isomerisation products. This implies that the alkene is residing on the catalyst surface for longer, allowing for more isomerisation, but not long enough for the complete hydrogenation. Pd-$^{\mathrm{interstitial}}$Li/C (electron rich) on the other hand allows the alkene to be bound more strongly again, allowing more full hydrogenation events to occur with a subsequent reduction in isomerisation products.

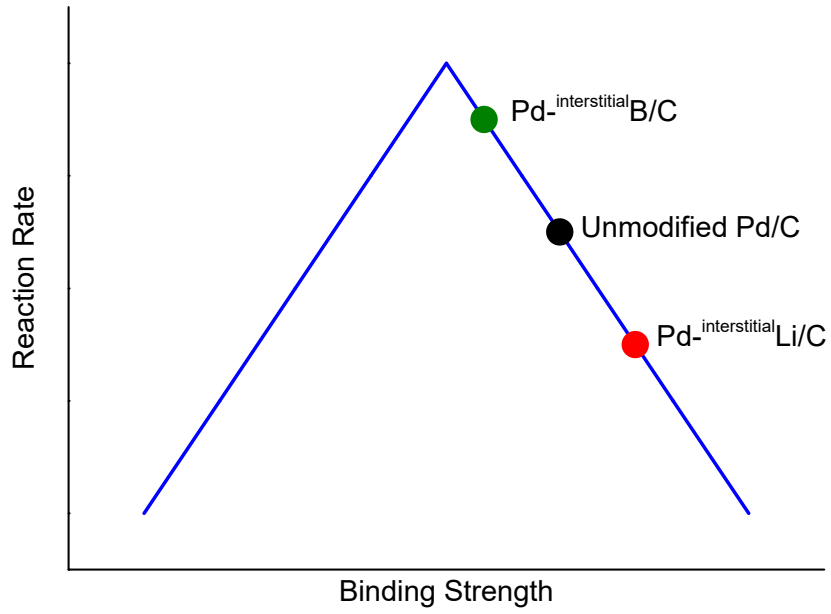

Figure 6.7: An illustration of how changing the molecule binding strength through interstitial doping affects the reaction rate.

In terms of electronics, the predicted reduction of electron density at the Fermi level (ϵ_f) weakens the adsorptive strength of the Pd-$^{\text{interstitial}}$B/C catalyst, allowing the *cis*- isomer to desorb more readily and preventing a greater rate of *cis*/*trans* isomerisation as well as over-hydrogenation.[12] Conversely, lithium, with its predicted increase in electron density at ϵ_f, binds the substrate more strongly leading to a greater rate of isomerisation and over-hydrogenation compared the unmodified catalyst. Indeed, the binding of the alkyne to the Pd-$^{\text{interstitial}}$Li/C surface is strong enough to slow the rate of alkyne hydrogenation as the rate of desorption is reduced.[38] This is the Sabatier principle in action and is illustrated by Figure 6.7.

6.3.4 Liquid Phase Hydrogenation Conclusions

It is clear that the modification of the palladium by either boron or lithium has had a noticeable, and differentiable, impact upon catalytic performance. The modification often (but not in every case) leads to a decrease in the rate of over-hydrogenation of the desired alkenes.

The large differences in activity between the hydrogenations conducted in DCM or ethanol (beyond what would be expected by simple hydrogen solubility) suggest that the interactions of the solvent with the substrates studied and the catalyst cannot be ignored, and thus teasing out how the interstitial modification has altered the catalyst/substrate interaction becomes increasingly difficult under this testing regime.

A detailed kinetic analysis of one well-studied reaction, the hydrogenation of 3-hexyn-1-ol, has shown that the modification does induce changes in the rates of isomerisation and full hydrogenation for the catalysts. Under the conditions studied the boron modification would be considered the best catalyst of the three. In order to further investigate the catalytic implications of boron and lithium modification of the palladium it is necessary to remove the solvent effects which

could be obscuring the true nature of the catalysts. Therefore, other alkyne hydrogenation systems were investigated.

6.4 Vapour Phase Hydrogenation of 1-Pentyne

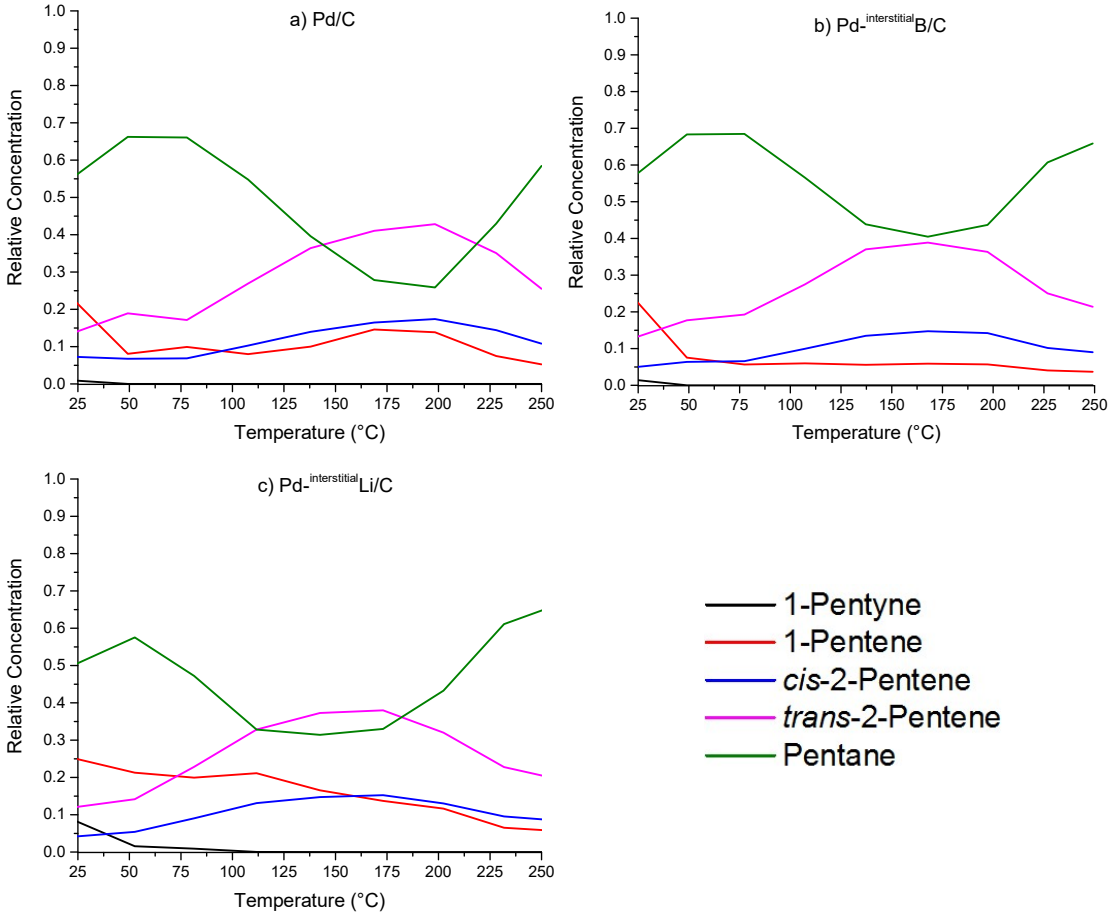

Figure 6.8: The vapour-phase hydrogenation curves of 1-pentyne for the three catalysts a) Pd/C, b) Pd-$^{\text{interstitial}}$B/C and c) Pd-$^{\text{interstitial}}$Li/C during a heating ramp. The product concentrations are normalised to 1.

In order to transition away from a liquid phase system where solvent interactions could mask the subtle changes in catalyst behaviour, the vapour phase hydrogenation of 1-pentyne was investigated. Full details can be found in Chapter 3 and follow the method of Hu *et al.*[39]

As was seen with the kinetic analysis of the 3-hexyn-1-ol hydrogenation reaction,

the introduction of an interstitial dopant to the host palladium induces changes in the isomerisation processes. With the vapour phase hydrogenation, any solvent effect is removed that may have been obscuring the true effect of the dopant. As this is a continuous flow process as opposed to the batch processes tested earlier, continuous monitoring of the sample progress is possible and therefore, the effect of temperature on the isomerisation and hydrogenation of 1-pentyne can be observed.

The U-shaped profile for the concentration of pentane against temperature can be explained by considering the competing processes on the surface of the catalyst. Namely, the rate of adsorption/desorption of the alkene product and the isomerisation rate of 1-pentene. It is, in essence, an equilibrium between the thermodynamic and kinetic control regions.[40,41] At lower temperatures for all three catalysts, the typical residence times of the alkene are longer which allows for over-hydrogenation of 1-pentene. As the temperature increases, reducing the overall residence time, the rate of over-hydrogenation decreases and the rates of formation of the isomerisation products begin to dominate, i.e. the reaction enters the region of kinetic control. At higher temperatures, the rate of total hydrogenation again dominates as the reaction becomes thermally controlled.

What is of interest from these results is the temperature at which these processes occur differs for all three catalysts, as well as the ratio of the products. The unmodified catalyst has the lowest concentration of pentane at 200 °C, boron modified at 175 °C, and lithium modified at 160 °C. This coupled with Pd-$^{\text{interstitial}}$B/C having the highest concentration of pentane of all the catalysts indicates that the alkene has a worse interaction, in terms of selectivity. Pd-$^{\text{interstitial}}$Li/C, on the other hand, has a higher concentration of *trans*-2-pentene at a lower onset temperature suggesting a stronger substrate surface interaction that would be expected by a more electron rich catalyst. The weakened alkene/surface interaction with the electron poor Pd-$^{\text{interstitial}}$B/C, which was an advantage for the hydrogenation of 3-hexyn-1-ol, appears to be a disadvantage under this testing regime. As this is

a continuous flow process, the reactant molecules are moving rapidly through the system. Should the residence time for each alkyne/alkene component be longer, as you expect to see on a more electron rich catalyst, the active site is effectively blocked in that instant to another passing reactant molecule, preventing the chance of another hydrogenation event resulting in a lower TOF.

6.5 Acetylene Hydrogenation

Acetylene hydrogenation is the simplest of the hydrocarbon saturations, with a wide variance in testing procedures and results depending upon the conditions chosen.[1,2] Two systems have been studied for this work, one looking at a dilute $C_2H_2 : H_2 : N_2$ system (1:1:18 or 1:2:17) which is not representative of an industrial system but will probe how the catalysts behave under unusual conditions.[42] The other was the industrial testing rig run by Dr Pilar Gomez-Jimenez at the Johnson Matthey Technology Centre, Sonning Common.

6.5.1 In-House Testing

For the in-house testing the total flow rate was fixed at $50\,\mathrm{mL\,min^{-1}}$, of which acetylene comprised $2.5\,\mathrm{mL\,min^{-1}}$ (5 % of the total flow). Hydrogen was either $2.5\,\mathrm{mL\,min^{-1}}$ or $5\,\mathrm{mL\,min^{-1}}$ depending on the testing regime (5 % or 10 % total flow) with the rest of the gas flow being nitrogen. Full experimental details can be found in Chapter 3.

Initial investigations focussed upon the selectivity of the catalysts in a hydrogen rich atmosphere (two-parts hydrogen for one-part acetylene) (Figure 6.9) at several temperature points. It is important to note that 100 % acetylene conversion was achieved for all catalysts under these conditions. Pd-$^{\mathrm{interstitial}}$Li/C appears to be the catalyst most resistant to over-hydrogenation, as with a 1:2 acetylene to hydrogen ratio complete saturation of the carbon-carbon triple bond can be expected.

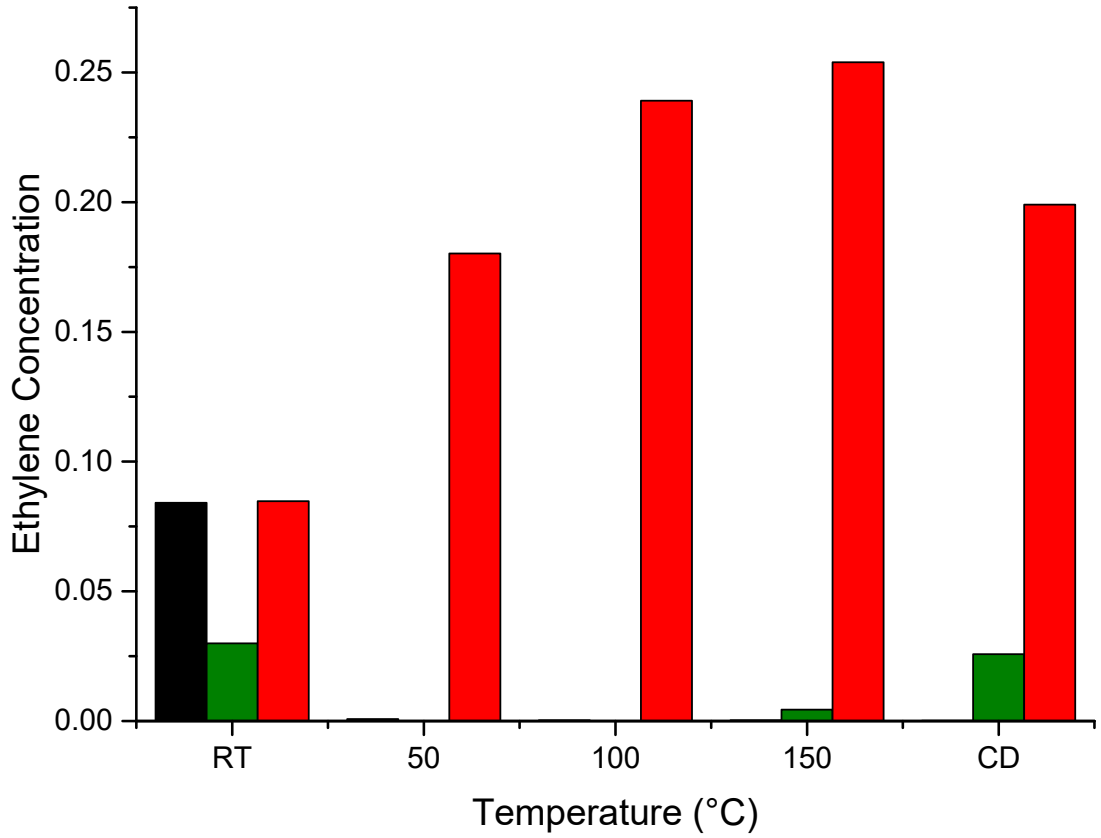

Figure 6.9: Acetylene hydrogenation in a hydrogen rich atmosphere. The black bars are unmodified Pd/C, green Pd-$^{\text{interstitial}}$B/C and red Pd-$^{\text{interstitial}}$Li/C. RT refers to an initial run at room temperature. CD is a run conducted at 50 °C after cooling the system from 150 °C.

These conditions had such a large excess of both catalyst and hydrogen it is unusual to see conversion that is not 100 % to ethane, unless, as was the case with Pd-$^{\text{interstitial}}$B/C in 1-pentyne hydrogenation, the longer residence time of acetylene on the surface of Pd-$^{\text{interstitial}}$Li/C in comparison to the other catalyst allows a fraction of ethylene to pass through the reactor without hydrogenating. However, it is necessary to test the catalysts at a point where acetylene conversion is not 100 % to truly gauge their effectiveness at this reaction. This was achieved by reducing the amount of catalyst 14× and reducing the amount of hydrogen in the gas flow by 50 %. The temperature was fixed at 75 °C.

Figure 6.10 shows the relative selectivity to ethylene (dashed lines) and conversion of acetylene (solid lines) over eight and a half hours of continuous flow. All the

catalysts exhibit some deactivation over this time period. The unmodified Pd/C shows the expected inverse correlation between conversion and selectivity, with conversion declining after six hours potentially due to a build-up of carbon fragments both within and on the catalyst.[10,43] The interstitially modified catalysts have similar behaviour, with ethylene selectivity constant at 80 % despite a slight but steady decrease in acetylene conversion, potentially due to coking.

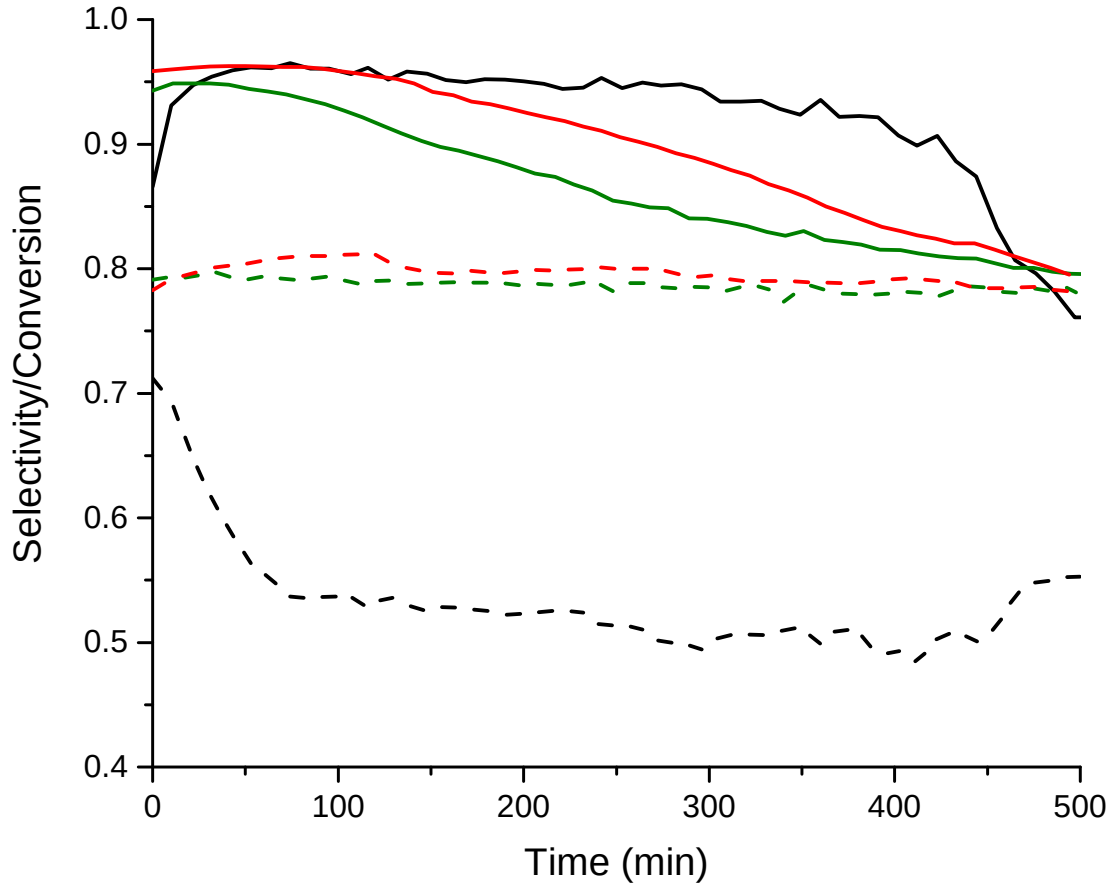

Figure 6.10: The relative conversion of acetylene (bolded lines) and selectivity towards ethylene (dashed lines) for the unmodified Pd/C (black), Pd-$^{\text{interstitial}}$B/C (green) and Pd-$^{\text{interstitial}}$Li/C (red).

Correcting the conversion of acetylene to ethylene for surface area shows that the boron modified catalyst has the highest turn-over frequency per metal site of all the catalysts (Figure 6.11). The unmodified Pd/C has a comparatively low selective turn-over frequency to C_2H_4 (the TOF for C_2H_2 to C_2H_4 minus TOF for

C_2H_4 to C_2H_6. In reality, there is a large amount of over-hydrogenation to ethane, supressing this value). It is not possible however, to conclude with certainty that the differences between the Pd-^{interstitial}B/C and Pd-^{interstitial}Li/C catalysts are due to the electronic modification of the catalyst. The large increase in selectivity towards ethylene for the two catalysts is most likely due to the blocking of the interstitial site for hydrogen, a leading cause of over-hydrogenation as this interstitial hydrogen readily escapes the lattice to hydrogenate a system.[1,5,44]

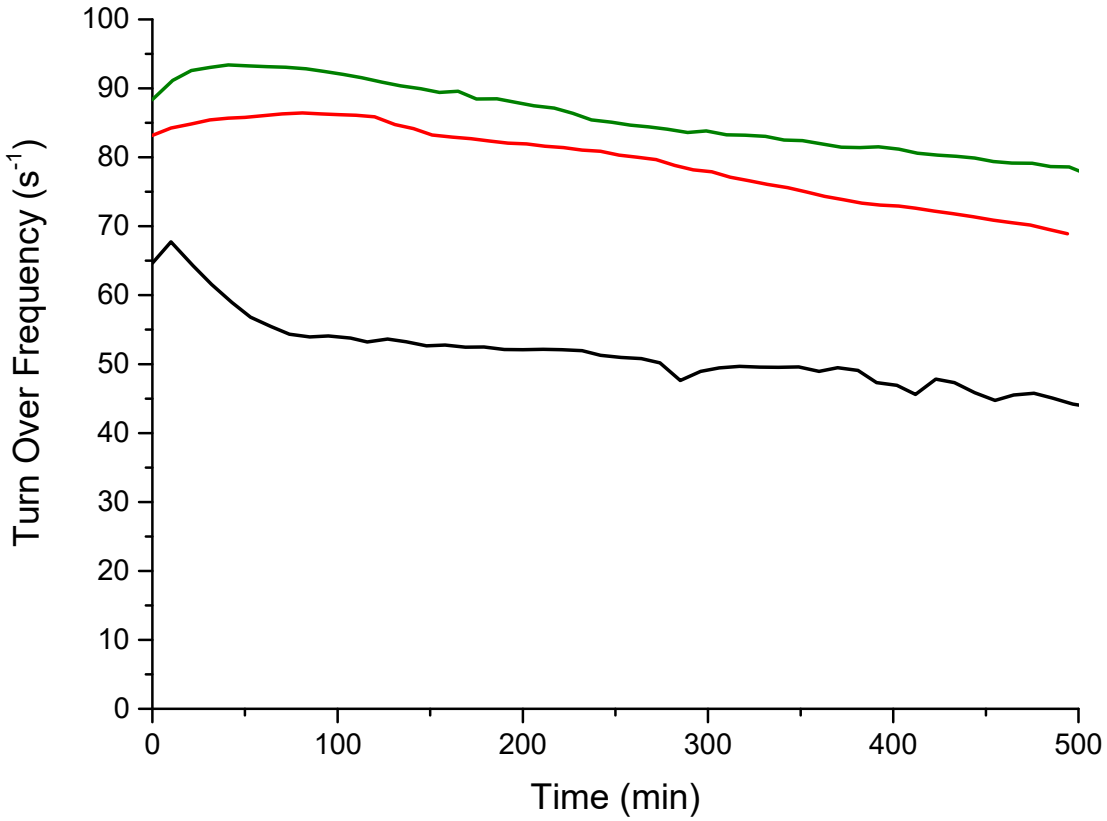

Figure 6.11: The turn over frequency in terms of atoms of acetylene converted to ethylene per second, corrected for metal surface areas. The black is unmodified Pd/C, green Pd-^{interstitial}B/C and Pd-^{interstitial}Li/C is red.

6.5.2 Industrial Testing

Under industrial acetylene hydrogenation conditions, both acetylene conversion and final ethane concentration are tracked. This is because the quantity of ethylene in

the feedstream is very high, set to (97.9 %), with the other components much lower. Acetylene is set to 1 % of the total flow, with a slight excess of hydrogen (1.1 %). As the feedstream has such a high relative concentration to the other components it is very difficult to track precisely the amount of ethylene is being produced.

Flow rates and reaction temperature parameters are adjusted for each catalyst to give comparable results at set levels of acetylene conversion.[45] This has the added effect of removing variations in residence time as a factor in catalyst performance. In the industrial setting it is key to maximise acetylene conversion, as this is in fact detrimental to further industrial processes such as polymerisation.[46,47] Similarly, minimising over-hydrogenation to ethane is necessary from an economic point of view. The results are summarised in Figure 6.12.

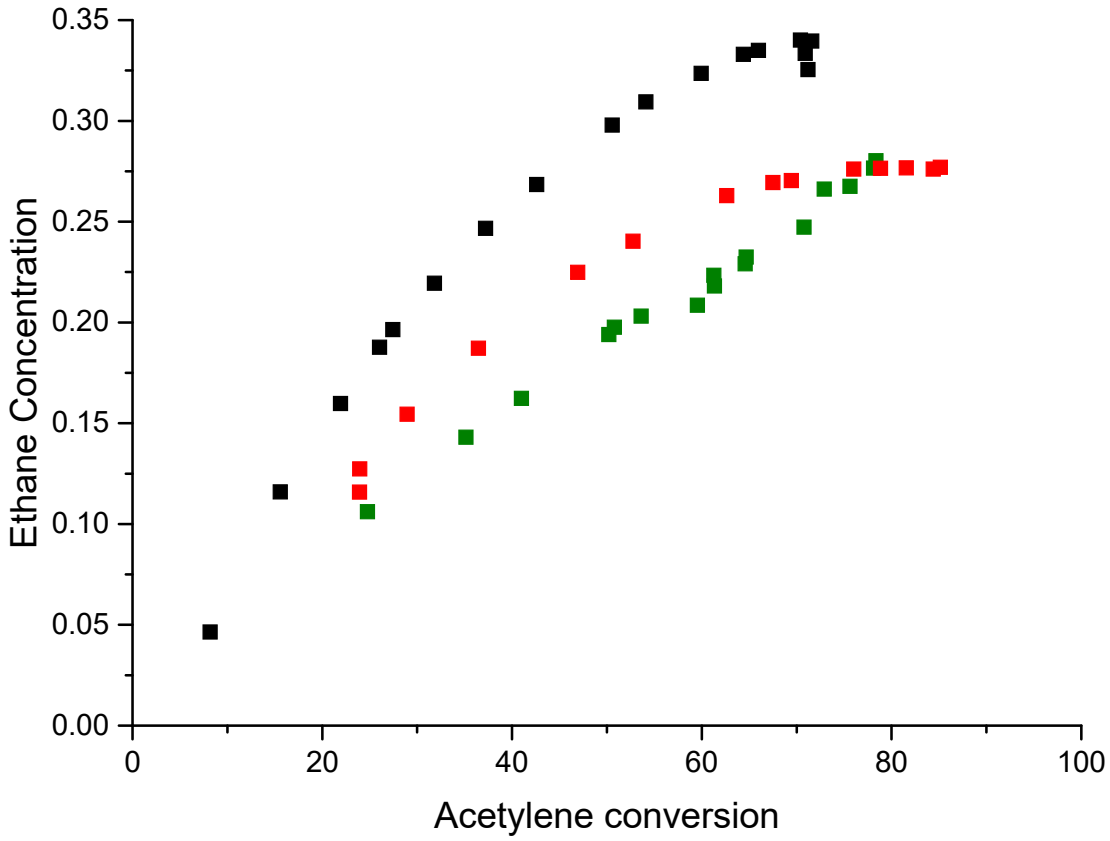

Figure 6.12: The comparison between down-stream ethane concentration and acetylene conversion for the three catalysts. The black is unmodified Pd/C, green Pd-$^{\text{interstitial}}$B/C and Pd-$^{\text{interstitial}}$Li/C is red.

It appears that the physical blockage of the interstitial sites by either boron or lithium has caused a reduction in over-hydrogenation to ethane. At first glance, the boron-modified catalyst has the best performance of the interstitially modified catalysts, but under industrial testing conditions the dispersion of the catalyst can play a key role. Indeed, a 5 % weight loading of palladium is much higher than what would be seen for an industrial catalyst.[48–51] The dispersions are similar for the three catalysts. Pd/C is 5.566 %, Pd-$^{\text{interstitial}}$B/C is 4.744 % and Pd-$^{\text{interstitial}}$Li/C is 5.062 %. The difference between the two interstitially modified catalysts is small enough that the initial conclusion of Pd-$^{\text{interstitial}}$B/C being the best catalyst for this reaction under these conditions is valid.

6.6 Conclusions

A range of different reactant molecules were hydrogenated in two solvents, ethanol and DCM). Some differences in reactivity and selectivity due to the catalyst modification became apparent. To study this further, 3-hexyn-1-ol was studied in-depth which allowed some preliminary conclusions to be drawn. The observed differences in reaction rate, and what influence the modifiers had had on the catalysts, could be assigned to changes in electron density at the Fermi level of the catalyst. Namely, the increase in electron density at the Fermi level for the Li modified sample led to a longer residence time for the 3-hexenol products giving rise to an increased rate of over-hydrogenation, whereas the electron deficient B modified catalyst had a shorter residence time giving better selectivity and initial rate of hydrogenation.

This effect was further studied with the solvent-free vapour phase hydrogenation of 1-pentyne, and the gas phase hydrogenation of acetylene under a range of conditions. Differences in selectivity and product composition led to the overall conclusion that the interstitial modification is playing a role in catalysis. Depending on the conditions investigated, either the boron modified or lithium modified

catalysts are the most effective for a given reaction.

Interstitial modification allows tuning of the catalysts for any hydrogenation reaction. In broad strokes, the boron-modified palladium is more suited to batch processes and partial hydrogenations where a reduced surface residence time is desired, and the lithium modified catalyst performs better in some continuous flow systems and hydrogenation regimes.

6.7 References

(1) A. Borodziński and G. C. Bond, *Catalysis Reviews*, July 2006, **48**, 91–144.

(2) A. Borodziński and G. C. Bond, *Catalysis Reviews*, Aug. 2008, **50**, 379–469.

(3) *Ullmann's Encyclopedia of Industrial Chemistry*, ed. H. Knözinger and H. Kochloefl, Wiley-VCH Verlag GmbH & Co. KGaA, Weinheim, Germany, 2000.

(4) G. C. Bond, *Metal-Catalysed Reactions of Hydrocarbons*, Springer, New York, 2005.

(5) C. W. A. Chan, K. Y. Tam, J. Cookson, P. Bishop and S. C. Tsang, *Catalysis Science & Technology*, 2011, **1**, 1584–1592.

(6) D. Teschner, Z. Révay, J. Borsodi, M. Hävecker, A. Knop-Gericke, R. Schlögl, D. Milroy, S. D. Jackson, D. Torres and P. Sautet, *Angewandte Chemie - International Edition*, 2008, **47**, 9274–9278.

(7) L. C. Jones, Z. Buras and M. J. Gordon, *The Journal of Physical Chemistry C*, June 2012, **116**, 12982–12988.

(8) J. Stachurski, J. M. Thomas, J. Stachurski and J. M. T. Selective, 1988, **1**, 67–72.

(9) D. Teschner, J. Borsodi, Z. Kis, L. Szentmiklósi, Z. Révay, A. Knop-Gericke, R. Schlögl, D. Torres and P. Sautet, *The Journal of Physical Chemistry C*, 2010, **114**, 2293–2299.

(10) D. Teschner, J. Borsodi, A. Wootsch, Z. Révay, M. Hävecker, A. Knop-Gericke, S. D. Jackson and R. Schlögl, *Science*, May 2008, **320**, 86.

(11) M. Armbrüster, M. Behrens, F. Cinquini, K. Föttinger, Y. Grin, A. Haghofer, B. Klötzer, A. Knop-Gericke, H. Lorenz, A. Ota, S. Penner, J. Prinz, C. Rameshan, Z. Révay, D. Rosenthal, G. Rupprechter, P. Sautet, R. Schlögl, L. Shao, L. Szentmiklósi, D. Teschner, D. Torres, R. Wagner, R. Widmer and G. Wowsnick, *ChemCatChem*, Aug. 2012, **4**, 1048–1063.

(12) C. W. A. Chan, A. H. Mahadi, M. M.-J. Li, E. C. Corbos, C. Tang, G. Jones, W. C. H. Kuo, J. Cookson, C. M. Brown, P. T. Bishop and S. C. E. Tsang, *Nature Communications*, Jan. 2014, **5**, 5787.

(13) K. Tedsree, C. W. A. Chan, S. Jones, Q. Cuan, W.-K. Li, X.-Q. Gong and S. C. E. Tsang, *Science*, 2011, **332**, 224–228.

(14) C. W. A. Chan, Y. Xie, N. Cailuo, K. M. K. Yu, J. Cookson, P. Bishop and S. C. Tsang, *Chemical Communications*, July 2011, **47**, 7971–3.

(15) R. A. Rajadhyaksha and S. L. Karwa, *Chemical Engineering Science*, 1986, **41**, 1765.

(16) J. A. Bennett, R. P. Fishwick, R. Spence, J. Wood, J. M. Winterbottom, S. D. Jackson and E. H. Stitt, *Applied Catalysis A: General*, 2009, **364**, 57–64.

(17) U. K. Singh and M. A. Vannice, *Applied Catalysis A: General*, 2001, **213**, 1.

(18) A. Gamez, J. Köhler and J. Bradley, *Catalysis Letters*, 1998, **55**, 73.

(19) D. C. Wynne, M. M. Olmstead and P. G. Jessop, *Journal of the American Chemical Society*, 2000, **122**, 7638–7647.

(20) A. Baiker, *Chemical Reviews*, 1999, **99**, 453–473.

(21) C. Betti, J. Badano, C. Lederhos, M. Maccarrone, N. Carrara, F. Coloma-Pascual, M. Quiroga and C. Vera, *Reaction Kinetics, Mechanisms and Catalysis*, 2016, **117**, 283.

(22) B. S. Akpa, C. D'Agostino, L. F. Gladden, K. Hindle, H. Manyar, J. McGregor, R. Li, M. Neurock, N. Sinha, E. H. Stitt, D. Weber, J. A. Zeitler and D. W. Rooney, *Journal of Catalysis*, 2012, **289**, 30.

(23) S. Mukherjee and M. A. Vannice, *Journal of Catalysis*, 2006, **243**, 108.

(24) D. Deng, Y. Yang, Y. Ging, Y. Li, X. Xu and Y. Wang, *Green Chemistry*, 2013, **15**, 2525.

(25) N. O. Lemcoff, *Journal of Catalysis*, 1977, **46**, 1977.

(26) I. McManus, H. Daly, J. M. Thompson, E. Connor, C. Hardacre, S. K. Wilkinson, N. Sedaie Bonab, J. ten Dam, M. J. H. Simmons, E. H. Stitt, C. D'Agostino, J. McGregor, L. F. Gladden and D. J. J, *Journal of Catalysis*, 2015, **330**, 344–353.

(27) S. K. Wilkinson, I. McManus, H. Daly, J. M. Thompson, C. Hardacre, N. Sedaie Bonab, J. ten Dam, M. J. H. Simmons, C. D'Agostino, J. McGregor, L. F. Gladden and E. H. Stitt, *Journal of Catalysis*, 2015, **330**, 362–373.

(28) R. Sander, *Atmospheric Chemistry and Physics*, 2015, **15**, 4399–4981.

(29) L. L. Lopez, P. Bernatis, J. Birnbaum, R. C. Haltiwanger and M. R. DuBois, *Organometallics*, 1992, **11**, 2424–2435.

(30) P. Lühring and A. Schumpe, *Journal of Chemical and Engineering Data*, 1989, **34**, 250–252.

(31) M. Gurrath, T. Kuretzky, H. P. Boehm, L. B. Okhlopkova and A. S. Lisitsyn, *Carbon*, 2000, **38**, 1241–1255.

(32) A. Menzel, K. Swamy, R. Beer, P. Hanesch, E. Bertel and U. Birkenheuer, *Surface Science*, 2000, **454**, 88–93.

(33) Á. Mastalir, Z. Király, G. Szöllösi and M. Bartók, *Applied Catalysis A: General*, 2001, **213**, 133.

(34) D. J. Metz and A. Glines, *The Journal of Physical Chemistry*, 1967, **71**, 1158–1158.

(35) S. D. Jackson, C. A. Hamilton, G. J. Kelly and D. D. Bruin, *Reaction Kinetics and Catalysis Letters*, 2001, **73**, 77–82.

(36) A. L. Kolpin, D.Phil. Thesis, University of Oxford, 2014.

(37) J. C. A. A. Roelofs and P. H. Berben, *Chemical Communications*, 2004, **1**, 970–971.

(38) *Chemical Bonding at Surfaces and Interfaces*, ed. A. Nilsson, L. G. M. Pettersson and J. Nørskov, Elsevier, Amsterdam, 2008.

(39) K.-J. Hu, S. R. Plant, P. R. Ellis, C. M. Brown, P. T. Bishop and R. E. Palmer, *Phys. Chem. Chem. Phys.*, 2014, **16**, 26631–26637.

(40) R. D. O'Brien, *Fats and Oils: Formulating and Processing for Applications*, CRC Press, Boca Raton, Florida, 3rd, 2009.

(41) K. Iwasaki, K. K. Wan, A. Oppedisano, S. W. M. Crossley and R. A. Shenvi, *Journal of the American Chemical Society*, 2014, **136**, 1300–1303.

(42) A. J. McCue, C. J. McRitchie, A. M. Shepherd and J. A. Anderson, *Journal of Catalysis*, 2014, **319**, 127–135.

(43) D. W. Griffin, D. A. Mellichamp and M. F. Doherty, *AIChE Journal*, 2008, **54**, 2597.

(44) S. B. Ziemecki, G. A. Jones and D. G. Swartzfager, *Journal of Less-Common Metals*, 1987, **131**, 157–162.

(45) F. Studt, F. Abild-Pedersen, T. Bligaard, R. Z. Sørensen, C. H. Christensen and J. K. Nørskov, *Science*, June 2008, **320**, 1320.

(46) J. Osswald, K. Kovnir, M. Armbruster, R. Giedigkeit, R. Jentoft, U. Wild, Y. Grin and R. Schögl, *Journal of Catalysis*, Aug. 2008, **258**, 219–227.

(47) J. Osswald, R. Giedigkeit, R. Jentoft, M. Armbruster, F. Girgsdies, K. Kovnir, T. Ressler, Y. Grin and R. Schögl, *Journal of Catalysis*, Aug. 2008, **258**, 210–218.

(48) A. N. R. Bos and K. R. Westerterp, *Chemical Engineering and Processing*, 1993, **32**, 1–7.

(49) Y. Liu, Y. He, D. Zhou, J. Feng and D. Li, *Catal. Sci. Technol.*, 2016, **6**, 3027–3037.

(50) Y. A. Ryndin, M. V. Stenin, A. I. Boronin, V. I. Bukhtiyarov and V. I. Zaikovskii, *Applied Catalysis*, 1989, **54**, 277–288.

(51) J. T. Feng, X. Y. Ma, D. G. Evans and D. Q. Li, *Industrial and Engineering Chemistry Research*, 2011, **50**, 1947–1954.

7

Conclusions and Future Perspectives

Contents

7.1 Conclusions

Throughout this thesis, the primary objective has been to explore the interstitial modification of palladium for selective partial hydrogenation catalysts. To this end, new green synthetic routes to the known Pd-$^{\text{interstitial}}$B/C catalyst were developed and screened. In addition, the novel Pd-$^{\text{interstitial}}$Li/C system was developed for the first time and was initially catalytically tested and characterised.

These two interstitial systems underwent further detailed characterisations to broaden the understanding of the Pd-$^{\text{interstitial}}$B/C system through refining prior investigations into its nature, and thoroughly characterising Pd-$^{\text{interstitial}}$Li/C. This work provides near-conclusive proof of the interstitial location of lithium short of directly imaging it within the palladium lattice. A figure of 13.7 % of the octahedral sites are believed to be occupied by lithium, comparable to the Pd-$^{\text{interstitial}}$B/C (20 % occupied) and Pd-$^{\text{interstitial}}$C/C (15 % occupied) systems.

The interstitial dopant within these materials alters the surface electronics of the system and hence the reactivity of the catalyst can be tuned. DFT work highlighted the differing effects boron and lithium have on the metal, with boron lowering electron density at the Fermi level and lithium raising it. This changes the binding strength of reactive molecules to the catalyst surface which impacts catalytic performance.

A range of different substrates were hydrogenated in different solvent and phase

regimes where the differences in reactivity and selectivity due to the catalyst modification became apparent. The change in electron density at the Fermi level of the interstitially modified Pd/C catalysts led to altered residence times for the reactive molecules on the catalyst surface. This gave rise to changes in the relative rate of hydrogenation or isomerisation between the systems. Interstitial modification allows tuning of the catalysts for any hydrogenation reaction. Broadly speaking, the optimal catalyst to use depends on the conditions being investigated and interstitial modification provides a simple way to change reaction outputs.

7.2 Future Perspectives

The research presented in this thesis provides an understanding of how a catalyst can be modified interstitially to subtly alter its catalytic behaviour. In future work other metal systems like ruthenium could be investigated for interstitial doping, or expanding the range of known palladium interstitial dopants could be explored.

For a more industrially relevant catalyst, reducing the palladium loading from 5 % whilst maintaining the interstitial modification is desirable, as well as expanding the range of reactions these catalysts can be used for. Indeed, optimising the grinding approaches will provide an excellent solvent-free approach to these interstitial catalysts. Similarly, a number of different experiments could be conducted to build upon this work. Firstly, EXAFS could be used as a complimentary technique to the PDF studies of the on Pd-$^{\text{interstitial}}$Li material. Indeed, PDF on Pd-$^{\text{interstitial}}$B may be able to provide complimentary information on the observed fcc to hcp transition seen in STEM.

Computationally, expanding the DFT study to include calculating changes in substrate binding energy for the tested reagents to see if that correlates with the observed experimental results. There is also merit in studying further hydrogenation reactions, as well as expanding the catalytic behaviour of these materials in more

solvent free systems.

In a broader sense, nanotechnology is a growth area necessary to develop catalysts for new processes, or improve older processes to reduce waste and cost. This is a requirement to meet the social, economic and environmental challenges of the future.